Theoretical Study of the Effect of Counteranions on Olefin Polymerization Reaction by (Pyridylamido)Hf Catalyst

Nana Misawa

Contents

Chapter 1
General Introduction

1.1. Introduction

Polyolefins, which are synthesized through polymerization of alkene monomers, play essential roles in our daily lives. A wide variety of polyolefins have been synthesized over 200 million metric tons every year and commercially utilized in a wide range of plastic products like pipes, packaging films, household bottles, automobile parts, disposable diapers, food containers, etc. [1–5]. These days, demands of polyolefin keep its growth by about 5% every year, as the global population grows [5]. Therefore, improvement of production efficiencies and material properties are strongly desired.

For efficient production of polyolefins, catalysts are typically used to reduce the activation energy for the polymerization process, thereby speeding up the reaction and allowing it to proceed even under mild conditions. Since the great invention of Ziegler–Natta catalyst for ethylene polymerization in the 1950s [6–8], olefin polymerization catalyst has developed remarkably to meet the demand for versatile and cost-efficient plastics [9,10]. Although Ziegler-Natta catalysts are still used to produce large volumes of polyethylene and polypropylene, broad molecular weight distributions (MWDs) of the produced polymer materials indicate that the catalysts have a several types of catalytic active sites.

In the late 20th century, the major focus in polymer chemistry was placed on producing materials with controlled molecular architectures and polymer morphology [11–13]. In this aspect, the discovery of the metallocene catalysts in the late 1970s, which have only one kind of active metal center [14–20], opened the possibility to synthesize polymers with a narrow MWD, highly defined microstructure, controlled tacticity, and stereoregularity. Besides, copolymerization of ethylene with propylene or higher α-olefins by metallocene catalysts enabled the commercial production of polyolefin elastomers with a wide range of properties through changing the type and ratio of the α-olefin comonomers [21–27].

In more recent years, a wide variety of "post-metallocene" catalysts with non-cyclopentadienyl ligands have been developed, which offer rich and unique mechanistic features and novel polymer microstructures [28–30]. Among them, (pyridylamido)Hf(IV) catalyst [31–34] is attracting attention for its strong ability to incorporate α-olefin comonomers and thus utilized for industrial-scale production of various polyolefins. Notably, this catalyst is applied in the chain shuttling polymerization (CSP) technology [34–36], where multiblock copolymers with highly crystalline polyethylene and amorphous poly(ethylene-co-α-olefin) blocks can be obtained by introducing a chain transfer agent (CSA) such as $ZnEt_2$ into a solution mixture of two catalyst species with different 1-octene incorporation abilities.

It should be noted here that the group 4 metal catalysts, which have been developed as the main group of polymerization catalysts, cannot work alone: they must be activated by cocatalysts before starting the polymerization reaction to become their cationic active form. Two types of activating cocatalyst have been commonly used to activate group 4

metal complexes; methyl aluminoxane (MAO) and boron-based cocatalysts [37], which become counteranions (CAs) after the catalyst activation and work with the cationic active catalyst, forming ion pairs (IPs). It is well known that CAs derived from the cocatalysts have significant effects on the yield or physical properties of the polymers produced by the metallocene catalysts [14–20] and post-metallocene catalysts [38–43]. Thus, the mechanism of catalytic polymerization (CP) reactions in the presence of CA should be elucidated in order to determine how CAs affect the properties of polymers.

To systematically understand the CP reaction mechanisms in the presence of CAs, the fundamental reaction, monomer insertion reaction, would be essentially regarded as a bimolecular reaction between a catalyst and a monomer, with a CA coexisting near the catalyst. Then, the insertion reaction can be divided into the two characteristic processes; a diffusion process, where the catalyst and monomer diffuse in solution to encounter each other, and an activation process, where the insertion reaction takes place between the encountered catalyst and monomer [44]. Under this assumption, in the diffusion process, CAs are expected to affect the encounter rate between the catalyst and monomer by moving around the active site to allow or block the monomer coordination to the catalyst [45,46]. On the other hand, in the activation process, CAs should affect the thermodynamic properties of the reaction, i.e., the probability of the actual reaction taking place between the encountered catalyst and monomer, through the electrostatic interaction with the cationic catalyst [47]. For the sake of simplicity, in this thesis, the above effects in the diffusion and activation processes would be hereafter called “dynamic” and “electronic” effects, respectively.

It is difficult to experimentally investigate the “dynamic” and “electronic” effects in the instantaneous phenomena of the CP reaction. For this reason, computational chemistry methodologies have been utilized as alternatives providing complementary information to the experimental ones, which enables a better understanding of the effect of CAs. For example, a lot of theoretical studies have been conducted on the activation process of the monomer insertion reaction using the quantum mechanics (QM) method [48] to reveal the “electronic” effect of CAs, especially in the metallocene-based CP systems [45–47,49–61]. On the other hand, only a limited number of studies have investigated in the diffusion process by employing the molecular dynamics (MD) method [62] to analyze the “dynamic” effect of CAs through simulating the atomistic motions of catalysts and CAs [63–66]. However, to make a computational study comparable to the experimental one, both diffusion and activation processes should be dealt with, which eventually leads to a better understanding of the electronic and dynamic effects of CAs in the overall CP reaction.

For this purpose, Red Moon (RM) method [67,68] should be effectively employed, which enables a full-atomistic molecular simulation of so-called “complex chemical reaction”, i.e., the whole CP reaction, as a succession of elementary reaction processes, i.e., the monomer insertion reaction. In this method, diffusion and activation processes could be reasonably described by using MD and Monte Carlo (MC) methods, respectively. Hence, RM method has great potential to provide deeper insights into the overall CP reaction mechanisms with CAs, which cannot be simulated using conventional QM and MD methods.

In this thesis, therefore, using these computational methods, I conduct a comprehensive study of the dynamic and electronic effects of CAs on monomer insertion reaction and the overall CP reaction in order to obtain some new insights into the role of CAs. In particular, I focus on the catalytic activities of (pyridylamido)Hf(IV) catalyst [38–40] and on the MWD of its produced polymers [39], which has been experimentally reported to be affected by the boron-based CAs, $MeB(C_6F_5)_3^-$ and $B(C_6F_5)_4^-$. Therefore, I investigate the mechanism of olefin monomer insertion reaction into the Hf–alkyl bond of (pyridylamido)Hf(IV) catalyst by taking advantage of QM and MD methods in combination to reveal the dynamic and electronic effects of CAs on the catalytic activity. On the basis of the mechanistic insight, I also perform full-atomistic simulations based on RM method, which can deal with the whole CP reaction process and thus enables the virtual production of a growing polymer chain on the catalyst, to investigate the effect of the CAs on the MWDs of the produced polymers.

To save space and make the discussion easier to understand, abbreviations have been introduced throughout this thesis, as shown in **Table of Abbreviations**.

Table of Abbreviations

Abbreviation	Full name or description
$HfCat^+$	The initial cationic active species of (pyridylamido)Hf(IV) catalyst
CP	Catalytic polymerization
CA	Counteranion
3PFB	$MeB(C_6F_5)_3^-$ (methyltris(perfluorophenyl)borate)
4PFB	$B(C_6F_5)_4^-$ (tetrakis(perfluorophenyl)borate)

QM	Quantum mechanics
MD	Molecular dynamics
REMD	Replica-exchange molecular dynamics
IP	Ion pair
ISIP	Inner-sphere ion pair
OSIP	Outer-sphere ion pair
AASO	Associative active site opening
MS	Minimum-energy state
RS	Reactant state
TS	Transition state
PS	Product state
CK	Chemical kinetics
IDE	Ion pair dissociation energy
CTE	Conformational transition energy
FE	Free energy
FES	Free energy surface
$HfCat^{Pn+}$	The cationic active species of (pyridylamido)Hf(IV) catalyst with 1-octene *n*-mer chain
MWD	Molecular weight distribution
PDI	Polydispersity index

1.2. Chemical Kinetics of Second-Order Reaction

In the CP reactions, the principal reaction is essentially considered a bimolecular second-order reaction between an olefin monomer and a polymerization catalyst, and is in general described by the following typical second-order reaction scheme [44],

$$\mathrm{A} + \mathrm{B} \xrightarrow{k_2} \mathrm{C}, \tag{1.1}$$

where A and B correspond to the catalyst and olefin monomer, and C does to the catalyst with ‘one monomer’-longer growing chain, and k_2 is the reaction rate constant for the CP reaction.

1.2.1. Diffusion and Activation Processes

In the chemical kinetics (CK) treatment, it is common that the second-order reaction in solution can be modeled as a combination of two successive processes, i.e., a diffusion process and an activation process [44]. The former is a process in which the reactants A and B diffuse in solution and then encounter each other to form an association complex $\mathrm{A}\cdots\mathrm{B}$, while the latter is a process in which $\mathrm{A}\cdots\mathrm{B}$ turns to the product C. Considering these two processes, the scheme (1.1) can be expressed more precisely as [44],

$$\mathrm{A} + \mathrm{B} \underset{k_{\mathrm{d}}'}{\overset{k_{\mathrm{d}}}{\rightleftarrows}} \mathrm{A}\cdots\mathrm{B} \xrightarrow{k_{\mathrm{a}}} \mathrm{C}, \tag{1.2}$$

where k_{d} is the rate constant of association of A and B, and k_{d}' is that of dissociation of $\mathrm{A}\cdots\mathrm{B}$ through the diffusion process, while k_{a} is the rate constant of the activation process to form the product C. The reverse reaction in the activation process is not considered for simplicity.

1.2.2. Steady-State Approximation and Two-Limiting Schemes

a. Activation-Controlled Scheme

If the steady-state approximation is to be applied to the concentration [A···B], k_2 is obtained as,

$$k_2 = \frac{k_a \cdot k_d}{k_a + k_d'}. \tag{1.3}$$

Further, if the second-order reaction is activation-controlled, i.e., $k_a << k_d'$ is satisfied, k_2 is approximately estimated as,

$$k_2 = \frac{k_a \cdot k_d}{k_a + k_d'} \approx k_a \frac{k_d}{k_d'} = k_a \cdot K_d, \tag{1.4}$$

where K_d is the equilibrium constant, defined as k_d/k_d'. This means that the kinetic constant k_a and equilibrium constant K_d essentially determine k_2 in the activation-controlled scheme.

Then, k_a can be obtained by the transition state theory as,

$$k_a = \kappa \frac{k_B T}{h} \exp\left(-\frac{G_{TS}}{RT}\right), \tag{1.5}$$

where κ and T are the transmission coefficient and the temperature, respectively, and G_{TS} is the activation energy, assuming that the transition state (TS) $(A\cdots B)^{\ddagger}$ exists between A···B and C.

On the other hand, K_d can be obtained as,

$$K_{\mathrm{d}} = \frac{[\mathrm{A}\cdots\mathrm{B}]}{[\mathrm{A}][\mathrm{B}]}, \tag{1.6}$$

because the relation

$$\frac{[\mathrm{A}\cdots\mathrm{B}]}{[\mathrm{A}][\mathrm{B}]} = \frac{k_{\mathrm{d}}}{k_{\mathrm{a}} + k_{\mathrm{d}}'} \approx \frac{k_{\mathrm{d}}}{k_{\mathrm{d}}'}, \tag{1.7}$$

can be obtained from the inequality $k_{\mathrm{a}} << k_{\mathrm{d}}'$ in the activation-controlled scheme.

In this scheme, therefore, both G_{TS} and the concentrations [A], [B], and $[\mathrm{A}\cdots\mathrm{B}]$ in equilibrium are necessary parameters.

b. Diffusion-Controlled Scheme

On the other hand, if the second-order reaction is diffusion-controlled, i.e., $k_{\mathrm{a}} >> k_{\mathrm{d}}'$ is satisfied, k_2 can be approximately estimated as

$$k_2 = \frac{k_{\mathrm{a}} \cdot k_{\mathrm{d}}}{k_{\mathrm{a}} + k_{\mathrm{d}}'} \approx k_{\mathrm{d}}. \tag{1.8}$$

This means that only k_{d} determines k_2. Thus, the precise scheme (1.2) can simply become:

$$\mathrm{A} + \mathrm{B} \xrightarrow{k_{\mathrm{d}}} \mathrm{C}. \tag{1.9}$$

Then, the rate equation in terms of the concentration of B at a certain time t $[\mathrm{B}]_t$ is expressed using k_{d} and the concentration of A at a certain time t $[\mathrm{A}]_t$ as,

$$-\frac{d[\mathrm{B}]_t}{dt} = k_{\mathrm{d}}[\mathrm{A}]_t[\mathrm{B}]_t. \tag{1.10}$$

When both sides are integrated with respect to t in the time interval [0, t], k_{d} is derived as,

$$k_{\mathrm{d}} = \frac{\ln[\mathrm{B}]_0 - \ln[\mathrm{B}]_t}{\int_0^t [\mathrm{A}]_t \, dt}. \tag{1.11}$$

In this scheme, therefore, the time-dependent concentrations $[A]_t$ and $[B]_t$ are necessary.

1.3. Thesis Outline

In the present thesis, to discuss systematically the effects of CAs in olefin polymerization reaction catalyzed by (pyridylamido)Hf catalyst, I divide this thesis into four chapters.

In Chapter 2, I investigate the 1-octene insertion reaction into the Hf–Me bond in the initial structure of the cationic active species of (pyridylamido)Hf(IV) catalyst ($HfCat^+$), focusing on the effect of the boron-based CAs, $MeB(C_6F_5)_3^-$ and $B(C_6F_5)_4^-$ on the catalytic activity. It is experimentally reported that the 1-octene polymerization reaction proceeds about twice faster with $B(C_6F_5)_4^-$ than with $MeB(C_6F_5)_3^-$. Therefore, to reveal the origin of this phenomenon, I analyze the activation and diffusion processes of 1-octene polymerization reaction catalyzed by $HfCat^+$ with these CAs using QM and replica exchange molecular dynamics (REMD) calculation, respectively. Then, I investigate the difference in the IP structures between $HfCat^+$–$MeB(C_6F_5)_3^-$ and $HfCat^+$–$B(C_6F_5)_4^-$ IP complexes, which are expected to significantly influence the CP reaction rates. Using the data obtained from the QM and REMD studies, I numerically evaluate the rate constants of 1-octene polymerization reaction catalyzed by the two IP complexes and compare them with the experimental ones. Finally, I discuss the crucial factor that determines the difference in the catalytic activities between $HfCat^+$–$MeB(C_6F_5)_3^-$ and $HfCat^+$–$B(C_6F_5)_4^-$ IP complexes.

In Chapter3, on the basis of the findings in Chapter 2, I conduct atomistic simulations of 1-octene polymerization reaction by (pyridylamido)Hf(IV) catalyst based on RM methodology. Through the RM simulations, I investigate the effect of the CAs, $MeB(C_6F_5)_3^-$ and $B(C_6F_5)_4^-$ on the activity and living character of 1-octene polymerization reaction by (pyridylamido)Hf(IV) catalyst with growing polymer chain ($HfCat^{Pn+}$) during the polymerization reaction. I demonstrate that RM simulation reproduces the faster reaction rate with $B(C_6F_5)_4^-$ than with $MeB(C_6F_5)_3^-$. Notably, I reveal the origin of a comparably slow initiation of polymerization reaction experimentally observed with $MeB(C_6F_5)_3^-$. Then I discuss the IP structures of $HfCat^{Pn+}$–$MeB(C_6F_5)_3^-$ and $HfCat^{Pn+}$–$B(C_6F_5)_4^-$ during the polymerization reaction, which is supposed to determine the polymerization reaction rates. Finally, I try to elucidate the origin of the experimentally reported MWD value of the polymer being broader with $B(C_6F_5)_4^-$ than with $MeB(C_6F_5)_3^-$, which means that the former CP reaction system has a less living character in its polymerization reaction than the latter one. Through the trajectory analyses of the RM simulations, I discuss the relative probability of the termination reaction to the 1-octene insertion reaction being influenced by the IP structures, which determines the living character of the CP reaction system.

In Chapter 4, the general conclusion of this thesis is provided, including future perspectives.

References

[1] Craver, C.; Carraher, C. *Applied Polymer Science: 21st Century*; Elsevier Science, 2000.

[2] Peacock, A. J. *Polymer chemistry : properties and applications*; Hanser Gardner Publications: Munich, 2006.

[3] Carraher, C.; Seymour, R. *Seymour/Carraher's Polymer Chemistry, Seventh Edition*; Undergraduate chemistry; Taylor & Francis, 2008.

[4] Chanda, M. *Introduction to Polymer Science and Chemistry: A Problem-Solving Approach*; CRC Press, 2006.

[5] Jubinville, D.; Esmizadeh, E.; Saikrishnan, S.; Tzoganakis, C.; Mekonnen, T. *Sustainable Materials and Technologies* **2020**, *25*, e00188.

[6] Ziegler, K.; Gellert, H.; Zosel, K.; Lehmkuhl, W.; Pfohl, W. *Angew. Chem.* **1955**, *67*, 424.

[7] Natta, G. *Angew. Chem.* **1956**, *68*, 393.

[8] Wilke, G. *Angew. Chem. Int. Ed.* **2003**, *42*, 5000.

[9] Soga, K.; Shiono, T. *Prog. Polym. Sci.* **1997**, *22*, 1503.

[10] Collins, R. A.; Russell, A. F.; Mountford, P. *Appl. Petrochem. Res.* **2015**, *5*, 153.

[11] Schrder, K.; Matyjaszewski, K.; Noonan, K. J. T.; Mathers, R. T. *Green Chem.* **2014**, *16*, 1673.

[12] Stürzel, M.; Mihan, S.; Mülhaupt, R. *Chem. Rev.* **2016**, *116*, 1398.

[13] Hong, M.; Chen, E. Y.-X. *Trends Chem.* **2019**, *1*, 148.

[14] Sinn, H.; Kaminsky, W. *Adv. Organomet. Chem.* **1980**, *18*, 99.

[15] Sinn, H.; Kaminsky, W.; Vollmer, H. J.; Woldt, R. *Angew. Chem., Int. Ed. Engl.* **1980**, *19*, 390.

[16] Brintzinger, H. H.; Fischer, D.; Mülhaupt, R.; Rieger, B.; Waymouth, R. M. *Angew. Chem., Int. Ed. Engl.* **1995**, *34*, 1143.

[17] Alt, H. G.; Koppl, A. *Chem. Rev.* **2000**, *100*, 1205.

[18] Resconi, L.; Cavallo, L.; Fait, A.; Piemontesi, F. *Chem. Rev.* **2000**, *100*, 1253.

[19] Osakada, K.; Carpenter, B.; Ceroni, P.; Kirchner, B.; Landfester, K.; Leszczynski, J.; Luh, T. Y.; Perlt, E.; Polfer, N. C.; Salzer, R. *Organometallic Reactions and Polymerization*; 2014; Vol. 85.

[20] Bochmann, M. *J. Organomet. Chem.* **2004**, *689*, 3982.

[21] Johnson, L. K.; Killian, C. M.; Brookhart, M. *J. Am. Chem. Soc.* **1995**, *117*, 6414.

[22] Guo, L.; Liu, W.; Chen, C. *Mater. Chem. Front.* **2017**, *1*, 2487.

[23] Furuyama, R.; Mitani, M.; Mohri, J.-i.; Mori, R.; Tanaka, H.; Fujita, T. *Macromolecules* **2005**, *38*, 1546.

[24] Klosin, J.; Fontaine, P. P.; Figueroa, R. *Acc. Chem. Res.* **2015**, *48*, 2004.

[25] Wang, W.-J.; Kolodka, E.; Zhu, S.; Hamielec, A. E. *J. Polym. Sci., Part A: Polym. Chem.* **1999**, *37*, 2949.

[26] Gibson, V. C.; Spitzmesser, S. K. *Chem. Rev.* **2003**, *103*, 283.

[27] Ittel, S. D.; Johnson, L. K.; Brookhart, M. *Chem. Rev.* **2000**, *100*, 1169.

[28] Britovsek, G. J. P.; Gibson, V. C.; Wass, D. F. *Angew. Chem. Int. Ed.* **1999**, *38*, 428.

[29] Gibson, V. C.; Spitzmesser, S. K. *Chem. Rev.* **2003**, *103*, 283–316, PMID: 12517186.

[30] Baier, M. C.; Zuideveld, M. A.; Mecking, S. *Angew. Chem. Int. Ed.* **2014**, *53*, 9722.

[31] Boussie, T. R.; Diamond, G. M.; Goh, C.; Hall, K. A.; LaPointe, A. M.; Leclerc, M.; Lund, C.; Murphy, V.; Shoemaker, J. A. W.; Tracht, U.; Turner, H.; Zhang, J.; Uno, T.; Rosen, R. K.; Stevens, J. C. *J. Am. Chem. Soc.* **2003**, *125*, 4306.

[32] Boussie, T. R.; Diamond, G. M.; Goh, C.; Hall, K. A.; LaPointe, A. M.; Leclerc, M. K.; Murphy, V.; Shoemaker, J. A. W.; Turner, H.; Rosen, R. K.; Stevens, J. C.; Alfano, F.; Busico, V.; Cipullo, R.; Talarico, G. *Angew. Chem., Int. Ed.* **2006**, *45*, 3278.

[33] Frazier, K. A.; Froese, R. D.; He, Y.; Klosin, J.; Theriault, C. N.; Vosejpka, P. C.; Zhou, Z.; Abboud, K. A. *Organometallics* **2011**, *30*, 3318.

[34] Chum, P. S.; Swogger, K. W. *Prog. Polym. Sci.* **2008**, *33*, 797.

[35] Arriola, D. J.; Carnahan, E. M.; Hustad, P. D.; Kuhlman, R. L.; Wenzel, T. T. *Science* **2006**, *312*, 714.

[36] Wenzel, T. T.; Arriola, D. J.; Carnahan, E. M.; Hustad, P. D.; Kuhlman, R. L. *Top. Organomet. Chem.* **2009**, *26*, 65.

[37] Chen, E. Y.-X.; Marks, T. J. *Chem. Rev.* **2000**, *100*, 1391.

[38] Busico, V.; Cipullo, R.; Pellecchia, R.; Rongo, L.; Talarico, G.; Macchioni, A.; Zuccaccia, C.; Froese, R. D. J.; Hustad, P. D. *Macromolecules* **2009**, *42*, 4369.

[39] Domski, G. J.; Lobkovsky, E. B.; Coates, G. W. *Macromolecules* **2007**, *40*, 3510.

[40] Cueny, E. S.; Johnson, H. C.; Anding, B. J.; Landis, C. R. *J. Am. Chem. Soc.* **2017**, *139*, 11903.

[41] Matsui, S.; Fujita, T. *Catal. Today* **2001**, *66*, 63 – 73, Nano-structured Materials and their Catalytic Functions.

[42] Makio, H.; Terao, H.; Iwashita, A.; Fujita, T. *Chem. Rev.* **2011**, *111*, 2363, PMID: 21250670.

[43] Romano, D.; Andablo-Reyes, E.; Ronca, S.; Rastogi, S. *Polymer* **2015**, *74*, 76 – 85.

[44] Atkins, P.; De Paula, J.; Keeler, J. *Atkins' Physical Chemistry*; Oxford University Press, 2018.

[45] Flisak, Z.; Ziegler, T. *Proc. Natl. Acad. Sci.* **2006**, *103*, 15338.

[46] Rappé, A. K.; Skiff, W. M.; Casewit, C. J. *Chem. Rev.* **2000**, *100*, 1435.

[47] Parveen, R.; Cundari, T. R.; Younker, J. M.; Rodriguez, G. *Organometallics* **2020**, *39*, 2068.

[48] Jensen, F. *Introduction to computational chemistry*; John Wiley & Sons, 2017.

[49] Sandhya, K. S.; Koga, N.; Nagaoka, M. *Bull. Chem. Soc. Jpn.* **2016**, *89*, 1093.

[50] Angermund, K.; Fink, G.; Jensen, V. R.; Kleinschmidt, R. *Chem. Rev.* **2000**, *100*, 1457.

[51] Zurek, E.; Ziegler, T. *Faraday Discuss.* **2003**, *124*, 93.

[52] Xu, Z.; Vanka, K.; Ziegler, T. *Organometallics* **2004**, *23*, 104.

[53] Ziegler, T.; Vanka, K.; Xu, Z. *C. R. Chim.* **2005**, *8*, 1552.

[54] Tomasi, S.; Razavi, A.; Ziegler, T. *Organometallics* **2007**, *26*, 2024.

[55] Lanza, G.; Fragalà, I. L.; Marks, T. J. *J. Am. Chem. Soc.* **2000**, *122*, 12764.

[56] Lanza, G.; Fragalà, I. L.; Marks, T. J. *Organometallics* **2002**, *21*, 5594.

[57] Motta, A.; Fragalà, I. L.; Marks, T. J. *J. Am. Chem. Soc.* **2007**, *129*, 7327.

[58] Motta, A.; Fragalà, I. L.; Marks, T. J. *J. Am. Chem. Soc.* **2008**, *130*, 16533.

[59] Sian, L.; Macchioni, A.; Zuccaccia, C. *ACS Catal.* **2020**, *10*, 1591.

[60] Laine, A.; Coussens, B. B.; Hirvi, J. T.; Berthoud, A.; Friederichs, N.; Severn, J. R.; Linnolahti, M. *Organometallics* **2015**, *34*, 2415.

[61] Kumawat, J.; Gupta, V. K. *ACS Catal.* **2020**, *10*, 1704.

[62] Frenkel, D.; Smit, B. *Understanding molecular simulation: from algorithms to applications*; Elsevier, 2001; Vol. 1.

[63] Correa, A.; Cavallo, L. *J. Am. Chem. Soc.* **2006**, *128*, 10952.

[64] Yang, S.; Ziegler, T. *Organometallics* **2006**, *25*, 887.

[65] Rowley, C. N.; Woo, T. K. *Organometallics* **2011**, *30*, 2071.

[66] Matsumoto, K.; Sandhya, K. S.; Takayanagi, M.; Koga, N.; Nagaoka, M. *Organometallics* **2016**, *35*, 4099.

[67] Nagaoka, M.; Suzuki, Y.; Okamoto, T.; Takenaka, N. *Chem. Phys. Lett.* **2013**, *583*, 80.

[68] Suzuki, Y.; Nagaoka, M. *J. Chem. Phys.* **2017**, *146*, 204102.

Chapter 2

Theoretical Elucidation of the Effect of Counteranions on the Olefin Polymerization Activity of (Pyridylamido)Hf(IV) Catalyst by QM and REMD Studies: $MeB(C_6F_5)_3^-$ versus $B(C_6F_5)_4^-$

2.1. Introduction

(Pyridylamido)Hf(IV) catalyst [1–4] is attracting attention as an ethylene/α-olefin copolymerization catalyst, which can be utilized in the chain-shuttling polymerization (CSP) technique for the production of ethylene/1-octene multi-block copolymers [4–6]. Hence, a lot of mechanistic studies [7–22] and ligand modifications [23–26] of this catalyst have been conducted so far.

The (pyridylamido)Hf(IV) catalyst needs to be activated by a cocatalyst to initiate a polymerization reaction (**Figure 1**). The activation process consists of the following steps: First, the Me group in precatalyst 1 is abstracted by the cocatalyst to yield cationic catalyst 2^+, which works with a counteranion (CA) generated from the cocatalyst, forming an ion pair (IP) [27]. Next, a monomer is inserted to the Hf–naphthyl bond to form the catalytically active species, called “monomer-inserted” active species 3^+ [8,9].

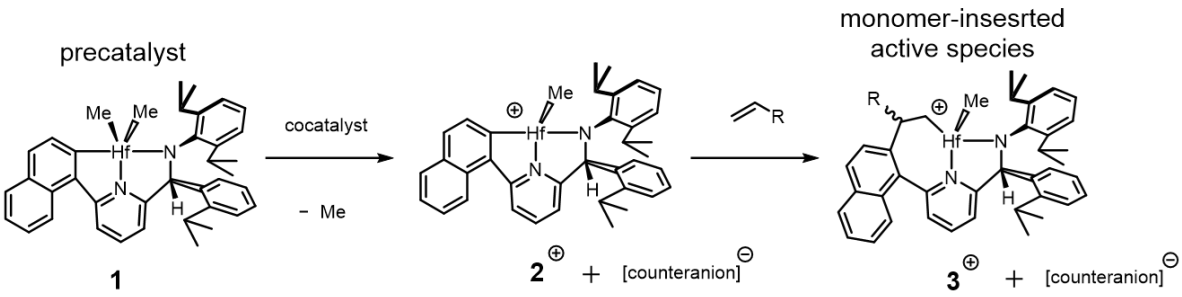

Figure 1. Schematic representations of activation process of (pyridylamido)Hf(IV) complex by a cocatalyst and the following monomer insertion process.

There are two types of activating cocatalyst commonly used for group 4 metal complexes: methyl aluminoxane (MAO) and boron-based cocatalysts [28]. The former does not have a defined chemical structure, and the required MAO/catalyst ratio ranges from 500:1 to 10000:1 in metallocene catalysts to achieve high activities [29,30]. In contrast, the latter has a structure that can be easily identified, and only about a 1:1 ratio of cocatalyst/catalyst is required. Therefore, in recent years, boron-based cocatalysts have been widely used in homogeneous olefin polymerization reactions.

Among the boron-based cocatalysts, perfluorophenyl borane $B(C_6F_5)_3$ and trityl borate salt $[C(C_6H_5)_3][B(C_6F_5)_4]$ are the most widely used [31]. The catalyst activation processes with these boron-based cocatalysts proceed, as shown in **Figure 2.** The methide abstraction of precatalyst 1 by $B(C_6F_5)_3$ yields cationic catalyst 2^+, and $MeB(C_6F_5)_3^-$. On the other hand, the methide abstraction of precatalyst 1 by $[C(C_6H_5)_3][B(C_6F_5)_4]$ yields cationic catalyst 2^+, the neutral byproduct $MeC(C_6H_5)_3$, and $B(C_6F_5)_4^-$. Although the structural difference between $MeB(C_6F_5)_3^-$ and $B(C_6F_5)_4^-$ is slight (only one substituent on B atom), it is experimentally reported that olefin

polymerization reaction by (pyridylamido)Hf(IV) catalyst with $B(C_6F_5)_4^-$ tends to proceed faster than with $MeB(C_6F_5)_3^-$ [11,14,16].

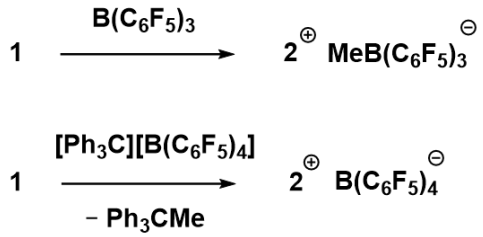

Figure 2. Schematic representations of activation process of (pyridylamido)Hf(IV) complex by $B(C_6F_5)_3$ and $[Ph_3C][B(C_6F_5)_4]$ cocatalysts. $B(C_6F_5)_3$ yields $MeB(C_6F_5)_3^-$ and $[Ph_3C][B(C_6F_5)_4]$ yields $B(C_6F_5)_4^-$ as CAs after activation.

Such a fact has been observed not only in the (pyridylamido)Hf(IV) catalyst but also in other group 4 metal complexes such as Kaminsky catalysts [32–38]. Hence, the mechanisms of the polymerization reactions of Kaminsky catalysts with these CAs have been intensively studied so far by experimental [39–41] and theoretical methods [42–60]. It is a well-established fact that weakly coordinating CAs can facilitate monomer coordination, leading to higher catalytic activity [27,28,39,56–62]. It was also suggested that the monomer capture process plays an important role in determining the polymerization reaction rate [63], and CAs are likely to be relevant in this process [58]. However, among the previous computational studies, only a few theoretical studies have focused on the dynamic aspect of the effect of CAs [53–55]. Therefore, it would be valuable to conduct a comprehensive study on the polymerization reaction mechanism by using both quantum mechanics (QM) and molecular dynamics (MD) methods to reveal the microscopic origin of the different reaction rates depending on the CAs.

In our group, the theoretical studies on the polymerization mechanism with the cationic (pyridylamido)Hf(IV) catalyst and the $MeB(C_6F_5)_3^-$ anion have been conducted using computational chemistry methods at the atomic level. In particular, we have determined the associative active site opening (AASO) mechanism in the activation step of ethylene insertion reaction using MD method [64]. In addition, we have elucidated the important role of $MeB(C_6F_5)_3^-$ in the stereoregularity of propylene insertion reaction using QM method [65]. On the basis of these findings, in this study, I attempt to elucidate the microscopic effect of each $MeB(C_6F_5)_3^-$ and $B(C_6F_5)_4^-$ on the 1-octene polymerization process with the (pyridylamido)Hf(IV) catalyst from both electronic and dynamic aspects using QM and MD method in combination and theoretically elucidate the crucial factors affecting the polymerization rates.

Therefore, first, I analyze the electronic and dynamic effects of the CA on 1-octene insertion reaction by using QM and replica exchange molecular dynamics (REMD) calculations, respectively. Then, from the obtained calculation results, I theoretically estimate the reaction rate constants based on the chemical kinetic formulation and compare them with the experimentally reported reaction rates. Throughout the chapter, I try to theoretically understand the microscopic origin of the 1-octene polymerization reaction rate being larger with $B(C_6F_5)_4^-$ than with $MeB(C_6F_5)_3^-$ theoretically [14]. This chapter is organized as follows: Section 2.2 describes the model systems, QM and REMD calculation methods, and the treatment of chemical kinetics. In Section 2.3, results and discussion are provided. Finally, in the last section, the findings of this study are summarized.

2.2. Models and Computational Methods

2.2.1. Model Schemes of 1-Octene Insertion Reaction by (Pyridylamido)Hf(IV) Complex

In this study, I adopt the “ethylene”-inserted active species ($HfCat^{+}$ in **Figure 3**) as a monomer-inserted active species 3^{+} (**Figure 1**), for the sake of simplicity. Thus, the polymerization proceeds with the successive monomer insertion to the Hf–alkyl bond of $HfCat^{+}$ to form $HfCat^{Pn+}$, where n is the number of inserted monomer units ($n \geq 0$), assuming hereafter $HfCat^{P0+}$ denotes $HfCat^{+}$ itself (**Figure 3**). This chapter will treat the first insertion process of 1-octene monomer to $HfCat^{P0+}$ giving $HfCat^{P1+}$, as an essential reaction process for the targeting polymerization reaction.

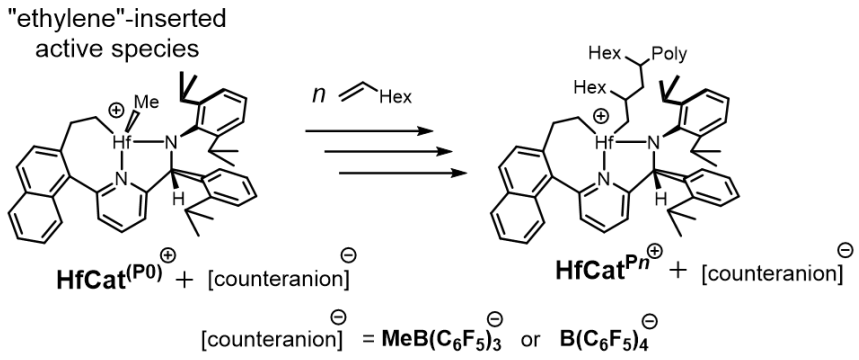

Figure 3. Schematic representation of 1-octene polymerization reaction by the “ethylene”-inserted active species ($HfCat^{+}$) adopted as a model of the active catalyst structure, which gives $HfCat^{Pn+}$ with n-meric 1-octene polymer chain. “Poly” represents a polymer chain. Only the first insertion is considered in this study.

According to the previous study [13,65], two types of coordination sites can be assumed in $HfCat^+$, which are defined as *trans* and *cis* to distinguish them relative to the pyridine nitrogen atom of $HfCat^+$ (**Figure 4(a)**). In addition to the coordination sites, it is necessary to consider the orientation of 1-octene coordination, i.e., 1,2-insertion and 2,1-insertion (**Figure 4(b)**), which is expected to influence the molecular weight distribution of the polymer [14]. Thus, I examined the four insertion patterns of 1-octene insertion: *trans*-1,2; *cis*-1,2; *trans*-2,1; and *cis*-2,1.

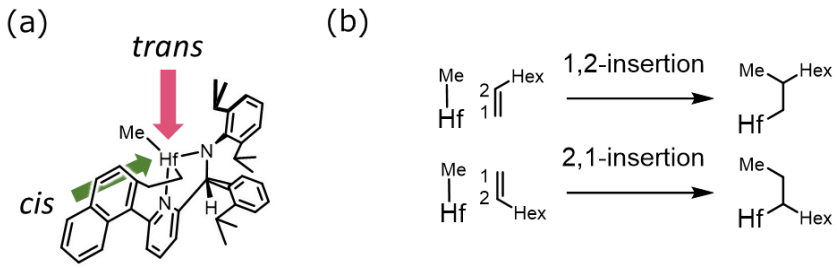

Figure 4. Schematic representations of (a) *trans*/*cis* and (b)1,2-/2,1-insertion to $HfCat^+$.

2.2.2. QM Calculations for Reaction Energetics

2.2.2.1. QM Model Preparation

To examine the influence of $MeB(C_6F_5)_3^-$ or $B(C_6F_5)_4^-$ on the 1-octene insertion process, I prepared two types of calculation models: Each of them consists of a 1-octene monomer and $HfCat^+$ with either $MeB(C_6F_5)_3^-$ or $B(C_6F_5)_4^-$ as CA. For each calculation model, the following six-step procedure was conducted: (i) MD simulations of the model system containing $HfCat^+$, CA, and 1-octene monomer (see Appendix A for details of the computational model and conditions) were performed to sample a wide

range of structures for the QM computational model of the monomer insertion reaction. (ii) A collection of 4000 structures was taken from the MD trajectory and classified into 80 representative configurations using the K-means clustering algorithm [66]. (iii) By performing QM calculations for these 80 structures, the five most stable structures for each insertion pattern were selected (in total, 20 structures), including the minimum-energy state (MS) structure. (v) Using these 20 structures as initial structures, the transition state structures of the four insertion patterns are searched for by using QM calculation. (vi) The most stable transition state (TS) structure was determined for each of the four insertion patterns. From this structure, the reactant state (RS) was obtained by IRC calculations, followed by structural optimizations. The most stable product structures obtained from the IRC calculation was defined as the product state (PS) structure.

2.2.2.2. QM Calculation

All QM calculations were performed with the Gaussian16 package [67]. Geometrical optimizations were conducted under vacuum using the M06 functional [68,69]. The LanL2DZ basis set with the associated effective core potential and additional f orbitals was used for Hf atom, and the standard 6-31G(d,p) basis set was used for the other atoms. Frequency analyses were carried out to confirm that each structure is a local minimum (i.e., no imaginary frequency) or a transition state (i.e., only one imaginary frequency). IRC calculations of the obtained transition states were performed to confirm the connectivity of the TSs to RSs and PSs. The energies of the optimized structures were further estimated through single-point calculations in the

toluene solvent with SMD model [70], using the M06 functional and the def2-TZVPP basis set for all the atoms. The Gibbs free energy of each optimized structure was calculated including thermal correction. The basis set superposition error (BSSE) correction with the counterpoise method of Boys and Bernardi [71,72] was included in the cation–anion interaction energies.

2.2.3. REMD Calculations for Free Energy Surfaces

2.2.3.1. Model System for REMD Calculations

To investigate the relationship between coordination of the 1-octene monomers and dissociation of the CAs, the following two model systems I and II were prepared for each REMD calculation in the cases of the $HfCat^{+}$–$MeB(C_6F_5)_3^{-}$ and $HfCat^{+}$–$B(C_6F_5)_4^{-}$ IP complexes, referring to our previous work [64]. Model system I consists of one IP and 180 solvent toluene molecules, while model system II consists of one IP, 50 1-octene molecules, and 100 solvent toluene molecules. The box sizes of the $HfCat^{+}$–$MeB(C_6F_5)_3^{-}$ and $HfCat^{+}$–$B(C_6F_5)_4^{-}$ IP model systems (for both I and II) were $(32.7\ Å)^3$ and $(32.5\ Å)^3$, respectively. The concentrations of 1-octene monomers in the $HfCat^{+}$–$MeB(C_6F_5)_3^{-}$ and $HfCat^{+}$–$B(C_6F_5)_4^{-}$ IP model systems II were 2.38 mol/L and 2.41 mol/L, respectively, which were both about five times denser than the experimental conditions of 0.5 mol/L [14]. The simulation boxes used as model system II in this study are shown in **Figure 5**.

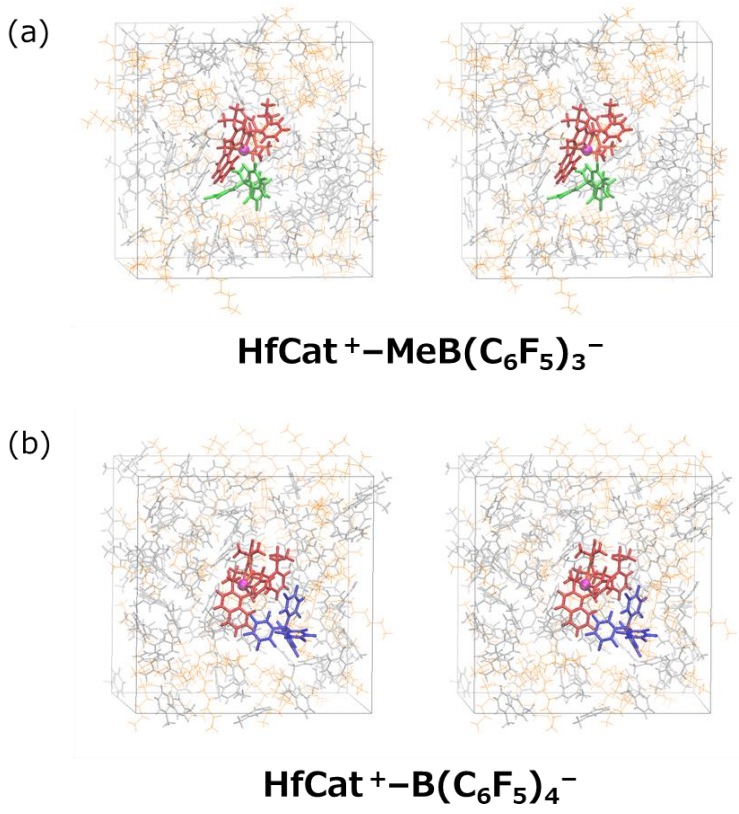

Figure 5. Side-by-side stereoviews of the model system II for (a) the $HfCat^{+}$–$MeB(C_6F_5)_3^{-}$ complex and (b) the $HfCat^{+}$–$B(C_6F_5)_4^{-}$ complex (red, $HfCat^{+}$; green, $MeB(C_6F_5)_3^{-}$; blue, $B(C_6F_5)_4^{-}$; orange, 1-octene; gray, toluene).

2.2.3.2. REMD Calculation Method

All REMD calculations [73] were executed using the pmemd module in AMBER14 [74] under the periodic boundary condition and the NVT condition. Each REMD calculation consisted of 18 replicas with temperatures ranging from 330 to 500 K. Only the trajectories at 330 K were used in our analysis. The temperatures of the replicas were distributed roughly exponentially to obtain uniform acceptance ratios between neighboring replicas. The replica exchange was attempted 50000 times every 1 ps (in total, 50 ns of MD trajectory). The weak-coupling algorithm with a time constant of 1

ps was applied to control the temperature. The integration time step was set to 1 fs, and the SHAKE algorithm was used to constrain the bond distances including hydrogen atoms.

The atomic charges were determined by the QM calculations with the Mertz–Singh–Kollman method [75,76]. The force field developed in our previous study [64] was used for the $HfCat^+$ molecule, and the general AMBER force field (GAFF) version 1.7 [77] was applied for all the other molecules. The Lennard-Jones (LJ) interaction parameters between the Hf atom and borate anion atoms developed in our previous study [64] were also used in the present study. Besides, the LJ interaction parameters between the Hf atom and the olefinic carbon atoms in 1-octene were developed in the same way with those between the Hf atom and carbon atoms in ethylene [64]. (**Table B1**, and see Appendix B for more details of the force field developments)

2.2.4. Kinetic Parameter Calculations

Table 1 shows the numerical values of k_a and K_d obtained from the QM and REMD calculations for the $HfCat^+$–$MeB(C_6F_5)_3^-$ and $HfCat^+$–$B(C_6F_5)_4^-$ IP systems. The former k_a values were evaluated by Eq. (1.5) with G_{TS} values obtained from the QM calculations, assuming the transmission coefficient κ was 1.0. The temperature was set to 323 K, referring to the previous experimental report of the 1-octene homopolymerization [14].

Following the definition that $HfCat^{Pn+}$ ($n \geq 0$) denoting $HfCat^+$ with a growing n-meric 1-octene polymer chain and 1-OCT denoting 1-octene monomer correspond respectively to A and B, the K_d value in Eq. (1.6) for

$$\mathrm{HfCat}^{\mathrm{P}n+} + \text{1-OCT} \underset{k_{\mathrm{d}}'}{\overset{K_{\mathrm{d}}}{\underset{\longleftarrow}{\overset{k_{\mathrm{d}}}{\longrightarrow}}}} \mathrm{HfCat}^{\mathrm{P}n+}\cdots\text{1-OCT}, \tag{2.1}$$

can be evaluated by the time duration of the $\mathrm{HfCat}^{\mathrm{P}n+}\cdots$1-OCT state with respect to all the observed time duration of the $\mathrm{HfCat}^{\mathrm{P}n+}$ state in the REMD trajectories, as follows,

$$K_{\mathrm{d}} = \frac{\sum_n [\mathrm{HfCat}^{\mathrm{P}n+}\cdots\text{1-OCT}]}{\left(\sum_n [\mathrm{HfCat}^{\mathrm{P}n+}] - \sum_n [\mathrm{HfCat}^{\mathrm{P}n+}\cdots\text{1-OCT}]\right)[\text{1-OCT}]} \equiv \frac{x}{(1-x)[\text{1-OCT}]}, \tag{2.2}$$

where x is defined as

$$x \equiv \frac{\sum_n [\mathrm{HfCat}^{\mathrm{P}n+}\cdots\text{1-OCT}]}{\sum_n [\mathrm{HfCat}^{\mathrm{P}n+}]}. \tag{2.3}$$

Table 1 shows the numerical values of K_{d} obtained from $[\mathrm{HfCat}^{\mathrm{P}0+}\cdots$1-OCT$]$ and $[\mathrm{HfCat}^{\mathrm{P}0+}]$ that can be evaluated from the REMD simulation assuming n = 0 in Eq. (2.2) and (2.3). I used the numerical values of 1-octene monomer concentration [1-OCT] and x shown in **Table 2**, reducing them by a scale factor of 1/5 to evaluate K_{d} because the values of [1-OCT] used in the present REMD calculations are five times larger than the experimental ones (see Subsection 2.2.3). Accordingly, the values of x in **Table 2** are expected to be five times larger than those in the experimental situations [14].

Table 1 also shows the numerical values of k_{d}, which were estimated, using Eq. (1.11), from the REMD calculation results of the HfCat^{+}–$\mathrm{MeB(C_6F_5)_3}^{-}$ and HfCat^{+}–$\mathrm{B(C_6F_5)_4}^{-}$ IP systems. Here, I assumed that the concentration of $\mathrm{HfCat}^{\mathrm{P}n+}$ (i.e., the chemical compound A in Eq. (1.9)) does not decrease during the CP reaction and is kept constant, i.e., $[\mathrm{HfCat}^{+}]_0$,

$$[\mathrm{A}]_t = [\mathrm{HfCat}^{+}]_0 = const. \tag{2.4}$$

Then, k_d was obtained as

$$k_d = \frac{\ln[1\text{-OCT}]_0 - \ln[1\text{-OCT}]_\tau}{[\mathrm{HfCat}^+]_0 \cdot \tau}, \tag{2.5}$$

where I estimated, from the REMD trajectories, the average time interval τ of association complex formation between $HfCat^+$ and 1-octene molecules and the 1-octene concentration at τ ($[1\text{-OCT}]_\tau$) after one 1-octene monomer had been inserted to the $HfCat^+$ in the model system.

Table 1. Rate constants k_a and k_d, and equilibrium constant K_d for $HfCat^+$–$MeB(C_6F_5)_3^-$ and $HfCat^+$–$B(C_6F_5)_4^-$ IP systems (see Section 1.2 for the definitions of these terms).

complex	k_a (s^{-1})	K_d ($L \cdot mol^{-1}$)	k_d ($L \cdot mol^{-1} \cdot s^{-1}$)
$HfCat^+$–$MeB(C_6F_5)_3^-$	8.7×10^{0}	1.4×10^{-1}	5.8×10^{10}
$HfCat^+$–$B(C_6F_5)_4^-$	5.6×10^{0}	3.6×10^{-1}	1.7×10^{11}

Table 2. Ratios of the $HfCat^+$ in association states with 1-octene in the REMD trajectories (x) and the 1-octene monomer concentration in the simulation boxes ([1-OCT]) in $HfCat^+$–$MeB(C_6F_5)_3^-$ and $HfCat^+$–$B(C_6F_5)_4^-$ IP systems.

complex	x	[1-OCT] ($mol \cdot L^{-1}$)
$HfCat^+$–$MeB(C_6F_5)_3^-$	0.32	2.38
$HfCat^+$–$B(C_6F_5)_4^-$	0.74	2.41

2.3. Results and Discussion

2.3.1. Energetics Influenced by the Counteranions $MeB(C_6F_5)_3^-$ and $B(C_6F_5)_4^-$

2.3.1.1. Favorable Pathway of 1-Octene Insertion Reaction: Structures and Energetics

Figure 6 shows the free energy diagrams of 1-octene insertion reaction in the $HfCat^+$–$MeB(C_6F_5)_3^-$ and $HfCat^+$–$B(C_6F_5)_4^-$ catalytic IP systems, together with their MS, RS, TS, and PS structures, both obtained from the QM calculations. The insertion patterns in the most stable reaction pathways (see the insertion patterns in Subsection 2.2.1) were *trans*-1,2 and *cis*-1,2 in the $HfCat^+$–$MeB(C_6F_5)_3^-$ and $HfCat^+$–$B(C_6F_5)_4^-$ complexes, respectively (**Table C1** and **C2**, and see Appendix C for the results of the other insertion patterns). The preference for *trans*-1,2 insertion in $HfCat^+$–$MeB(C_6F_5)_3^-$ complex is consistent with our previous report on propylene insertion reaction with this IP [65]. In contrast, the preference for *cis*-1,2 insertion in $HfCat^+$–$MeB(C_6F_5)_3^-$ complex is the same with the previous study where no CAs are included in the model system [13], which might be because of the weak coordinating ability of $B(C_6F_5)_4^-$. Hereafter, 3PFB and 4PFB will be appropriately used to denote $MeB(C_6F_5)_3^-$ (methyl**tris**(**p**er**f**luorophenyl)**b**orate) and $B(C_6F_5)_4^-$ (**tetrakis**(**p**er**f**luorophenyl)**b**orate), respectively, as well as in **Figure 6**.

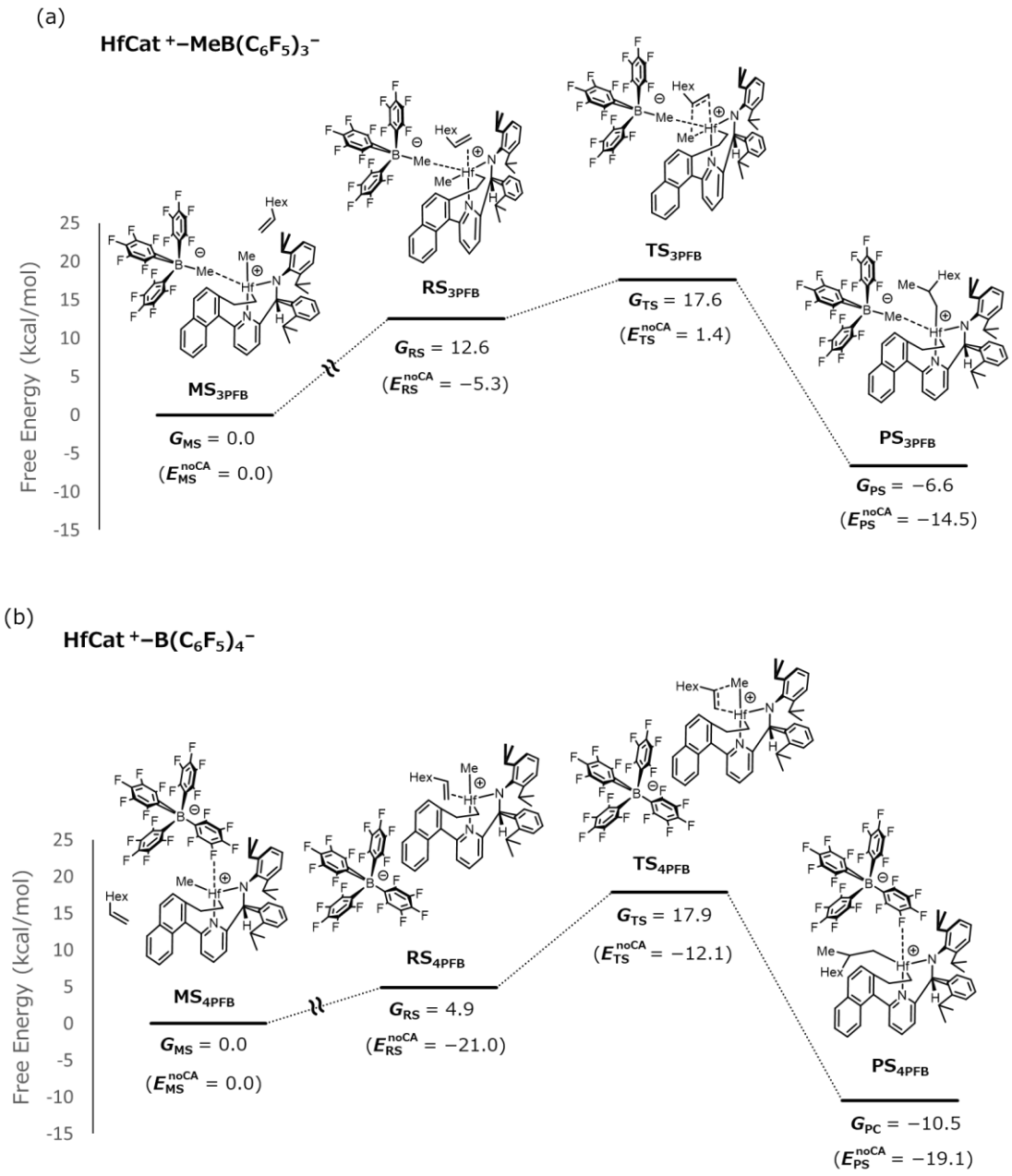

Figure 6. Free energy diagrams of 1-octene insertion reaction, together with the MS, RS, TS and PS structures of *trans*-1,2 and *cis*-1,2 insertion in (a) $HfCat^{+}$–$MeB(C_6F_5)_3^{-}$ and (b) $HfCat^{+}$–$B(C_6F_5)_4^{-}$ complexes, respectively. The energies E^{noCA}s show the single-point potential energies of the corresponding structures excluding the CAs from the IP complexes. *G*s and E^{noCA}s are the relative values to those in each MS. Herein "3PFB" and "4PFB" denote $MeB(C_6F_5)_3^{-}$ and $B(C_6F_5)_4^{-}$, respectively. Values are given in kcal/mol.

Initially, in MS_{3PFB} and MS_{4PFB} states, the $MeB(C_6F_5)_3^-$ and $B(C_6F_5)_4^-$ anions are both coordinated to the $HfCat^+$ with the Me group and with the F atom, respectively. Both catalyst structures are the penta-coordinated "inner-sphere" ion pairs (ISIPs) where the cation and anion are in close contact with each other [10,40], with the $MeB(C_6F_5)_3^-$ and $B(C_6F_5)_4^-$ anions being coordinated to $HfCat^+$ in *cis* and *trans* positions, respectively. This site difference should be because the latter anion is so bulky that its *cis* coordination is less stable due to the steric hindrance of the naphthyl and 2-isopropyl phenyl groups of the $HfCat^+$.

In the pathway from MSs to RSs for the considered catalyst system, the structure transformation like the backbone rearrangement (BBRA), as reported in the metallocene catalyst [63], was observed, which allows a monomer to enter the inner coordination sphere of the catalyst. It can be seen that monomers are located outside the coordination sphere in the MSs, while a monomer coordinate to Hf center and form the π-complexes in the RSs in the presence of both CAs. It is clarified here that the manner of the BBRA is largely dependent on the CAs [58] for this catalyst.

In the case of $HfCat^+$–$MeB(C_6F_5)_3^-$ complex, the $MeB(C_6F_5)_3^-$ anion keeps its coordination to the $HfCat^+$ from MS_{3PFB}, forming a hexa-coordination but keeping the ISIP structure in both RS_{3PFB} and TS_{3PFB}, as reported in the theoretical study on the propylene insertion reaction [65]. However, in the case of $HfCat^+$–$B(C_6F_5)_4^-$ complex, the $B(C_6F_5)_4^-$ anion is dissociated from the $HfCat^+$ in both RS_{4PFB} and TS_{4PFB}, keeping the penta-coordination of $HfCat^+$ but forming an "outer-sphere" ion pair (OSIP), where the cation and anion are rather separated each other [10,40]. In spite of this structural

difference, the G_{TS}s of the $HfCat^{+}$–$MeB(C_6F_5)_3^{-}$ and $HfCat^{+}$–$B(C_6F_5)_4^{-}$ complexes are 17.6 kcal/mol and 17.9 kcal/mol, respectively, almost in the same range.

However, finally in the PS_{3PFB} and PS_{4PFB} states, $MeB(C_6F_5)_3^{-}$ and $B(C_6F_5)_4^{-}$ are coordinated to the $HfCat^{+}$ in the *cis* and *trans* position with respect to the N atom in the pyridine ring, respectively, forming penta-coordinated ISIPs. Note that $B(C_6F_5)_4^{-}$ coordinates to $HfCat^{+}$ again. The G_{PS}s become –6.6 kcal/mol in the $HfCat^{+}$–$MeB(C_6F_5)_3^{-}$, and –10.5 kcal/mol in the $HfCat^{+}$–$B(C_6F_5)_4^{-}$ complex. It is worth noting that the overall reactions are exergonic for both cases.

2.3.1.2. Differences in ISIP/OSIP Structures of TSs (/RSs) between $HfCat^{+}$–$MeB(C_6F_5)_3^{-}$ and $HfCat^{+}$–$B(C_6F_5)_4^{-}$ Complexes: Trade-Offs between Conformation Transition Energy (CTE) and Ion Pair Dissociation Energy (IDE)

It is notable that some structural differences were observed in TSs (or RSs) between $HfCat^{+}$–$MeB(C_6F_5)_3^{-}$ and $HfCat^{+}$–$B(C_6F_5)_4^{-}$ complexes (**Figure 6**). In the former complex, the monomer is inserted via *trans*-1,2 pattern, whereas in the latter complex, *cis*-1,2 insertion is preferred. The reason for the preference for *trans*-1,2 in $HfCat^{+}$–$MeB(C_6F_5)_3^{-}$ is that its transition state of *cis*-1,2 insertion complex is an OSIP, where the electrostatic interaction between $HfCat^{+}$ and CA is weaker than ISIPs. Due to the steric repulsion between the naphthyl ring of the $HfCat^{+}$ and the hexyl chain of 1-octene monomer, I could not find any stable ISIP structure with 1-octene coordination in the *cis* position for the $HfCat^{+}$–$MeB(C_6F_5)_3^{-}$ complex. In contrast, the reason for the

preference for *cis*-1,2 insertion in $HfCat^{+}–B(C_6F_5)_4^{-}$ is that the structural stability of $HfCat^{+}$ with Me group at the *trans* position (with respect to the N atom in the pyridine ring) is more stable than that with Me group at the *cis* position by about 6 kcal/mol (see **Table D1** in Appendix D).

To elucidate the origin of the IP structure difference of TSs (or RSs) between the $HfCat^{+}–MeB(C_6F_5)_3^{-}$ and $HfCat^{+}–B(C_6F_5)_4^{-}$ complexes, I focused on the energy loss of the IP dissociation and that of the conformational transition of $HfCat^{+}$, associated with the ISIP/OSIP alternation. It can be assumed that the transformation from ISIP to OSIP leads to the unfavorable energy loss of the cation–anion electrostatic interaction, i.e., the ion pair dissociation energy (IDE). The transformation from OSIP to ISIP would lead to a favorable contribution by the electrostatic interaction energy between $HfCat^{+}$ and CAs (i.e., negative value of IDE). However, I found that the transformation from OSIP to ISIP inversely leads to an unfavorable energy contribution due to the distortion of the $HfCat^{+}$ from a penta-coordinated structure without coordination of CAs to a more sterically constrained hexa-coordinated one with coordination of CAs, i.e., the conformational transition energy (CTE). Therefore, in the present two catalytic IP complexes, it can be said that the IDE and CTE are assumed to be in a trade-off relationship, and their mutual compensation should be the key to determine the IP structures toward each TS (or RS) from each structural region of MS.

It was found that the IDEs of the $HfCat^{+}–MeB(C_6F_5)_3^{-}$ and $HfCat^{+}–B(C_6F_5)_4^{-}$ IPs are ~30 and ~5 kcal/mol, respectively (**Table E1**, and see Appendix E), while the CTE of $HfCat^{+}$ from a stable penta- to unstable hexa-coordinated configuration is ~20 kcal/mol (**Table D1**, and see Appendix D). It is, therefore, suggested that the hexa-

coordinated ISIP at TS_{3PFB} (or RS_{3PFB}) is more stable than its penta-coordinated OSIP because the IDE of the $HfCat^{+}$–$MeB(C_6F_5)_3^{-}$ (~30 kcal/mol) is larger than the CTE of the $HfCat^{+}$ (~20 kcal/mol). In contrast, the penta-coordinated OSIP at TS_{4PFB} (or RS_{4PFB}) is more stable than its hexa-coordinated ISIP because the CTE of the $HfCat^{+}$ (~20 kcal/mol) from the penta- to the hexa-coordinated configuration is larger than the IDE of the $HfCat^{+}$–$B(C_6F_5)_4^{-}$ (~5 kcal/mol).

2.3.1.3. G_{TS} in $HfCat^{+}$–$MeB(C_6F_5)_3^{-}$ Complex Almost Equal to That in $HfCat^{+}$–$B(C_6F_5)_4^{-}$ Complex despite the Structural Difference in TSs

The G_{TS} values of the $HfCat^{+}$–$MeB(C_6F_5)_3^{-}$ and the $HfCat^{+}$–$B(C_6F_5)_4^{-}$ complexes turned out almost equal to each other, i.e., 17.6 and 17.9 kcal/mol, respectively (**Figure 6**). To understand this coincidence despite the remarkable difference in the TS structures, it is worth elucidating if and how the following relation of energy decomposition should stand,

$$\Delta G = G_{TS} - G_{MS} \tag{2.6a}$$

$$\simeq (E_{TS}^{noCA} - E_{MS}^{noCA}) + (\Delta E_{TS}^{cation\text{-}anion} - \Delta E_{MS}^{cation\text{-}aniton}) \tag{2.6b}$$

$$= \Delta E^{noCA} + \Delta\Delta E^{cation\text{-}anion}, \tag{2.6c}$$

where E^{noCA} values denote the single-point potential energies of the structures containing only the $HfCat^{+}$ and 1-octene monomers, excluding the CAs from the IP

complexes while fixing the remaining geometries, and $\Delta E^{\text{cation–anion}}$ values are the corresponding cation–anion interaction energies without 1-octene monomers.

Figure 6 also shows such E^{noCA} values of the corresponding IP complexes, with each $E_{\text{MS}}^{\text{noCA}}$ of the $HfCat^{+}$–$MeB(C_6F_5)_3^{-}$ and the $HfCat^{+}$–$B(C_6F_5)_4^{-}$ complexes set to the origin of energy (0.0 kcal/mol). Note that $E_{\text{RS}}^{\text{noCA}}$ values are more stable than $E_{\text{MS}}^{\text{noCA}}$ values (see **Figure F1** in Appendix F). In the $HfCat^{+}$–$MeB(C_6F_5)_3^{-}$ complex, $E_{\text{TS}}^{\text{noCA}}$ of TS_{3PFB} showed a positive value of 1.4 kcal/mol since the destabilization energy due to the structure change of $HfCat^{+}$ from penta- (at MS_{3PFB}) to hexa-coordinated (at TS_{3PFB}) structure exceeds the stabilization energy by 1-octene coordination to $HfCat^{+}$. In contrast, in the $HfCat^{+}$–$B(C_6F_5)_4^{-}$ complex, it is reasonable that $E_{\text{TS}}^{\text{noCA}}$ of TS_{4PFB} is –12.1 kcal/mol because of the stabilization by the coordination of the 1-octene monomer to the $HfCat^{+}$ without any changes in the coordination number of $HfCat^{+}$. Accordingly, the large deviation of $E_{\text{TS}}^{\text{noCA}}$ values from G_{TS} values suggests that the CAs should play crucial roles in determining the G_{TS} energies. I found that such energy deviation of $E_{\text{TS}}^{\text{noCA}}$ stems from the changes in cation–anion interaction energies, $\Delta E^{\text{cation–anion}}$. That is, $\Delta E^{\text{cation–anion}}$ changes by 17.5 kcal/mol from MS_{3PFB} to TS_{3PFB} because the cation–anion interaction becomes relatively weaker in TS_{3PFB} owing to the influence of the 1-octene monomer coordination to $HfCat^{+}$ (**Table G1** in Appendix G). However, $\Delta E^{\text{cation–anion}}$ changes more largely by 26.4 kcal/mol from MS_{4PFB} to TS_{4PFB}, due to the IP dissociation, in addition to the influence of the 1-octene monomer coordination (**Table G2** in Appendix G). Thus, it is understood that the changes in $\Delta E^{\text{cation–anion}}$ of the IP complexes

make G_{TS} values of the HfCat^{+}–MeB(C$_6$F$_5$)$_3^{-}$ and the HfCat^{+}–B(C$_6$F$_5$)$_4^{-}$ complexes almost equal.

To sum up, the origin of the structural difference in TSs is attributed to the IDEs of HfCat^{+}–MeB(C$_6$F$_5$)$_3^{-}$ and HfCat^{+}–B(C$_6$F$_5$)$_4^{-}$ IPs (about 30 kcal/mol and 5 kcal/mol). However, it is characteristic that the G_{TS} values for both complexes are almost the same because the changes in the cation–anion interaction energies from MSs to TSs, i.e., $\Delta\Delta E^{\text{cation-anion}}$s, eventually cancel out, in a compensatory way, the energy difference of ΔE^{noCA} between in the HfCat^{+}–MeB(C$_6$F$_5$)$_3^{-}$ and HfCat^{+}–B(C$_6$F$_5$)$_4^{-}$ complexes.

2.3.2. Competition of Anion vs. Monomer Coordination to HfCat^{+}

2.3.2.1. Four Characteristic Regions on Free Energy Surfaces (FESs)

In Subsection 2.3.1, it was understood from the QM calculations that the electronic aspect of the IP structures in the course of the activation process is significantly different between the HfCat^{+}–MeB(C$_6$F$_5$)$_3^{-}$ and the HfCat^{+}–B(C$_6$F$_5$)$_4^{-}$ complexes. Likewise, it is reasonable to assume that a dynamic aspect of the IP structure during the diffusion process also influences the monomer capture step, where monomers approach the active center of HfCat^{+}, i.e., the initiating process that triggers the following process from the MS state toward TS through the RS state.

Thus, in order to investigate the characteristic change of the IP structure in the presence or absence of 1-octene monomers, I performed REMD calculations using the model system I (without 1-octene monomers) and II (with 1-octene monomers) for both $HfCat^{+}$–$MeB(C_6F_5)_3^{-}$ and $HfCat^{+}$–$B(C_6F_5)_4^{-}$ complexes (see Subsection 2.2.3 for the details of the REMD simulations). Thus, in order to investigate the characteristic change of the IP structure in the presence or absence of 1-octene monomers, I performed REMD calculations using the model system I (with 1-octene monomers) and II (without 1-octene monomers) for both $HfCat^{+}$–$MeB(C_6F_5)_3^{-}$ and $HfCat^{+}$–$B(C_6F_5)_4^{-}$ complexes (see Subsection 2.2.3 for the details of the REMD simulations). Then, to draw characteristic free energy surfaces (FESs) using the obtained REMD trajectories, the interatomic distance r between Hf and B atoms and the angle ϕ formed between the straight lines connecting Hf to B and Me (**Figure 7**) were taken as the two coordinates to map the FESs. To distinguish the anion location relative to the $HfCat^{+}$ on the 2-dimensional free energy (FE) maps, it was convenient to divide the FE maps into the four characteristic regions; i) Region A satisfying 4 Å < r < 5 Å and 40° < ϕ < 100°, ii) Region B satisfying 5 Å < r < 7 Å and 20° < ϕ < 100°, iii) Region C satisfying 7 Å < r < 10 Å and 20° < ϕ < 100°, and iv) Region D satisfying 7 Å < r < 10 Å and 100° < ϕ < 180°.

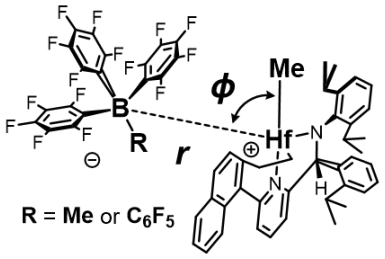

Figure 7. Definition of the distance r and the angle ϕ.

2.3.2.2. ISIPs Mainly Observed on the FESs of $HfCat^{+}$–$MeB(C_6F_5)_3^{-}$ Complex in the Presence or Absence of Monomers

Figure 8 shows the FE maps of the systems I and II for the $HfCat^{+}$–$MeB(C_6F_5)_3^{-}$ complex, which can be assumed to correspond almost to MS_{3PFB} and its surrounding states closer toward RS_{3PFB} (see **Figure 6(a)**). In addition, **Figure 9** shows the four typical catalyst structures $\mathbf{a}_{3PFB}$, $\mathbf{b}_{3PFB}$, $\mathbf{c'}_{3PFB}$, and $\mathbf{d'}_{3PFB}$ that appeared in the defined four regions A-D. In the FE map of system I (**Figure 8(a)**), the states of the complex are distributed in the regions A and B, where the ISIP structures $\mathbf{a}_{3PFB}$ and $\mathbf{b}_{3PFB}$ are observed with Me group and F atom coordinated to $HfCat^{+}$, respectively (**Figure 9**). It is understood that the structure $\mathbf{a}_{3PFB}$ is more energetically stable than the structure $\mathbf{b}_{3PFB}$, which corresponds to the fact that the Me group is coordinated to the $HfCat^{+}$ in MS_{3PFB}, obtained by the QM calculation in Subsection 2.3.1 (**Figure 6 (a)**).

In the FE map of system II for the $HfCat^{+}$–$MeB(C_6F_5)_3^{-}$ complex (**Figure 8(b)**), the states of the complex are distributed in all the regions A–D. As observed in system I (**Figure 8(a)**), region A is the most stable among them. In regions A and B, the ISIP structures $\mathbf{a}_{3PFB}$ and $\mathbf{b}_{3PFB}$ are respectively observed with no 1-octene monomer coordination to $HfCat^{+}$ (**Figure 9**). In regions C and D, the OSIP structures $\mathbf{c'}_{3PFB}$ and $\mathbf{d'}_{3PFB}$ are observed, where 1-octene monomers are coordinated to $HfCat^{+}$, instead of $MeB(C_6F_5)_3^{-}$ anions (**Figure 9**). Meanwhile, it should be noted that in these regions,

~35% of those structures are also observed without 1-octene monomer coordination to $HfCat^{+}$ (not shown in **Figure 9**).

From the above results, I determined the structural transition process of the $HfCat^{+}$–$MeB(C_6F_5)_3^{-}$ IP along with the coordination of 1-octene monomer (**Figure 9**). Herein, the chemical equilibrium between the structure $\mathbf{a}_{\mathbf{3PFB}}$ and structure $\mathbf{b}_{\mathbf{3PFB}}$ is biased toward the structure $\mathbf{a}_{\mathbf{3PFB}}$. When a 1-octene monomer approaches the IP complex, the $MeB(C_6F_5)_3^{-}$ anion in the structure $\mathbf{b}_{\mathbf{3PFB}}$ dissociates from $HfCat^{+}$ to form the structure $\mathbf{c'}_{\mathbf{3PFB}}$. Then, the $MeB(C_6F_5)_3^{-}$ anion moves to the opposite side from the active site to form the structure $\mathbf{d'}_{\mathbf{3PFB}}$. It is worth noting that this structural transition mechanism is essentially identical to that of the associative active site opening (AASO) mechanism reported in our previous study on the activation process with ethylene monomers [64].

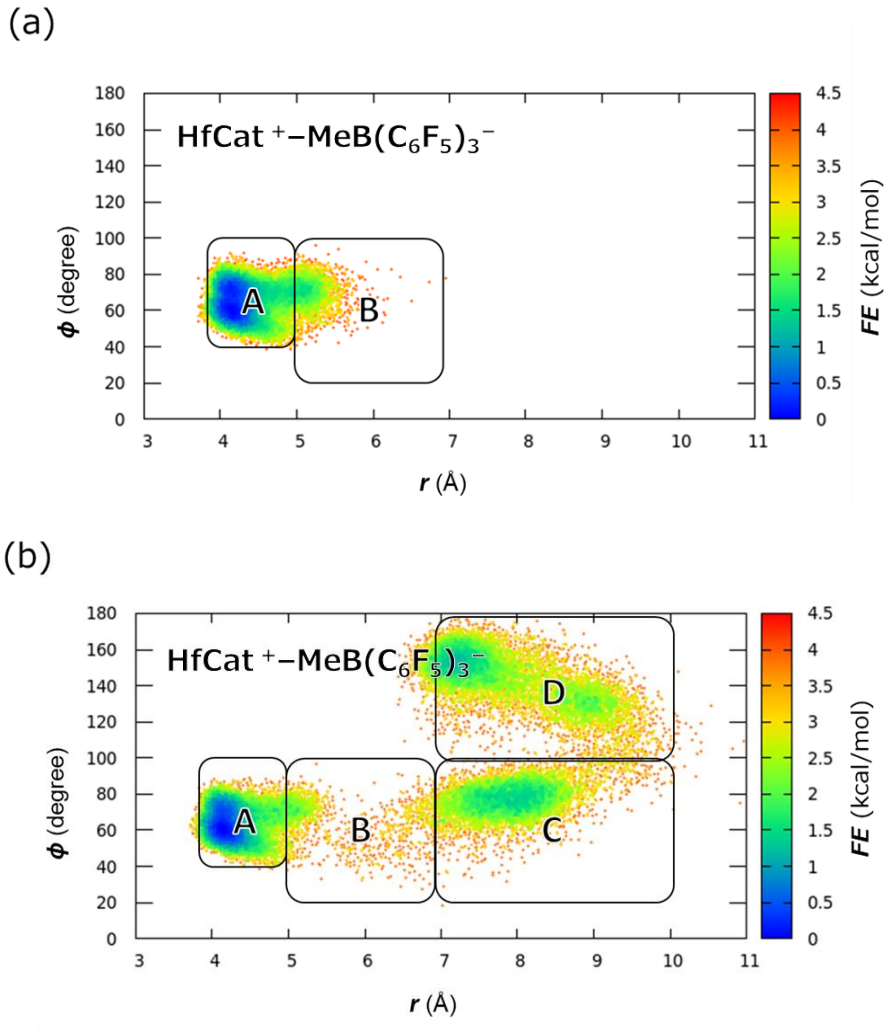

Figure 8. Free energy maps with respect to r and ϕ for the $HfCat^{+}$–$MeB(C_6F_5)_3^{-}$ complex; (a) system I (without 1-octene) and (b) system II (with 1-octene). The free energy at the most stable point in region A is set to the origin of energy (0.00 kcal/mol). Calculations were performed by using bins with size of (0.05 Å, 2.0 deg.).

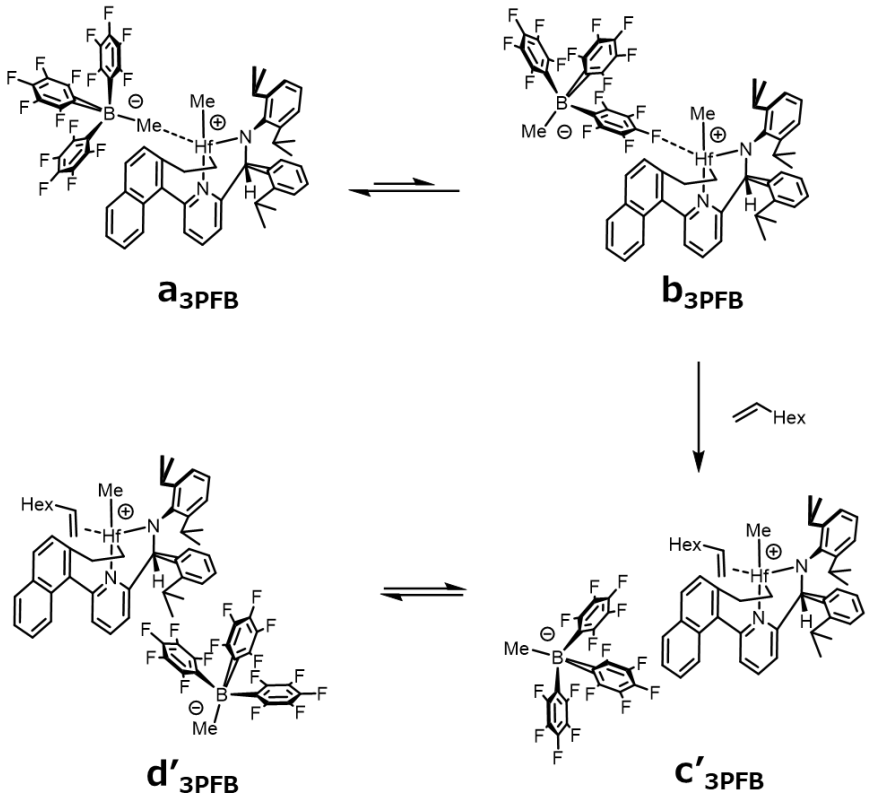

Figure 9. Schematic images of the structure transition of the IPs in the 1-octene coordination process with $MeB(C_6F_5)_3^-$. The structures **a**$_{\mathbf{3PFB}}$, **b**$_{\mathbf{3PFB}}$, **c'**$_{\mathbf{3PFB}}$, and **d'**$_{\mathbf{3PFB}}$ are the representative structures of regions A–D in Figure 8(a) and 8(b), respectively.

2.3.2.3. ISIPs Mainly Observed in the Absence of Monomers while OSIPs Observed Only in the Presence of Monomers in the FESs of $HfCat^+$–$B(C_6F_5)_4^-$ Complex

Figure 10 shows the FE maps of systems I and II for the $HfCat^+$–$B(C_6F_5)_4^-$ complex, which can be assumed to correspond almost to MS_{4PFB} and its surrounding states closer toward RS_{4PFB} (see **Figure 6(b)**). In addition, **Figure 11** shows the four typical catalyst

structures **b$_{4PFB}$**, **c$_{4PFB}$**, **c'$_{4PFB}$** and **d'$_{4PFB}$** that appeared out of the defined four regions A-D. In the FE maps of system I (**Figure 10(a)**), the states of the complex are distributed in regions B and C, where the ISIP structure **b$_{4PFB}$** and the OSIP structure **c$_{4PFB}$** are observed, respectively (**Figure 11**). Herein region A is not observed because the $B(C_6F_5)_4^-$ anion does not have a Me group. It is understood that the structure **b$_{4PFB}$** is more energetically stable than the structure **c$_{4PFB}$**, which corresponds to the fact that F atom is coordinated to $HfCat^+$ in the state MS_{4PFB}, obtained by the QM calculation in Subsection 2.3.1 (**Figure 6 (b)**).

In the FE map of system II (**Figure 10(b)**) for the $HfCat^+$–$B(C_6F_5)_4^-$ complex, the states of the complex are distributed in regions C and D. Compared to the FE map of system I (**Figure 10(a)**), it is clarified that region B has disappeared, that is, the ISIP structures are no longer observed, which suggests that the IP separation would be further promoted by the monomers present in the solvent. In regions C and D, the OSIP structures **c'$_{4PFB}$** and **d'$_{4PFB}$** are observed, where 1-octene monomers are coordinated to $HfCat^+$, instead of $B(C_6F_5)_4^-$ anions (**Figure 11**). Meanwhile, it should be noted that in these regions, ~35% of those structures are also observed without 1-octene monomer coordination to $HfCat^+$ (not shown in **Figure 11**).

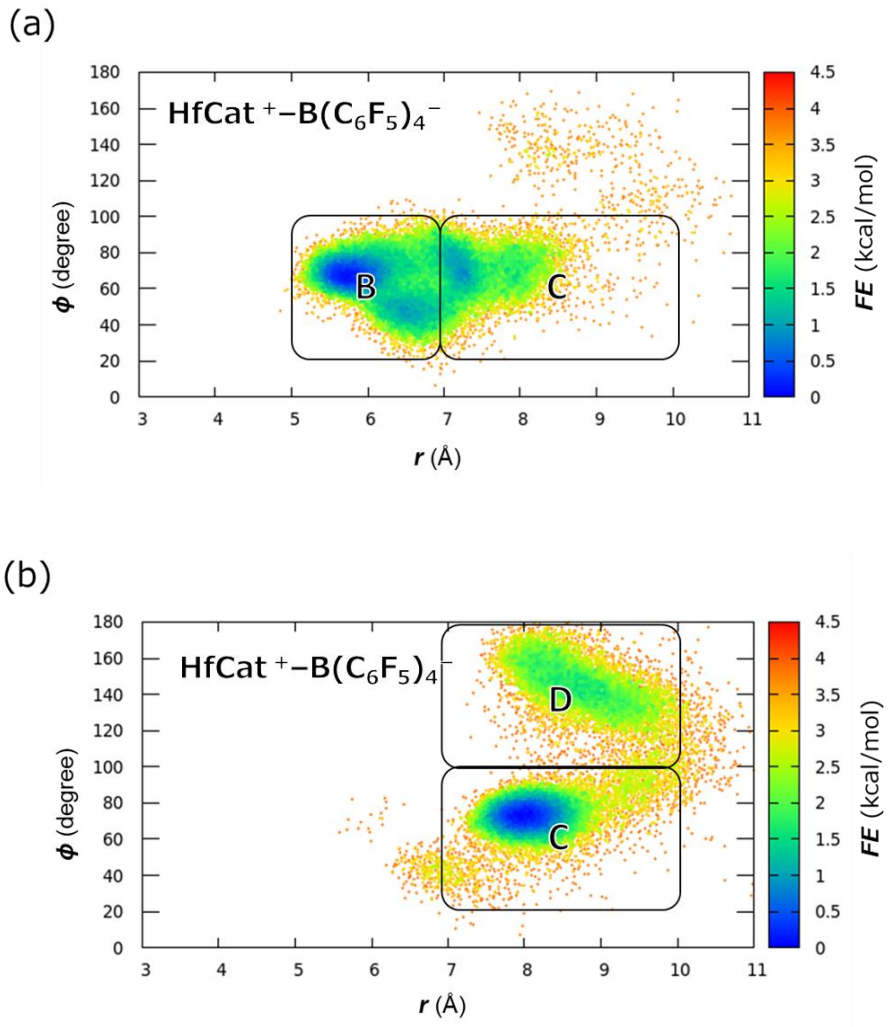

Figure 10. Free energy maps with respect to r and ϕ for the $HfCat^{+}$–$B(C_6F_5)_4^{-}$ complex; (a) system I (without 1-octene) and (b) system II (with 1-octene). The free energy at the most stable point in (a) region B and (b) region C are set to the origin of energy (0.00 kcal/mol), respectively. Calculations were performed by using bins with size of (0.05 Å, 2.0 deg.).

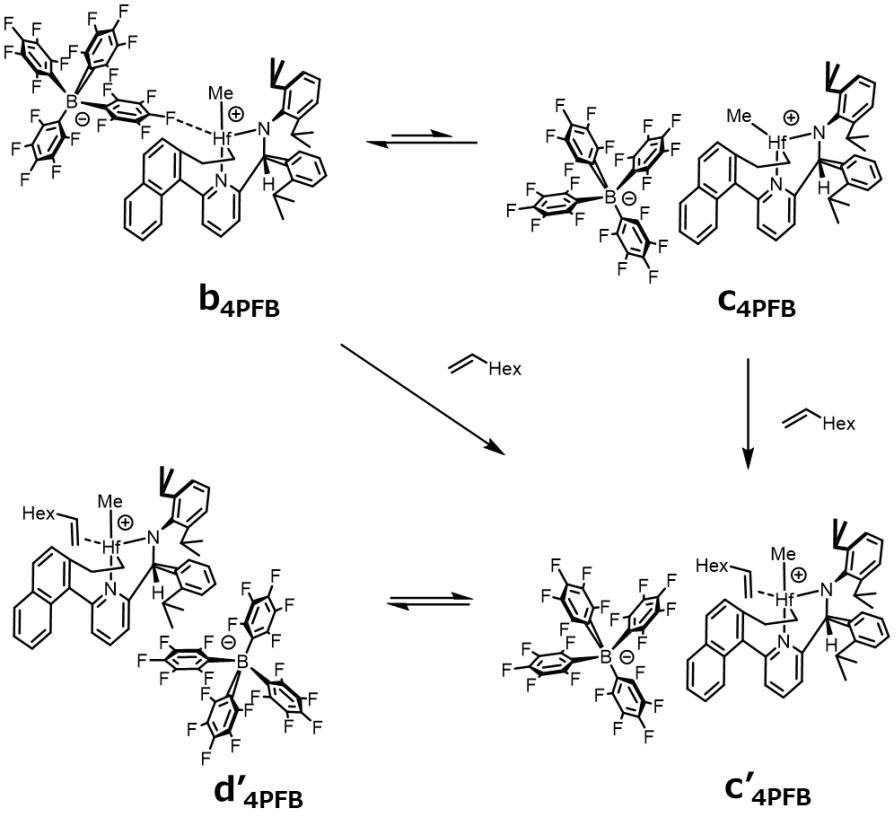

Figure 11. Schematic images of the structure transition of the ion pairs in the 1-octene coordination process in $HfCat^{+}$–$B(C_6F_5)_4^{-}$ complex. The structures **b4PFB**, **c4PFB**, **c'4PFB**, and **d'4PFB** are the representative structures of the regions B and C in Figure 10(a) and regions C and D in Figure 10(b), respectively.

Accordingly, I can confirm the structural transition process of the $HfCat^{+}$–$B(C_6F_5)_4^{-}$ IP along with the coordination of 1-octene monomer (**Figure 11**). The chemical equilibrium between the ISIP structure **b4PFB** and the OSIP structure **c4PFB** is strongly biased toward the structure **b4PFB**. When a 1-octene monomer approaches the complex, the $B(C_6F_5)_4^{-}$ anion in the ISIP structure **b4PFB** dissociates from $HfCat^{+}$ in accordance with 1-octene monomer coordination to form the OSIP structure **c'4PFB**. Furthermore, **c4PFB** becomes **c'4PFB** after 1-octene coordination to $HfCat^{+}$, keeping the OSIP structure. Then, the $B(C_6F_5)_4^{-}$ anion moves to the opposite side from the active site to form the

OSIP structure **d'$_{4PFB}$**. Once more, I would like to mention that this structural transition mechanism reminds us of the AASO mechanism that was reported in our previous study on the activation process [64], suggesting that the $B(C_6F_5)_4^-$ anion, which coordinates to $HfCat^+$ only with a weakly coordinating F atom, is more likely to dissociate from $HfCat^+$ than the $MeB(C_6F_5)_3^-$ anion, which has a strongly coordinating Me group. The complete disappearance of the $HfCat^+$–$B(C_6F_5)_4^-$ ISIP structure in the presence of 1-octene monomers (**Figure 10(b)**), which is in contrast with the retention of the $HfCat^+$–$MeB(C_6F_5)_3^-$ ISIP structure (**Figure 8(b)**), suggests that the AASO mechanism is more likely to occur in the $HfCat^+$–$B(C_6F_5)_4^-$ complex than $HfCat^+$–$MeB(C_6F_5)_3^-$ one.

2.3.2.4. Ratio of the $HfCat^+$ Capturing 1-octene Monomers: Influenced by Anion Coordinating Ability to $HfCat^+$

Table 2 shows the ratio *x* (Eq. (2.3)) of the $HfCat^+$ capturing 1-octene monomers among all states of $HfCat^+$ observed in the REMD simulations, together with the values of the 1-octene concentration [1-OCT] in the $HfCat^+$–$MeB(C_6F_5)_3^-$ and $HfCat^+$–$B(C_6F_5)_4^-$ complex systems. For determining the association states, the following criteria were considered: The distances between the Hf atom and each of the two sp^2 carbon atoms in 1-octene are within those distances in the MS structures obtained from the QM calculation. It is revealed that the value of *x* in the $HfCat^+$–$B(C_6F_5)_4^-$ complex was ~2.5 times as large as that in the $HfCat^+$–$MeB(C_6F_5)_3^-$ complex, although the 1-octene monomer concentrations ([1-OCT]) were almost the same. This is because the $B(C_6F_5)_4^-$ anion is more likely to dissociate from $HfCat^+$ than $MeB(C_6F_5)_3^-$ anion, so that monomer coordination is less likely to compete with anion coordination.

2.3.3. Relationship between the Reaction Rates and the Microscopic Reaction Mechanisms

Kinetic constants k_a, K_d, and k_d were obtained based on the chemical kinetic formulation (see Subsection 2.2.4). Using these constants, I calculate the k_2 values for the $HfCat^+$–$MeB(C_6F_5)_3^-$ and $HfCat^+$–$B(C_6F_5)_4^-$ complexes and compare them with the experimental ones.

2.3.3.1. k_a, K_d, and k_d in $HfCat^+$– $B(C_6F_5)_4^-$ Complex Are Larger than Those in $HfCat^+$–$MeB(C_6F_5)_3^-$ Complex

It was found that the k_a value in the $HfCat^+$–$MeB(C_6F_5)_3^-$ complex is about 1.5 times larger than that of the $HfCat^+$–$B(C_6F_5)_4^-$ complex, while the K_d value of the $HfCat^+$–$B(C_6F_5)_4^-$ complex is ~2.5 times larger than that of the $HfCat^+$–$MeB(C_6F_5)_3^-$ complex (**Table 1**).

The calculated k_d value for the $HfCat^+$–$B(C_6F_5)_4^-$ system was about three times larger than that for the $HfCat^+$–$MeB(C_6F_5)_3^-$ system (**Table 1**). Compared to the theoretical association rate constant, k_d^{theo}, assuming a diffusion-controlled reaction of spherical particles in the law of mass-action [78] with the numerical diffusion coefficients of $HfCat^+$ and 1-octene molecules (**Table H1**, and see Appendix H), the present k_d values in **Table 1** are both close enough to that of k_d^{theo} that was obtained theoretically under the simple but essential approximation. Thus, it can be said that the present rather precise and characteristic difference in their numerical values is

reasonably obtained owing to the successful and microscopic description of the intermolecular interaction between 1-octene and $HfCat^{+}$.

2.3.3.2. Calculated k_2 Values Reproduced the Tendency of the Experimental Values: Difference in the Coordination Ability

Table 3 shows the values of the calculated reaction rate constants, $k_2^{calc\_act}$, assuming an activation-controlled reaction and $k_2^{calc\_diff}$ assuming a diffusion-controlled reaction, and that of the experimental one, k_2^{exp}. The values of $k_2^{calc\_act}$ and $k_2^{calc\_diff}$ are calculated from the results of k_a, K_d, and k_d shown in **Table 1** using Eq. (1.4) for the activation-controlled assumption and Eq. (1.8) for a diffusion-controlled assumption, respectively. The values of k_2^{exp} are calculated using the 1-octene monomer half-life $\tau_{1/2}$, which is reported in the experimental study [14] (see Appendix I).

It was found that the values of $k_2^{calc\_act}$ are comparatively closer to those of k_2^{exp}, especially in $HfCat^{+}$–$B(C_6F_5)_4^{-}$ system, whereas the values of $k_2^{calc\_diff}$ are significantly different from those of k_2^{exp} (**Table 3**). It is suggested, therefore, that the present CP reaction occurs in the activation-controlled scheme, which can be normally expected for such kinds of catalytic reactions with activation energies larger than ~3 kcal/mol.

Table 3. 1-Octene polymerization reaction rate constants, i) the experimental one k_2^{exp} ii) the computational one for activation-controlled reactions $k_2^{calc\_act}$, and iii) the computational one for diffusion-controlled reactions $k_2^{calc\_diff}$ in $HfCat^+$–$MeB(C_6F_5)_3^-$ and $HfCat^+$–$B(C_6F_5)_4^-$ complexes. Values are given in $L \cdot mol^{-1} \cdot s^{-1}$.

complex	k_2^{exp}	$k_2^{calc\_act}$	$k_2^{calc\_diff}$
$HfCat^+$–$MeB(C_6F_5)_3^-$	3.5×10^2	1.3×10^0	1.4×10^{11}
$HfCat^+$–$B(C_6F_5)_4^-$	5.6×10^2	2.0×10^0	3.1×10^{11}

Under the above suggestion, I can further assume that the slight deviation of $k_2^{calc\_act}$ values from k_2^{exp} ones should come from the following uncertain factors: the validities of calculation models, calculation methods, and reaction schemes. For example, although I have revealed that both $HfCat^+$–$MeB(C_6F_5)_3^-$ and $HfCat^+$–$B(C_6F_5)_4^-$ complexes take the ISIP structures at their MSs, it might not be the case for the $HfCat^{Pn+}$–$MeB(C_6F_5)_3^-$ or $HfCat^{Pn+}$–$B(C_6F_5)_4^-$ complex, having a bulky *n*-meric 1-octene polymer chain ($n \geq 1$) attached on $HfCat^+$. Probably, these complexes may also take OSIP structures, which I can expect would somehow improve the deviation of $k_2^{calc\_act}$ from k_2^{exp} in the $HfCat^+$–$MeB(C_6F_5)_3^-$ system. It is also plausible that further improvement must be obtained by changing the calculation model from "ethylene-inserted" active species to "1-octene-inserted" one, or reconsidering the reaction schemes. Moreover, it is well-known that the choice of the "level of theory" in QM calculation significantly influences the $k_2^{calc\_act}$ values. In particular, in an activation-controlled reaction, $k_2^{calc\_act}$ is approximated by a product of k_a and K_d (Eq. (1.4)), which are expressed by Eq. (1.6) using G_{TS} and by Eq. (2.2) using the ratio x of the $HfCat^+$ forming association complex with 1-octene monomer, respectively. Thus, it is understood that such values of $k_2^{calc\_act}$ being smaller than that of k_2^{exp} suggest that either

those G_{TS} values should be overestimated or x values should be underestimated. Under these assumptions, therefore, I should note that the agreement between the ratio of $k_2^{calc\_act}$ ($HfCat^+$–$B(C_6F_5)_4^-$/$HfCat^+$–$MeB(C_6F_5)_3^-$) and that of k_2^{exp}, i.e., ~1.6, might be fortuitous and need further careful examination, due to not only the uncertainty discussed above, but also to the uncertainty of k_2^{exp} estimation (see Appendix I).

From the QM calculation in Subsection 2.3.1 to see the electronic effect of the counteranions, I found that the G_{TS} values are almost identical in both $HfCat^+$–$MeB(C_6F_5)_3^-$ and $HfCat^+$–$B(C_6F_5)_4^-$ complexes in spite of the OSIP/ISIP difference in TSs (see **Figure 6**). From the REMD calculation in Subsection 2.3.2 to see the dynamic effect of the counteranions, I found that the ratio x of the concentration of $HfCat^+$ forming association complex with 1-octene monomers was ~2.5 times larger in $HfCat^+$–$B(C_6F_5)_4^-$ complex than that in $HfCat^+$–$MeB(C_6F_5)_3^-$ one (see **Table 2**) because $B(C_6F_5)_4^-$ is more likely to form the OSIP structure along with 1-octene monomer approaching $HfCat^+$ (see **Figure 8** and **Figure 10**). From the above discussion, it is proved that, although the reaction is activation-controlled, the K_d was responsible for k_2 of the $HfCat^+$–$B(C_6F_5)_4^-$ complex being larger than that of the $HfCat^+$–$MeB(C_6F_5)_3^-$ one, which becomes larger with the weaker coordination ability of CAs. It is, therefore, the monomer capture step observed in the REMD study, which is significantly influenced by the dynamic effect of counteranions, is the essential key factor to bring about the 1-octene polymerization reaction rate larger with the $B(C_6F_5)_4^-$ than with $MeB(C_6F_5)_3^-$ anions.

2.4. Concluding Remarks

In this study, the effects of $MeB(C_6F_5)_3^-$ and $B(C_6F_5)_4^-$ on the 1-octene polymerization reaction catalyzed by the ethylene-inserted cationic active species of the (pyridylamido)Hf(IV) catalyst (i.e., $HfCat^+$) were analyzed using computational chemistry methods. For comprehensive understanding of the reaction mechanism, I regarded a combination of the successive two processes of the diffusion and activation processes as the elementary reactions of this CP reaction of the $HfCat^+$ and 1-octene monomers.

First, I analyzed the microscopic mechanism of 1-octene insertion reaction throughout the activation process, using QM calculation. I found that the $MeB(C_6F_5)_3^-$ anion is coordinated to the $HfCat^+$ in its transition state (TS), forming an "inner-sphere" ion pair (ISIP) structure. However, the $B(C_6F_5)_4^-$ anion is separated from the $HfCat^+$ in its TS, forming an "outer-sphere" ion pair (OSIP) structure. In spite of these structural differences, the G_{TS} values in $HfCat^+$–$B(C_6F_5)_4^-$ and $HfCat^+$–$MeB(C_6F_5)_3^-$ complexes are almost the same due to the energy compensation from the cation–anion interaction, i.e., the electronic effect of the CAs, to cancel out the difference in the stabilities between penta- and hexa-coordination structures.

Next, I analyzed the dynamics of the $MeB(C_6F_5)_3^-$ and $B(C_6F_5)_4^-$ anions in the diffusion process by using replica exchange MD (REMD) calculation and investigated their difference characterized through their diffusion processes. Then, it was found that $B(C_6F_5)_4^-$ is more likely to dissociate from $HfCat^+$ to form OSIP than $MeB(C_6F_5)_3^-$, because of its weaker coordination ability, so that the coordination of monomer is less likely to compete with the coordination of $B(C_6F_5)_4^-$ anion than with that of

$MeB(C_6F_5)_3^-$ anion. Thus, it was found that, in REMD trajectories of the $HfCat^+$–$B(C_6F_5)_4^-$ complex, the time duration ratio x of $HfCat^+$ forming such association complexes with 1-octene monomers with respect to the time duration of isolated $HfCat^+$ was ~2.5 times as large as that of the $HfCat^+$–$MeB(C_6F_5)_3^-$ complex due to the dynamic effect of the CAs.

On the basis of the above calculation results, I calculated the values of the reaction rate constant for the polymerization, k_2, in the activation-controlled scheme and found them to be in good agreement with the experimental ones. Furthermore, it was revealed that the larger x value of $HfCat^+$–$B(C_6F_5)_4^-$ complex in the diffusion process leads to qualitatively reproducing the larger k_2 value for $HfCat^+$–$B(C_6F_5)_4^-$ than that for $HfCat^+$–$MeB(C_6F_5)_3^-$, which is brought about from the weaker coordination ability of $B(C_6F_5)_4^-$. Therefore, it is computationally confirmed that the coordination ability of CA in the dynamic aspect is the key factor in determining the polymerization reaction rate constant.

It is computationally clarified that the microscopic mechanism of 1-octene insertion reaction by $HfCat^+$ with $MeB(C_6F_5)_3^-$ and $B(C_6F_5)_4^-$ in both electronic and dynamic aspects using QM and REMD methods in combination. Above all, it was demonstrated that the monomer capture step [63], which is largely influenced by the dynamic effect of counteranions, determines the polymerization reaction rates in this catalytic system. I believe that this work might be the first example of numerically estimating the CP reaction rate constant by computationally simulating the reaction mechanism from both electronic and dynamic viewpoints.

Appendix A:

Details of MD Calculation to Sample the Desired Configurations for the QM Calculation

In order to sample the initial structures for the QM calculations, I performed NVT-MD simulations in vacuum for 1 ns at 800 K controlled by the weak-coupling algorithm with a time constant of 1 ps using AMBER14 [74]. In each calculation, I imposed harmonic constraints on the position of the 1-octene monomer to efficiently sample the four desired configurations of 1-octene monomer coordination: *trans*-1,2; *trans*-2,1; *cis*-1,2; and *cis*-2,1. I sampled the configurations every 1 ps from each trajectory, and obtained 1000 configurations for each monomer coordination pattern (in total, 4000 configurations).

In these simulations, I used the intramolecular force field parameters obtained in the previous study for ethylene-inserted active species, as well as those for the intramolecular force field of borate anion. For the intramolecular force field of ethylene and all the intermolecular force fields, I used the parameters of GAFF 1.7 [77].

Appendix B:

Details of Intermolecular Force Field Development for the $HfCat^{+}$–1-Octene Interaction

To describe the intermolecular interaction between the cationic $HfCat^{+}$ and 1-octene monomers, I modified the LJ parameters of Hf-(C_1 atom in 1-octene) and Hf-(C_2 atom

in 1-octene), with reference to our previous work [64]. For this purpose, I consider a system composed of a $HfCat^{+}$ and a 1-octene molecule. First, I performed QM partial optimizations with the constraint on either r_1: Hf-(C_1 atom in 1-octene) or r_2: Hf-(C_2 atom in 1-octene) (**Figure B1**), using each stable configuration of the four coordination patterns obtained by full geometry optimization as initial structures. The r_1 ranges from 2.6 to 6.0 Å and r_2 from 3.0 to 6.0 Å at intervals of 0.2 Å. Then, I performed MM partial optimizations starting from the obtained QM optimized configurations with the harmonic constraints on either r_1 or r_2. I defined an evaluation function S for fitting LJ parameters as follows:

$$S = \sum_X \frac{\sum_r \exp\{-(\Delta E^{QM}_{X,r} - \Delta E^{QM}_{X,\min})\}(\Delta\Delta E^{QM-MM}_{X,r})^2}{\sum_r \exp\{-(\Delta E^{QM}_{X,r} - \Delta E^{QM}_{X,\min})\}},$$

where

$$\Delta E^{\alpha}_{X,r} = E^{\alpha}_{X,r} - E^{\alpha}_{X,r_{\max}} \ (\alpha = \text{QM or MM}),$$

$$\Delta\Delta E^{QM-MM}_{X,r} = \Delta E^{QM}_{X,r} - \Delta E^{MM}_{X,r},$$

X is the index for coordination patterns, r is the index for distances, $r_{\max}$ is the index for the longest distance, and $E^{QM}_{X,\min}$ is the minimum value of $E^{QM}_{X,r}$.

By minimizing the S value, I optimized the LJ parameters of Hf-(C_1 atom in 1-octene) and Hf-(C_2 atom in 1-octene). As a result, the parameters in **Table B1** were obtained.

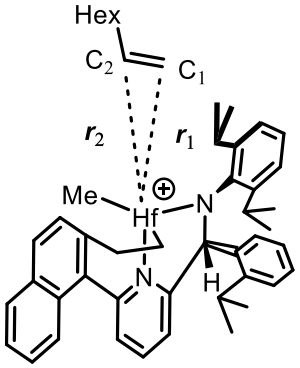

Figure B1. Schematic representation of the constraints on Hf-(C_1 atom in 1-octene) and Hf-(C_2 atom in 1-octene) distances.

Table B1. LJ parameters for Hf–C_1 and Hf–C_2 after modification.

	ε (kcal/mol)	σ (Å)
Hf–C_1	7.36	2.61
Hf–C_2	5.65	3.29

Appendix C:

Reaction Free Energies for All the Insertion Patterns

As I stated in Subsection 2.2.1, I have searched for the transition state structures of the expected four insertion patterns, *trans*-1,2; *trans*-2,1; *cis*-1,2; and *cis*-2,1. **Table C1** and **Table C2** show the obtained energies for four insertion patterns in $HfCat^+$–$MeB(C_6F_5)_3^-$ and $HfCat^+$–$B(C_6F_5)_4^-$ systems, respectively. The reaction pathway shown in **Figure 6(a)** corresponds to *trans*-1,2 insertion in the $HfCat^+$–$MeB(C_6F_5)_3^-$

complex, and that in **Figure 6(b)** corresponds to *cis*-1,2 insertion in the $HfCat^{+}$–$B(C_6F_5)_4^{-}$ complex.

Table C1. G^{TS} and G^{RS} values, which are the Gibbs free energies of TS and RS states relative to MS, in each configuration of 1-octene insertion reaction with $MeB(C_6F_5)_3^{-}$.

	trans-1,2	*cis*-1,2	*trans*-2,1	*cis*-2,1
G^{TS} (kcal/mol)	17.6	25.4	19.1	24.8
G^{RS} (kcal/mol)	12.6	13.5	10.2	15.2

Table C2. G^{TS} and G^{RS} values, which are the Gibbs free energies of TS and RS states relative to MS, in each configuration of 1-octene insertion reaction with $B(C_6F_5)_4^{-}$.

	trans-1,2	*cis*-1,2	*trans*-2,1	*cis*-2,1
G^{TS} (kcal/mol)	22.4	17.9	23.2	19.4
G^{RS} (kcal/mol)	15.3	13.0	21.1	11.8

Appendix D:

Conformation Transition Energy of $HfCat^{+}$ from Penta- to Hexa-coordinated Structure

To examine the conformation transition energy (CTE) of $HfCat^{+}$ from the penta- to hexa-coordinated configuration, I adopted $HfCat^{+}$_TS_{3PFB}, $HfCat^{+}$_$TS_{4PFB,cis}$, and $HfCat^{+}$_$TS_{4PFB,trans}$ (**Figure D1**) as model structures for the hexa- and penta-coordinated configurations, which are taken from the coordinates of the cationic

$HfCat^+$ in TS_{3PFB}, TS_{4PFB}, and the transition state of *trans*-1,2 insertion reaction in $HfCat^+$–$B(C_6F_5)_4^-$ complex (**Table C2**) respectively. Then, I performed QM single-point calculations for these configurations at the M06/def2-TZVPP level of theory. I also performed geometry optimization of the cationic $HfCat^+$ at the M06/6-31G(d,p) (LanL2DZ+f for Hf atom) level of theory, followed by single-point calculation at the M06/def2-TZVPP level of theory. **Table D1** shows the obtained potential energies at the model structures relative to that of the optimized structure of cationic $HfCat^+$ set as 0.0 kcal/mol. From this result, I found that the CTE of $HfCat^+$ from the penta- to hexa-coordinated configuration is about 20 kcal/mol.

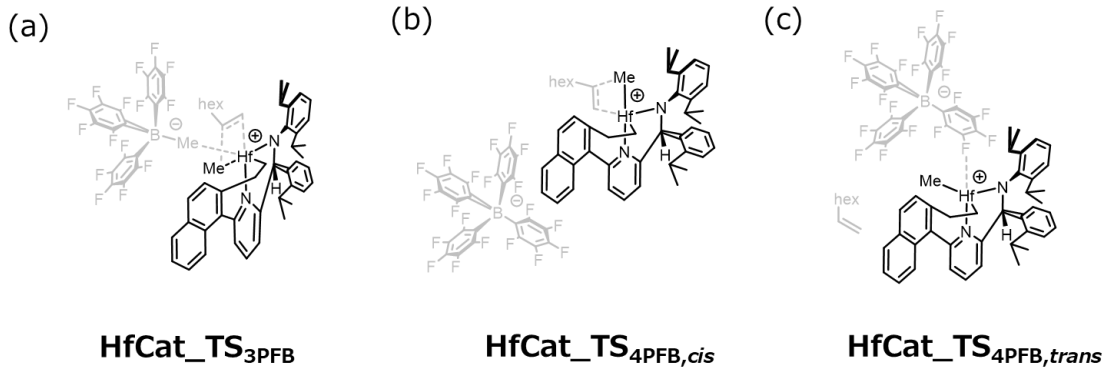

Figure D1. Structures of (a) $HfCat^+$_TS_{3PFB}, (b) $HfCat^+$_$TS_{4PFB,cis}$, and (c) $HfCat^+$_$TS_{4PFB,trans}$.

Table D1. Potential energies of $HfCat^+$_TS_{3PFB} and $HfCat^+$_TS_{4PFB} relative to the optimized structure of cationic $HfCat^+$.

	$HfCat^+$_TS_{3PFB}	$HfCat^+$_$TS_{4PFB,cis}$	$HfCat^+$_$TS_{4PFB,trans}$
E (kcal/mol)	39.3	19.2	25.5

Appendix E:

Ionpair Dissociation Energy of the $HfCat^{+}$–$MeB(C_6F_5)_3^{-}$ and the $HfCat^{+}$–$B(C_6F_5)_4^{-}$ Ionpairs

To examine the ionpair dissociation energies (IDEs), I considered the reference structures of TS'_{3PFB} (OSIP) and TS'_{4PFB} (ISIP) as shown in **Figure E1**, where the $HfCat^{+}$–$MeB(C_6F_5)_3^{-}$ and $HfCat^{+}$–$B(C_6F_5)_4^{-}$ IP configurations correspond to those in TS_{4PFB} (OSIP) and TS_{3PFB} (ISIP) in **Figure 6**, respectively. **Table E1** shows the values of the cation–anion interaction energy $\Delta E^{cation–anion}$ (= $E^{ionpair} – E^{cation} – E^{anion}$) in TSs and TS's, where $E^{ionpair}$, E^{cation}, and E^{anion} are the single-point calculated potential energies of the IP, cation, and anion, respectively. The difference of the $\Delta E^{cation–anion}$ values between the ISIP and OSIP complexes corresponds to the IDE, i.e., between TS_{3PFB} (ISIP) and TS'_{3PFB} (OSIP) (–81.0 kcal/mol and –50.8 kcal/mol), or between TS'_{4PFB} (ISIP) and TS_{4PFB} (OSIP) (–60.7 kcal/mol and –54.9 kcal/mol). Thus, the IDEs of the $HfCat^{+}$–$MeB(C_6F_5)_3^{-}$ and $HfCat^{+}$–$B(C_6F_5)_4^{-}$ IPs are estimated as ~30 kcal/mol and ~5 kcal/mol, respectively.

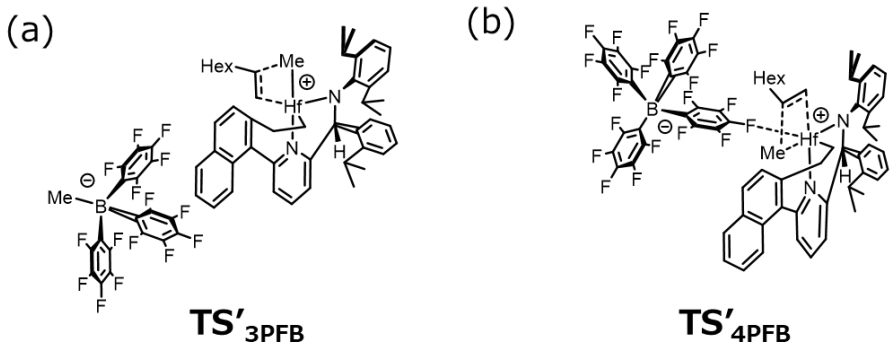

Figure E1. Structures of (a) TS'$_{3PFB}$ and (b) TS'$_{4PFB}$, whose catalyst configurations correspond to those of TS_{4PFB} and TS_{3PFB}.

Table E1. Cation–anion interaction energies $\Delta E^{cation–anion}$ in TS and TS' structures of $HfCat^+$–$MeB(C_6F_5)_3^-$ and $HfCat^+$–$B(C_6F_5)_4^-$ complexes.

	TS_{3PFB}	TS'$_{3PFB}$	TS_{4PFB}	TS'$_{4PFB}$
$\Delta E^{cation–anion}$ (kcal/mol)	-81.0	–50.8	-54.9	–60.7

Appendix F

Potential Energies of the Structures without CAs in $HfCat^+$–$MeB(C_6F_5)_3^-$ and $HfCat^+$–$B(C_6F_5)_4^-$ Complexes

Figure F1 shows the potential energy diagrams of E^{noCA}'s, which are the single-point potential energies of the structures containing only the $HfCat^+$ and 1-octene monomers, excluding the CAs from the IP complexes while fixing the remaining geometries of MSs, RSs, TSs, and PSs. Herein E^{noCA}'s are the relative values to the E^{noCA}' in MS_{3PFB}, while E^{noCA}s is **Figure 6** are the relative values to those in each MSs.

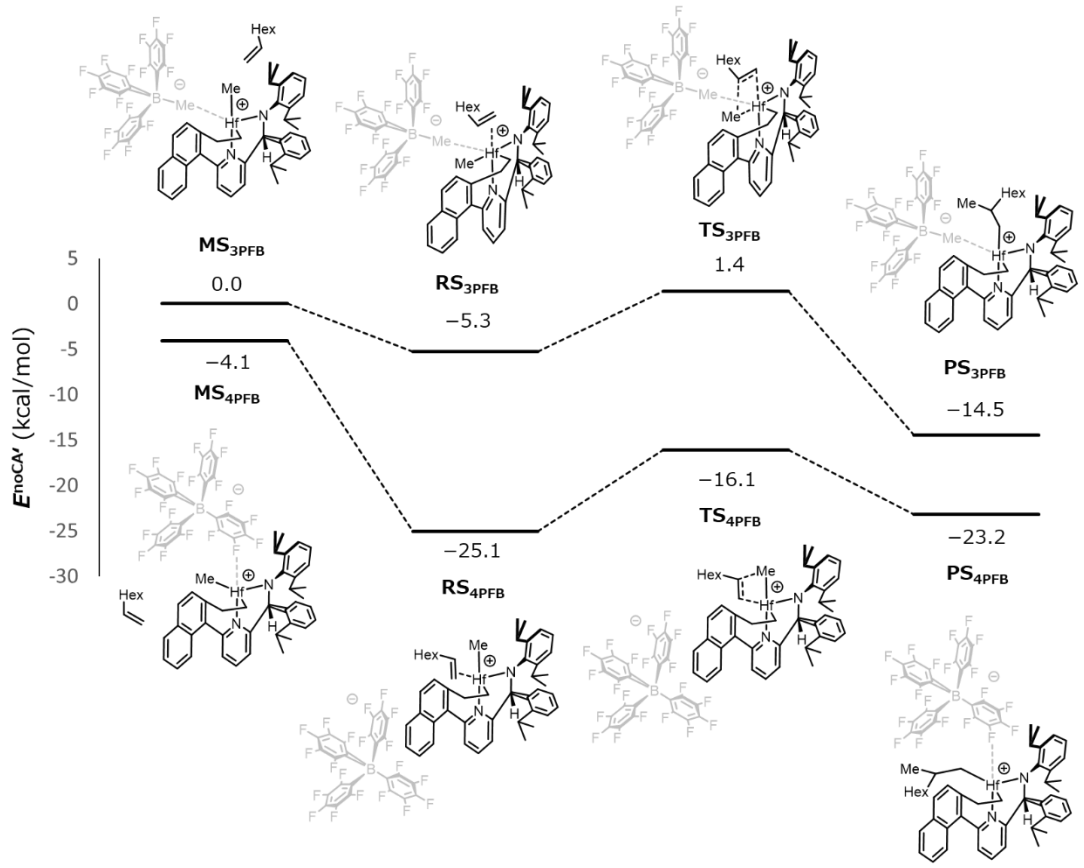

Figure F1. Potential energy diagrams of the MSs, RSs, TSs, and PSs in **Figure 6** without CAs in $HfCat^+$–$MeB(C_6F_5)_3^-$ and $HfCat^+$–$B(C_6F_5)_4^-$ complexes. E^{noCA}'s are the relative values to the energy in MS_{3PFB}. Herein "3PFB" and "4PFB" denote $MeB(C_6F_5)_3^-$ and $B(C_6F_5)_4^-$, respectively. Values are given in kcal/mol.

Appendix G:

Cation–anion Interaction Energies of the 1-octene Insertion Reaction Intermediates

Table G1 and **G2** shows the values of the cation–anion interaction energies $\Delta E^{cation–anion}$ (= $E^{ionpair} - E^{cation} - E^{anion}$) in MSs, RSs, TSs, and PSs of the $HfCat^+$–$MeB(C_6F_5)_3^-$ and $HfCat^+$–$B(C_6F_5)_4^-$ complexes, respectively.

Table G1. Cation–anion interaction energies $\Delta E^{\text{cation–anion}}$ in MS, RS, TS, and PS structures of $HfCat^{+}$–$MeB(C_6F_5)_3^{-}$ complex.

	MS_{3PFB}	RS_{3PFB}	TS_{3PFB}	PS_{3PFB}
$\Delta E^{\text{cation–anion}}$ (kcal/mol)	-98.5	–77.7	-81.0	–94.1

Table G2. Cation–anion interaction energies $\Delta E^{\text{cation–anion}}$ in MS, RS, TS, and PS structures of $HfCat^{+}$–$B(C_6F_5)_4^{-}$ complex.

	MS_{4PFB}	RS_{4PFB}	TS_{4PFB}	PS_{4PFB}
$\Delta E^{\text{cation–anion}}$ (kcal/mol)	-81.3	–56.8	-54.9	–57.4

Appendix H:

Theoretical Estimation of k_d^{theo} Based on the Smoluchowski's Equation on the Association Rate Constants of Spherical Particles at Mass-action Law Level

According to the work by Smoluchowski [78], the theoretical association rate constant in diffusion-controlled reaction of suspended spherical particles at the level of mass-action law is obtained by using the following equation:

$$k_d = 4\pi R^* N_A (D_X + D_Y), \quad \text{(H1)}$$

where effective radius R^* is the critical distance between the chemical species X and Y, N_A is the Avogadro constant, D_X and D_Y is the diffusion coefficients of X and Y, respectively.

For calculating the rate constant k_d in the present catalytic system, it is necessary to determine also the diffusion constants for $HfCat^+$ and 1-octene. For this purpose, I performed MD calculations for $HfCat^+$ and 1-octene. The model system consists of a $HfCat^+$ molecule, 40 1-octene molecules and 480 solvent toluene molecules and NVT-MD simulation was conducted for 1 μs. From the mean-square displacement (MSD) data obtained from the trajectory, I estimated the diffusion coefficients of $HfCat^+$ and 1-octene molecules.

By applying the obtained values of the diffusion coefficients to Eq. (H1), the association rate constant k_d was calculated, and is shown in **Table H1**, together with the diffusion constants of $HfCat^+$ and 1-octene, denoted as D_{HfC} and $D_{1\text{-}OCT}$. Here, the

effective radius R^* was set to 3.3 Å with reference to the distance between Hf atom and olefinic carbon atoms in the coordination structure obtained from the QM calculation of the 1-octene insertion reaction.

Table H1. Diffusion constants D_{HfC} and $D_{1\text{-}OCT}$, and the estimated association rate constant k_d based on the Eq. (H1) with the critical distance R^* 3.3 Å.

D_{HfC} ($m^2 \cdot s^{-1}$)	$D_{1\text{-}OCT}$ ($m^2 \cdot s^{-1}$)	k_d ($L \cdot mol^{-1} \cdot s^{-1}$)
1.86×10^{-9}	4.03×10^{-9}	1.47×10^{10}

Appendix I:

Theoretical Estimation of k_2^{exp}

To estimate the k_2^{exp}, I have assumed the second-order reaction

$$\mathrm{HfCat}^{Pn+} + \text{1-OCT} \xrightarrow{k_2} \mathrm{HfCat}^{P(n+1)+}, \tag{I1}$$

and k_2 can be estimated from the second-order reaction rate law as

$$k_2 = \frac{\ln[\text{1-OCT}]_0 - \ln[\text{1-OCT}]_{\tau_{1/2}}}{\int_0^{\tau_{1/2}} [\mathrm{HfCat}^{Pn+}]_t \, dt}, \tag{I2}$$

using the 1-octene monomer half-life $\tau_{1/2}$, which are 30 s and 60 s with $MeB(C_6F_5)_3^-$ and with $B(C_6F_5)_4^-$, respectively reported in the experiment [14]. Herein, the denominator in Eq. (I2) can be obtained from the integral of the active site concentration of Hf catalyst from $t = 0$ to $t = \tau_{1/2}$. Even though the manner of activation is different between in $MeB(C_6F_5)_3^-$ and in $B(C_6F_5)_4^-$ in the experiment [14], it is clearly shown that the active site count increases from ~30% to ~45% with $MeB(C_6F_5)_3^-$ due to the slow

initiation and decreases from ~60% to ~45% with $B(C_6F_5)_4^-$ due to the catalyst deactivation [82] from $t = 0$ to $t = \tau_{1/2}$.

Thus, I supposed that it is reasonable to assume the following equation

$$\int_0^{\tau_{1/2}} [\mathrm{HfCat}^{Pn+}]_t \, dt \simeq \tau_{1/2} [\mathrm{HfCat}^{Pn+}]_{\mathrm{ave.}}, \tag{I3}$$

to obtain the denominator in Eq. (I2). To approximately deal with the time-dependent concentration of $[\mathrm{HfCat}^{Pn+}]_t$, I solved Eq. (I2) and obtained the average active site concentrations of HfCat^{Pn+} ($[\mathrm{HfCat}^{Pn+}]_{\mathrm{ave.}}$) with $MeB(C_6F_5)_3^-$ and $B(C_6F_5)_4^-$ with 2 significant digits as 40% and 50% of the initial precatalyst concentration, respectively [14]. In this way, the intrinsic k_2^{exp} values can be estimated, which are comparable with our computational study within the present theoretical assumptions and computational approximations.

References

[1] Boussie, T. R.; Diamond, G. M.; Goh, C.; Hall, K. A.; LaPointe, A. M.; Leclerc, M.; Lund, C.; Murphy, V.; Shoemaker, J. A. W.; Tracht, U.; Turner, H.; Zhang, J.; Uno, T.; Rosen, R. K.; Stevens, J. C. *J. Am. Chem. Soc.* **2003**, *125*, 4306.

[2] Boussie, T. R.; Diamond, G. M.; Goh, C.; Hall, K. A.; LaPointe, A. M.; Leclerc, M. K.; Murphy, V.; Shoemaker, J. A. W.; Turner, H.; Rosen, R. K.; Stevens, J. C.; Alfano, F.; Busico, V.; Cipullo, R.; Talarico, G. *Angew. Chem., Int. Ed.* **2006**, *45*, 3278.

[3] Eagan, J. M.; Xu, J.; Di Girolamo, R.; Thurber, C. M.; Macosko, C. W.; LaPointe, A. M.; Bates, F. S.; Coates, G. W. *Science* **2017**, *355*, 814.

[4] Chum, P. S.; Swogger, K. W. *Prog. Polym. Sci.* **2008**, *33*, 797.

[5] Arriola, D. J.; Carnahan, E. M.; Hustad, P. D.; Kuhlman, R. L.; Wenzel, T. T. *Science* **2006**, *312*, 714.

[6] Wenzel, T. T.; Arriola, D. J.; Carnahan, E. M.; Hustad, P. D.; Kuhlman, R. L. *Top. Organomet. Chem.* **2009**, *26*, 65.

[7] Frazier, K. A.; Froese, R. D.; He, Y.; Klosin, J.; Theriault, C. N.; Vosejpka, P. C.; Zhou, Z.; Abboud, K. A. *Organometallics* **2011**, *30*, 3318.

[8] Zuccaccia, C.; Busico, V.; Cipullo, R.; Talarico, G.; Froese, R. D. J.; Vosejpka, P. C.; Hustad, P. D.; Macchioni, A. *Organometallics* **2009**, *28*, 5445.

[9] Froese, R. D. J.; Hustad, P. D.; Kuhlman, R. L.; Wenzel, T. T. *J. Am. Chem. Soc.* **2007**, *129*, 7831.

[10] Zuccaccia, C.; Macchioni, A.; Busico, V.; Cipullo, R.; Talarico, G.; Alfano, F.; Boone, H. W.; Frazier, K. A.; Hustad, P. D.; Stevens, J. C.; Vosejpka, P. C.; Abboud, K. A. *J. Am. Chem. Soc.* **2008**, *130*, 10354.

[11] Busico, V.; Cipullo, R.; Pellecchia, R.; Rongo, L.; Talarico, G.; Macchioni, A.; Zuccaccia, C.; Froese, R. D. J.; Hustad, P. D. *Macromolecules* **2009**, *42*, 4369.

[12] Niu, A.; Stellbrink, J.; Allgaier, J.; Richter, D.; Hartmann, R.; Domski, G. J.; Coates, G. W.; Fetters, L. J. *Macromolecules* **2009**, *42*, 1083.

[13] De Rosa, C.; Di Girolamo, R.; Talarico, G. *ACS Catal.* **2016**, *6*, 3767.

[14] Cueny, E. S.; Johnson, H. C.; Anding, B. J.; Landis, C. R. *J. Am. Chem. Soc.* **2017**, *139*, 11903–11912.

[15] Zhou, Z.; Stevens, J. C.; Klosin, J.; Qiu, X.; Redwine, D.; Cong, R.; Taha, A.; Mason, J.; Winniford, B.; Chauvel, P.; Montan, N. *Macromolecules* **2009**, *42*, 2291.

[16] Domski, G. J.; Lobkovsky, E. B.; Coates, G. W. *Macromolecules* **2007**, *40*, 3510.

[17] Domski, G. J.; Eagan, J. M.; De Rosa, C.; Di Girolamo, R.; LaPointe, A. M.; Lobkovsky, E. B.; Talarico, G.; Coates, G. W. *ACS Catalysis* **2017**, *7*, 6930.

[18] Johnson, H. C.; Cueny, E. S.; Landis, C. R. *ACS Catalysis* **2018**, *8*, 4178.

[19] Gao, Y.; Chen, X.; Zhang, J.; Chen, J.; Lohr, T. L.; Marks, T. J. *Macromolecules* **2018**, *51*, 2401.

[20] Cueny, E. S.; Landis, C. R. *ACS Catalysis* **2019**, *9*, 3338.

[21] Cueny, E. S.; Landis, C. R. *Organometallics* **2019**, *38*, 926.

[22] Yang, F.; Wang, X.; Ma, Z.; Wang, B.; Pan, L.; Li, Y. *Polymers* **2020**, *12*, 89.

[23] Rocchigiani, L.; Busico, V.; Pastore, A.; Talarico, G.; Macchioni, A. *Angew. Chem. Int. Ed.* **2014**, *53*, 2157–2161.

[24] Wang, S.; Wang, L.; Zhong, L.; Xu, R.; Wang, X.; Kang, W.; Gao, H. *Eur. Polym. J.* **2020**, *131*, 109709.

[25] Kulyabin, P. S.; Uborsky, D. V.; Voskoboynikov, A. Z.; Canich, J. A. M.; Hagadorn, J. R. *Dalton Trans.* **2020**, *49*, 6693.

[26] Kulyabin, P. S.; Goryunov, G. P.; Mladentsev, D. Y.; Uborsky, D. V.; Voskoboynikov, A. Z.; Canich, J. A. M.; Hagadorn, J. R. *Chem. Eur. J.* **2019**, *25*, 10478.

[27] Zaccaria, F.; Sian, L.; Zuccaccia, C.; Macchioni, A. In *Chapter One - Ion pairing in transition metal catalyzed olefin polymerization*; Prez, P. J., Ed.; Adv. Organomet. Chem.; Academic Press, 2020; Vol. 73; pp 1 – 78.

[28] Chen, E. Y.-X.; Marks, T. J. *Chem. Rev.* **2000**, *100*, 1391.

[29] Jngling, S.; Mlhaupt, R. *J. Organomet. Chem.* **1995**, *497*, 27.

[30] Santamki, S.; Aitola, E.; Kokko, E.; Repo, T.; Leskel, M.; Seppl, J. *Eur. Polym. J.* **2009**, *45*, 863.

[31] Jia, L.; Yang, X.; Stern, C. L.; Marks, T. J. *Organometallics* **1997**, *16*, 842.

[32] Sinn, H.; Kaminsky, W. *Adv. Organomet. Chem.* **1980**, *18*, 99.

[33] Sinn, H.; Kaminsky, W.; Vollmer, H. J.; Woldt, R. *Angew. Chem., Int. Ed. Engl.* **1980**, *19*, 390.

[34] Brintzinger, H. H.; Fischer, D.; Mülhaupt, R.; Rieger, B.; Waymouth, R. M. *Angew. Chem., Int. Ed. Engl.* **1995**, *34*, 1143.

[35] Alt, H. G.; Koppl, A. *Chem. Rev.* **2000**, *100*, 1205.

[36] Resconi, L.; Cavallo, L.; Fait, A.; Piemontesi, F. *Chem. Rev.* **2000**, *100*, 1253.

[37] Osakada, K.; Carpenter, B.; Ceroni, P.; Kirchner, B.; Landfester, K.; Leszczynski, J.; Luh, T. Y.; Perlt, E.; Polfer, N. C.; Salzer, R. *Organometallic Reactions and Polymerization*; 2014; Vol. 85.

[38] Bochmann, M. *J. Organomet. Chem.* **2004**, *689*, 3982.

[39] Chen, M.-C.; Roberts, J. A.; Marks, T. J. *J. Am. Chem. Soc.* **2004**, *126*, 4605.

[40] Wilson, P. A.; Hannant, M. H.; Wright, J. A.; Cannon, R. D.; Bochmann, M. *Macromol. Symp.* **2006**, *236*, 100.

[41] Bochmann, M.; Cannon, R. D.; Song, F. *Kinet. Catal.* **2006**, *47*, 160.

[42] Rapp´e, A. K.; Skiff, W. M.; Casewit, C. J. *Chem. Rev.* **2000**, *100*, 1435.

[43] Sandhya, K. S.; Koga, N.; Nagaoka, M. *Bull. Chem. Soc. Jpn.* **2016**, *89*, 1093.

[44] Angermund, K.; Fink, G.; Jensen, V. R.; Kleinschmidt, R. *Chem. Rev.* **2000**, *100*, 1457.

[45] Zurek, E.; Ziegler, T. *Faraday Discuss.* **2003**, *124*, 93.

[46] Xu, Z.; Vanka, K.; Ziegler, T. *Organometallics* **2004**, *23*, 104.

[47] Ziegler, T.; Vanka, K.; Xu, Z. *C. R. Chim.* **2005**, *8*, 1552.

[48] Tomasi, S.; Razavi, A.; Ziegler, T. *Organometallics* **2007**, *26*, 2024.

[49] Lanza, G.; Fragalà, I. L.; Marks, T. J. *J. Am. Chem. Soc.* **2000**, *122*, 12764.

[50] Lanza, G.; Fragalà, I. L.; Marks, T. J. *Organometallics* **2002**, *21*, 5594.

[51] Motta, A.; Fragalà, I. L.; Marks, T. J. *J. Am. Chem. Soc.* **2007**, *129*, 7327.

[52] Motta, A.; Fragalà, I. L.; Marks, T. J. *J. Am. Chem. Soc.* **2008**, *130*, 16533.

[53] Correa, A.; Cavallo, L. *J. Am. Chem. Soc.* **2006**, *128*, 10952.

[54] Yang, S.; Ziegler, T. *Organometallics* **2006**, *25*, 887.

[55] Rowley, C. N.; Woo, T. K. *Organometallics* **2011**, *30*, 2071.

[56] Sian, L.; Macchioni, A.; Zuccaccia, C. *ACS Catal.* **2020**, *10*, 1591.

[57] Laine, A.; Coussens, B. B.; Hirvi, J. T.; Berthoud, A.; Friederichs, N.; Severn, J. R.; Linnolahti, M. *Organometallics* **2015**, *34*, 2415.

[58] Flisak, Z.; Ziegler, T. *Proc. Natl. Acad. Sci.* **2006**, *103*, 15338.

[59] Kumawat, J.; Gupta, V. K. *ACS Catal.* **2020**, *10*, 1704.

[60] Parveen, R.; Cundari, T. R.; Younker, J. M.; Rodriguez, G. *Organometallics* **2020**, *39*, 2068.

[61] Riddlestone, I. M.; Kraft, A.; Schaefer, J.; Krossing, I. *Angew. Chem. Int. Ed.* **2018**, *57*, 13982–14024.

[62] Hoff, R.; Mathers, R. *Handbook of Transition Metal Polymerization Catalysts*; Wiley, 2010.

[63] Zaccaria, F.; Cipullo, R.; Budzelaar, P. H. M.; Busico, V.; Ehm, C. *J. Polym. Sci. A* **2017**, *55*, 2807.

[64] Matsumoto, K.; Sandhya, K. S.; Takayanagi, M.; Koga, N.; Nagaoka, M. *Organometallics* **2016**, *35*, 4099.

[65] Matsumoto, K.; Takayanagi, M.; Sankaran, S. K.; Koga, N.; Nagaoka, M. *Organometallics* **2018**, *37*, 343.

[66] Shao, J.; Tanner, S. W.; Thompson, N.; Cheatham, T. E. *J. Chem. Theory Comput.* **2007**, *3*, 2312, PMID: 26636222.

[67] Frisch, M. J.; Trucks, G. W.; Schlegel, H. B.; Scuseria, G. E.; Robb, M. A.; Cheeseman, J. R.; Scalmani, G.; Barone, V.; Petersson, G. A.; Nakatsuji, H.; Li, X.; Caricato, M.; Marenich, A. V.; Bloino, J.; Janesko, B. G.; Gomperts, R.; Mennucci, B.; Hratchian, H. P.; Ortiz, J. V.; Izmaylov, A. F.; Sonnenberg, J. L.; Williams-Young, D.; Ding, F.; Lipparini, F.; Egidi, F.; Goings, J.; Peng, B.; Petrone, A.; Henderson, T.; Ranasinghe, D.; Zakrzewski, V. G.; Gao, J.; Rega, N.; Zheng, G.; Liang, W.; Hada, M.; Ehara, M.; Toyota, K.; Fukuda, R.; Hasegawa, J.; Ishida, M.; Nakajima, T.; Honda, Y.; Kitao, O.; Nakai, H.; Vreven, T.; Throssell, K.; Montgomery, J. A., Jr.; Peralta, J. E.; Ogliaro, F.; Bearpark, M. J.; Heyd, J. J.; Brothers, E. N.; Kudin, K. N.; Staroverov, V. N.; Keith, T. A.; Kobayashi, R.; Normand, J.; Raghavachari, K.; Rendell, A. P.; Burant, J. C.; Iyengar, S. S.; Tomasi, J.; Cossi, M.; Millam, J. M.; Klene, M.; Adamo, C.; Cammi, R.; Ochterski, J. W.; Martin, R. L.; Morokuma, K.; Farkas, O.; Foresman, J. B.; Fox, D. J. Gaussian16 Revision C.01. 2016; Gaussian Inc. Wallingford CT.

[68] Zhao, Y.; Truhlar, D. G. *Theor. Chem. Acc.* **2008**, *120*, 215.

[69] Zhao, Y.; Truhlar, D. G. *J. Chem. Phys.* **2006**, *125*, 194101.

[70] Marenich, A. V.; Cramer, C. J.; Truhlar, D. G. *J. Phys. Chem. B* **2009**, *113*, 6378.

[71] Simon, S.; Duran, M.; Dannenberg, J. *J. Chem. Phys.* **1996**, *105*, 11024.

[72] Boys, S. F.; Bernardi, F. *Mol. Phys.* **1970**, *19*, 553.

[73] Sugita, Y.; Okamoto, Y. *Chem. Phys. Lett.* **1999**, *314*, 141.

[74] Case, D.; Babin, V.; Berryman, J.; Betz, R.; Cai, Q.; Cerutti, D.; T.E. Cheatham, I.; Darden, T.; Duke, R.; Gohlke, H.; Goetz, A.; Gusarov, S.; Homeyer, N.; Janowski, P.; Kaus, J.; Kolossv´ary, I.; Kovalenko, A.; Lee, T.; LeGrand, S.; Luchko, T.; Luo, R.; Madej, B.; Merz, K.; Paesani, F.; Roe, D.; Roitberg, A.; Sagui, C.; Salomon-Ferrer, R.; Seabra, G.; Simmerling, C.; Smith, W.; Swails, J.; Walker, R.; Wang, J.; Wolf, R.; Wu, X.; Kollman, P. *AMBER 14*; University of California: San Francisco, 2014.

[75] Besler, B. H.; Merz, K. M.; Kollman, P. A. *J. Comput. Chem.* **1990**, *11*, 431.

[76] Singh, U. C.; Kollman, P. A. *J. Comput. Chem.* **1984**, *5*, 129.

[77] Wang, J.; Wolf, R. M.; Caldwell, J. W.; Kollman, P. A.; Case, D. A. *J. Comput. Chem.* **2004**, *25*, 1157.

[78] Smoluchowski, M. v. *Zeitschrift für physikalische Chemie* **1918**, *92*, 129.

[79] Nagaoka, M.; Suzuki, Y.; Okamoto, T.; Takenaka, N. *Chem. Phys. Lett.* **2013**, *583*, 80.

[80] Suzuki, Y.; Nagaoka, M. *J. Chem. Phys.* **2017**, *146*, 204102.

[81] Matsumoto, K.; Takayanagi, M.; Suzuki, Y.; Koga, N.; Nagaoka, M. *J. Comput. Chem.* **2019**, *40*, 421.

[82] Joshi, A.; Zijlstra, H. S.; Collins, S.; McIndoe, J. S. *ACS Catalysis* **2020**, *10*, 7195.

Chapter 3

Atomistic Simulation of the Polymerization Reaction by a (Pyridylamido)hafnium(IV) Catalyst: Counteranion Influence on the Reaction Rate and the Living Character of the Catalytic System

3.1. Introduction

These days, the major focus in polymer chemistry has been placed on the concept of green chemistry and sustainable material development in an ideal way to reduce the negative impact of the industrial chemicals on human health and the environment [1]. In this aspect, better insights into microscopic reaction mechanisms of catalytic polymerization (CP) reactions are strongly needed for the sustainable development of new generations of polymerization catalysts.

Understanding the detailed mechanisms of CP reaction has been a great challenge due to its complexity and the difficulty of isolating reaction intermediates. In general, CP reaction mechanisms are experimentally investigated by various methods such as NMR spectroscopy, stopped-flow technique, quench-labeling, FT-IR, GPC, and so on [2–6]. Nevertheless, it is still difficult to observe the instantaneous and microscopic phenomenon of the reaction at each moment of the polymerization process.

In this aspect, computational chemistry methodologies have become powerful tools that are not only complementary to experimental approaches but also essential for investigating the microscopic chemical phenomena. In particular, mechanistic studies of CP reactions using quantum mechanical (QM) method [7] have been intensively conducted [8–19]. Some studies have utilized molecular dynamics (MD) method [20] to simulate the atomistic motion of catalysts [21–24]. Nevertheless, these conventional methods can deal with just either initial or partial reaction step out of the whole polymerization process and thus cannot adopt a catalyst with a growing polymer chain attached to its metal atom as a calculation model. However, for a comprehensive understanding of CP reactions, it is strongly expected that the whole CP process should be dealt with by alternative and advanced simulation methods.

For this purpose, the Red Moon (RM) methodology [25,26] should be a promising one, which can deal with the whole reaction process. It is demonstrated that RM simulations can reasonably reproduce the experimentally observable macroscopic physical quantities, assuming the appropriate reaction schemes based on the chemical kinetics framework [27–32]. In this method, diffusion and reaction processes could be reasonably described by MD and Monte Carlo (MC) methods, respectively. Thus, the RM methodology should become an effective and efficient method to reveal the mechanism of the whole CP process from a microscopic point of view.

Therefore, in this chapter, I would like to conduct RM simulations of the 1-octene polymerization reaction catalyzed by (pyridylamido)Hf(IV) complex [33–35], aiming for its future application to more complex chemical reaction, like chain-shuttling polymerization (CSP) catalyst system [35–37], where ethylene/1-octene block

copolymers are produced. I would like to focus on the most important properties that have been paid attention to, i.e., activities and the living characters of the catalytic systems, which determine the molecular weight distribution (MWD) of the polymers [38–45]. It is reported that the 1-octene polymerization by the (pyridylamido)Hf(IV) catalyst proceeds about twice faster with $B(C_6F_5)_4^-$ than with $MeB(C_6F_5)_3^-$ [42], which means that the activity of the catalyst is higher with $B(C_6F_5)_4^-$ than with $MeB(C_6F_5)_3^-$. Notably, not only the catalytic activity but also the living character of the catalytic system is dependent on the CAs; It is experimentally reported that polydispersity index (PDI) of 1-hexene polymer produced by the (pyridylamido)Hf(IV) catalyst with $B(C_6F_5)_4^-$ is relatively larger, that is, its MWD is broader than that produced with $MeB(C_6F_5)_3^-$ [38]. This implies that the catalytic system has a lesser living character in its polymerization reaction with $B(C_6F_5)_4^-$ than with $MeB(C_6F_5)_3^-$.

Thus, I perform full-atomistic simulation of olefin polymerization reaction by the (pyridylamido)Hf(IV) catalyst with $MeB(C_6F_5)_3^-$ and $B(C_6F_5)_4^-$ using RM method, and investigate the ion pair (IP) structures during the polymerization reaction, which should significantly affect the reaction rates. Then, I analyze the MD trajectories of RM simulation to estimate the chain termination reaction rate in the presence of each CA, which critically affects the MWD, in order to elucidate the origin of the living character of the polymerization reaction that is dependent on the coexisting CAs.

This chapter is organized as follows: In Section 3.2, the reaction scheme and elementary processes of the present catalytic system are described. In Section 3.3, the theoretical treatment of Red Moon method is described. In Section 3.4, computational

details are provided. Then, in Section 3.5, results and discussion are described. Finally, in the last section, the findings of this study are summarized.

3.2. Reaction Scheme and Its Elementary Processes

In general, the fundamental mechanism of a typical catalytic olefin polymerization includes (i) initiation, (ii) propagation, and (iii) termination reactions. Additionally, in the present CP reaction system, the catalyst needs to be activated before the polymerization reaction ((0) activation reaction). Then, the reaction scheme of the present CP reaction can be described in **Scheme 1** [31], where M stands for a monomer, P and D stand for growing and dead (or dormant) chains, respectively, and T stands for a termination agent. The reaction starts with the activation reaction of catalyst (Cat) to

$$\mathrm{Cat} \longrightarrow \mathrm{Cat}^{*} \qquad \text{(0) Activation} \qquad \text{(R1)}$$

$$\mathrm{Cat}^{*} + \mathrm{M} \longrightarrow \mathrm{P}_1 \qquad \text{(i) Initiation} \qquad \text{(R2)}$$

$$\mathrm{P}_n + \mathrm{M} \longrightarrow \mathrm{P}_{n+1} \qquad \text{(ii) Propagation} \qquad \text{(R3)}$$

$$\mathrm{P}_n + \mathrm{T} \longrightarrow \mathrm{D}_n + \mathrm{Cat}^{*}\text{–T} \qquad \text{(iii) Termination} \qquad \text{(R4)}$$

an active catalyst (Cat^{*}) (in (R1)) and chain initiation by creating a monomer-inserted species P_1 from Cat^{*} with M (in (R2)). Then, the chain propagates (in (R3)), where P_n stands for a growing chain attached to an active catalyst, possessing a total number

of *n* monomer units. In the last reaction (iii), a growing chain becomes a dead (or dormant) chain D_n with or without a termination agent T (in (R4)). In general, there are some possible mechanisms of termination reaction in the CP system, such as *β*-hydride transfer (T = M, Cat^*–T = P_1), *β*-hydride elimination (T = none, Cat^*–T = metal hydride complex), hydrogenolysis (T = H_2, Cat^*–T = metal hydride complex) reactions, and so on.

In the RM simulations of the present study, however, the last reaction (iii) is not explicitly considered because the present CP reaction is assumed to proceed in a living-like way, and (iii) itself is actually a very unlikely event. Besides, since some experimental studies employed a preactivation procedure to obtain the active catalyst before starting polymerization reaction [42,44], I would not consider (0) activation reaction explicitly but focus on (i) initiation and (ii) propagation reactions, in order to compare the simulation results with the experimental ones. Therefore, for the RM simulation of the present CP system, I introduce the elementary processes of the two steps (i) and (ii) in the reaction scheme.

3.2.1. Catalyst Activation Reaction with Two Elementary Processes

In **Figure 1**, shown is the schematic representation of 1-octene polymerization by (pyridylamido)Hf(IV). It should be noted that, before the initiation reaction (i) and the propagation reaction (ii) with subsequent monomer insertion, the activation reaction (0) occurs, involving the two elementary processes, i.e., (0-i) catalytic IP

formation from precatalyst 1 via methide abstraction by a cocatalyst and (0-ii) monomer insertion processes.

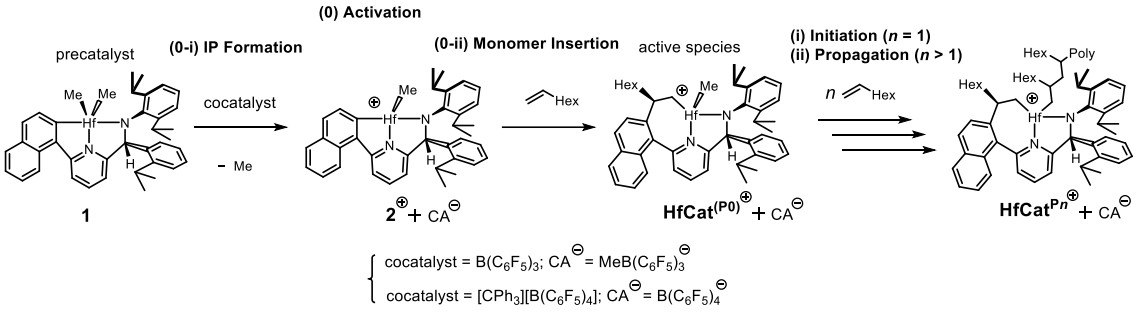

Figure 1. Schematic representation of 1-octene polymerization reaction by (pyridylamido)Hf(IV) catalyst: (0) Instantaneous activation consisting of (0-i) IP formation and (0-ii) monomeric 1-octene insertion, (i) initiation and (ii) propagation reactions. The 1-octene-inserted active species ($HfCat^{+}$) shows initiation reaction (i) to form $HfCat^{P1+}$ with *mono*meric 1-octene and further propagation reaction (ii) to form $HfCat^{Pn+}$ with *n*-meric 1-octene polymer chain. "Poly" represents a polymer chain, while "Hex" is a hexyl group.

The former process (0-i) is the formation process of an IP of cation 2^{+} and CA out of (pyridylamido)Hf(IV) complex 1 and a cocatalyst. Among the cocatalysts to activate the precatalyst, boron-based cocatalysts $B(C_6F_5)_3$, and $[C(C_6H_5)_3][B(C_6F_5)_4]$ are the most widely used [38,39,42,46]. The activation of the precatalyst 1 by $B(C_6F_5)_3$ yields the cationic catalyst 2^{+} and $MeB(C_6F_5)_3^{-}$ as CA, while that by $[C(C_6H_5)_3][B(C_6F_5)_4]$ yields 2^{+} and $B(C_6F_5)_4^{-}$ with the neutral byproduct $MeC(C_6H_5)_3$.

The latter process (0-ii) is a process of a monomeric 1-octene insertion into the Hf–naphthyl bond of 2^{+}, which forms the catalytically active species called "monomer-inserted active species", i.e., "1-octene-inserted active species" $HfCat^{+}$ (**Figure 1**)

[47,48]. Although there are some possible isomeric 1-octene-inserted active species, $HfCat^{+}$ in **Figure 1**, where the hexyl chain in the *β*-position is oriented back toward the pyridine ring of the ligand, is suggested to be kinetically favored in the experiment [48].

Thus, in **Scheme 1**, Cat corresponds to a pair of **1** and either $B(C_6F_5)_3$ or $[C(C_6H_5)_3][B(C_6F_5)_4]$, while Cat* does to an IP of $HfCat^{+}$ and either $MeB(C_6F_5)_3^{-}$ or $B(C_6F_5)_4^{-}$.

3.2.2. Initiation and Propagation Reactions

In general, the monomer insertion process in the CP reaction, common to both (i) initiation and (ii) propagation reactions (**Figure 1**), consists of the following steps: First, a monomer coordinates to the active site of the catalyst to form a suitable configuration for insertion process. Then, two chemical bonds are created between the polymeryl carbon atom on Hf and a sp^2 carbon atom of the monomer and between Hf and the other sp^2 carbon, leading to the chain elongation by one monomeric unit. In this way, the present polymerization reaction proceeds with a successive monomeric 1-octene insertion to the Hf–alkyl bond of $HfCat^{+}$ to form $HfCat^{Pn+}$, where the superscript P*n* denotes an *n*-meric 1-octene polymer chain attached to the Hf atom ($n \geq 0$), assuming hereafter that $HfCat^{P0+}$ denotes $HfCat^{+}$ itself (**Figure 1**). Thus, in **Scheme 1**, P_n stands, as a whole, for an IP of $HfCat^{Pn+}$ and CA, in general.

Concerning the possible configuration for the monomer insertion reaction, two types of coordination sites can be assumed in $HfCat^{Pn+}$, which are defined as *trans* and

cis to distinguish them relative to the pyridine nitrogen atom of HfCat^{Pn+} [18,19] (**Figure 2(a)**). In addition, it is necessary to consider the orientation of 1-octene coordination, i.e., 1,2-insertion and 2,1-insertion (**Figure 2(b)**), which is expected to influence the molecular weight distribution of the polymer [42]. Thus, there are four possible coordination patterns of 1-octene insertion, i.e., *trans*-1,2, *cis*-1,2 *trans*-2,1 and *cis*-2,1 [49].

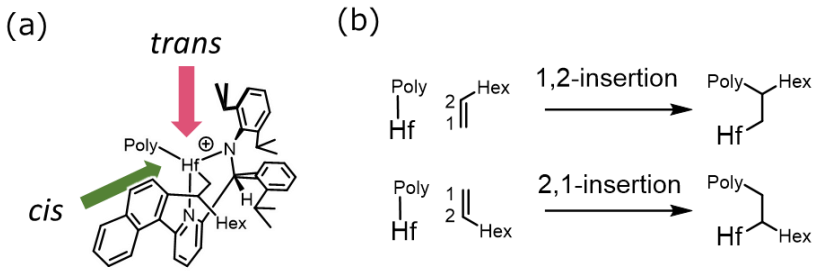

Figure 2. Schematic representations of (a) *trans*/*cis* and (b)1,2-/2,1-insertion to HfCat^{Pn+}. "Poly" represents a polymer chain, while "Hex" is a hexyl group.

3.3. Theoretical Treatments

To investigate the microscopic polymerization process in the present catalytic system, I employed the RM methodology [25,26], which is implemented by alternately using the molecular dynamics (MD) and the Monte Carlo (MC) methods. The former describes the dynamics of molecules in a long-time scale, while the latter describes the reactions that accompany the bond breaking and formation in a short-time scale.

Such one cycle consisting of the above process, including MC and MD process, is called an "RM cycle". By repeating this RM cycle, we can stochastically simulate a

succession of the chemical reaction, and we can realize reasonably the atomistic dynamics of the whole system [27–31]. Thus, the RM simulation would enable us to simulate the 1-octene polymerization reaction from $HfCat^{+}$ to $HfCat^{Pn+}$ ($n \geq 1$) as shown in **Figure 1**. The detailed algorithm of RM simulation is provided in Appendix A.

Additionally, before executing the simulations, for all the molecular species necessary for the present purpose in the reaction scheme (**Scheme 1**), atomic parameters in the molecular mechanical (MM) force field, such as the force constants, Lennard-Jones (LJ) parameters, and atomic charges, are required to be prepared (see Section 3.4).

3.4. Computational Details

3.4.1. (Pyridylamido)Hf Complex, Counteranion, 1-Octene, and Toluene Solvent

I prepared two CP systems for the RM simulation, each of which contains an IP of $HfCat^{+}$ with either $MeB(C_6F_5)_3^{-}$ or $B(C_6F_5)_4^{-}$ as a counteranion, 120 1-octene monomer molecules, and 480 toluene solvent molecules, hereafter denoted as $HfCat^{Pn+}$–$MeB(C_6F_5)_3^{-}$ or $HfCat^{Pn+}$–$B(C_6F_5)_4^{-}$ IP systems.

As the molecular mechanical (MM) force field parameters, the general AMBER force field (GAFF) 1.7 [50] was used for both 1-octene and toluene. Meanwhile, for the CAs and $HfCat^{Pn+}$, those parameters developed in our previous study [24] were

employed. The atomic point charges in the MM force field were assigned by the Merz-Singh-Kollman method [51,52].

In addition, to correctly represent the intermolecular interactions of cation–anion and cation–monomer, the Lennard-Jones (LJ) interaction parameters are introduced between the Hf atom and borate anion atoms and between the Hf atom and the olefinic carbon atoms in 1-octene, which have been developed in our previous studies [24,49].

3.4.2. Reaction Conditions and Control Parameters for RM Simulation

All MD calculations were performed by pmemd program in AMBER14 [53] under the periodic boundary condition. The box sizes of the $HfCat^{Pn+}$–$MeB(C_6F_5)_3^-$ and $HfCat^{Pn+}$–$B(C_6F_5)_4^-$ IP systems were both 50.5^3 $Å^3$. The concentrations of 1-octene monomers were 1.55 mol/L in both IP systems, about three times denser than the experimental conditions of 0.5 mol/L [42]. This is because when the concentration is set equal to the experimental one, I found it much more time-consuming to computationally reproduce the selectivity of the four reaction patterns in Section 2.2, which can be estimated from the QM study on 1-octene insertion reaction in Chapter 2 [49]. A weak coupling-algorithm with a constant of 1 ps was applied to control the temperature and the pressure, and SHAKE algorithm was used to constrain the bond distance including hydrogen atoms.

The initial CP systems were prepared according to the following procedure: First, all the molecules were allocated in the simulation box. They were then equilibrated by

one NPT-MD calculation performed for 100 ps at 323 K under the pressure of 500 bar. Then, NPT-MD calculations were performed for 500 ps at 323 K under 1 bar. Finally, NVT-MD calculations were performed for 1 ns at 323 K to obtain ten initial structures from the trajectories of the last 200 ps for each of the $HfCat^{Pn+}$–$MeB(C_6F_5)_3^-$ and $HfCat^{Pn+}$–$B(C_6F_5)_4^-$ IP systems.

The RM simulation was performed in NVT ensemble at 323 K. The NVT-MD calculation (process 2(a) in Appendix A) was performed for 100 ps with the time step of 2 fs. From the trajectories, configurations were sampled every 2 ps, and thus, in total, 50 configurations were obtained. The numerical value of $\Delta E_a^{R_i}$ for each 1-octene insertion process (R_i) was taken from the QM calculation in our previous research [49]. Under this calculation condition, ten RM simulations were performed for 3000 RM cycles, starting from the ten different initial structures, for each $HfCat^{Pn+}$–$MeB(C_6F_5)_3^-$ and $HfCat^{Pn+}$–$B(C_6F_5)_4^-$ IP system.

3.4.3. QM Model Preparation

To examine the activation free energies of possible termination reactions, which affect the MWDs, a model system consisting of an ethylene monomer and $HfCat^{P2+}$, which is made through 2,1-insertion of 1-octene monomer after the first 1,2-insertion, was prepared. Using this model, the following six-step procedure was conducted: (i) MD simulations were performed to sample a wide range of structures for the QM computational model of the insertion reaction. (ii) Then, 1000 structures were taken from the MD trajectory and classified them into 20 representative configurations by using the K-means clustering algorithm. (iii) By performing QM calculations for these

20 structures, the most stable five structures were selected. (v) Using these five structures as initial structures, the transition state structures of the β-hydride elimination reaction are searched for by using QM calculation. (vi) The most stable transition state (TS) structure was determined for each of the four insertion patterns, and from this structure, the reactant state (RS) and product state (PS) structures were obtained by IRC calculations, followed by structural optimizations.

To sample the initial structures for the QM calculations, I performed NVT-MD simulations in a vacuum for 1 ns at 800 K controlled by the weak-coupling algorithm with a time constant of 1 ps using AMBER14 [53]. In each calculation, I imposed harmonic constraints on the position of the 1-octene monomer to efficiently sample the desired configurations. I sampled configurations every 1 ps from each trajectory and obtained 1000 configurations for each monomer coordination pattern.

3.4.4. QM Calculation Details

All QM calculations were performed with the Gaussian16 package [54]. Geometrical optimizations were conducted under vacuum using the M06 functional [55,56]. The LANL2DZ basis set with the associated effective core potential and additional f orbitals was used for the Hf atom, and the standard 6-31G(d) basis set was used for the other atoms. Frequency analyses were carried out to confirm that each structure is a local minimum (no imaginary frequency) or a transition state (only one imaginary frequency). IRC calculations of the obtained transition states were performed to confirm the connectivity of the transition states to the intermediates. The energies of the optimized structures are further estimated through single-point

calculations in the toluene solvent with SMD model [57], using the M06 functional and the def2-TZVPP basis set for all the atoms. The Gibbs free energy of each optimized structure was calculated including thermal corrections.

3.5. Results and Discussion

3.5.1. Difference in the Initial Stage of Polymerization Reaction: Slow Initiation with $MeB(C_6F_5)_3^-$ vs. Fast Initiation with $HfCat^{Pn+}–B(C_6F_5)_4^-$

3.5.1.1. 1-Octene Consumption Rates Reproduced the Experimental Tendency: Faster with $B(C_6F_5)_4^-$ than with $MeB(C_6F_5)_3^-$

Figure 3 shows the average 1-octene consumption rate progress during the polymerization simulations of the $HfCat^{Pn+}–MeB(C_6F_5)_3^-$ and $HfCat^{Pn+}–B(C_6F_5)_4^-$ IP systems until 3000 RM cycle. **Table 1** shows the polymerization reaction rate constant k_2^{exp} in each IP system that can be estimated from the experiment [42,49]. In **Figure 3**, the polymerization reaction in the $HfCat^{Pn+}–B(C_6F_5)_4^-$ IP system proceeds about twice faster than that of the $HfCat^{Pn+}–MeB(C_6F_5)_3^-$ system throughout the simulation, which is consistent with the experimental result that is shown in **Table 1** [42]. The RM simulations of 1-octene polymerization reaction for 3000 RM cycles resulted in the average of ~33-mer (n = 33) and ~63-mer (n = 63) production by the $HfCat^{Pn+}–MeB(C_6F_5)_3^-$ and $HfCat^{Pn+}–B(C_6F_5)_4^-$ IPs, respectively. I found that the difference in the 1-octene consumption rate with respect to RM cycle comes from the difference in the total number of reaction candidates found during the NVT-MD process of RM simulation (process 2(a) in Appendix A), since the average ratio of all accepted reactions to all reaction candidates per one RM simulation was almost the same

between the $HfCat^{Pn+}$–$MeB(C_6F_5)_3^-$ and $HfCat^{Pn+}$–$B(C_6F_5)_4^-$ IP systems (0.070 and 0.069, see **Table B1** in Appendix B). The average of the total number of all reaction candidates per one RM simulation in the $HfCat^{Pn+}$–$B(C_6F_5)_4^-$ IP system was double that in the $HfCat^{Pn+}$–$MeB(C_6F_5)_3^-$ one (see **Table B1** in Appendix B). This result reflects the observation in the replica-exchange MD (REMD) simulations that the frequency of 1-octene coordination to $HfCat^+$ with $B(C_6F_5)_4^-$ as a counteranion was ~2.5 times larger than that with $MeB(C_6F_5)_3^-$ due to the dynamic effect of the CAs in Chapter 2 [49]. Therefore, the reaction "rate" with respect to RM cycle (**Figure 3**) is dependent on the monomer capture step, where a monomer coordinates to the catalyst. In fact, the finding in Chapter 2 showed that the "rate" difference in the polymerization reaction between with $MeB(C_6F_5)_3^-$ and with $B(C_6F_5)_4^-$ can be mainly attributed to the monomer capture step [49], therefore, RM cycle could be considered as the physical time. In our theoretical estimation based on the transformation theory [26], 1 RM cycle was evaluated, on average, to be ca. 20–25 μs of the physical time (see **Table C1** in Appendix C), by assuming k_2^{exp} values in **Table 1** as the propagation rates in the RM simulations ((R2) and (R3) in **Scheme 1**).

Taking a closer look at **Figure 3**, the large difference in the 1-octene consumption rate can be found in the initial stage of the polymerization reaction (until ~500 RM cycle) between the $HfCat^{Pn+}$–$MeB(C_6F_5)_3^-$ and $HfCat^{Pn+}$–$B(C_6F_5)_4^-$ IP systems. In the case of $HfCat^{Pn+}$–$MeB(C_6F_5)_3^-$ IP system, the 1-octene consumption rate grows comparatively more slowly, since no 1-octene propagation takes place in seven RM simulations out of the total of ten RM simulations before the 500 RM cycle. It is worth noting that, in one RM simulation out of the total of ten RM simulations of the $HfCat^{Pn+}$–$MeB(C_6F_5)_3^-$ IP system, no insertion reaction was observed throughout the

simulation for 3000 RM cycles. I suppose that this phenomenon might have some key to the relatively slow rise of the 1-octene consumption rate observed with $MeB(C_6F_5)_3^-$ experimentally in the initial stage of the 1-octene polymerization reaction, even when the catalyst is pre-activated [42]. On the other hand, as for the $HfCat^{Pn+}$–$B(C_6F_5)_4^-$ system, the reaction rate at the beginning of the polymerization reaction looks slightly higher than that afterward. This phenomenon should have some relationships with the bulkiness of the growing polymer chain around the active site of the catalyst.

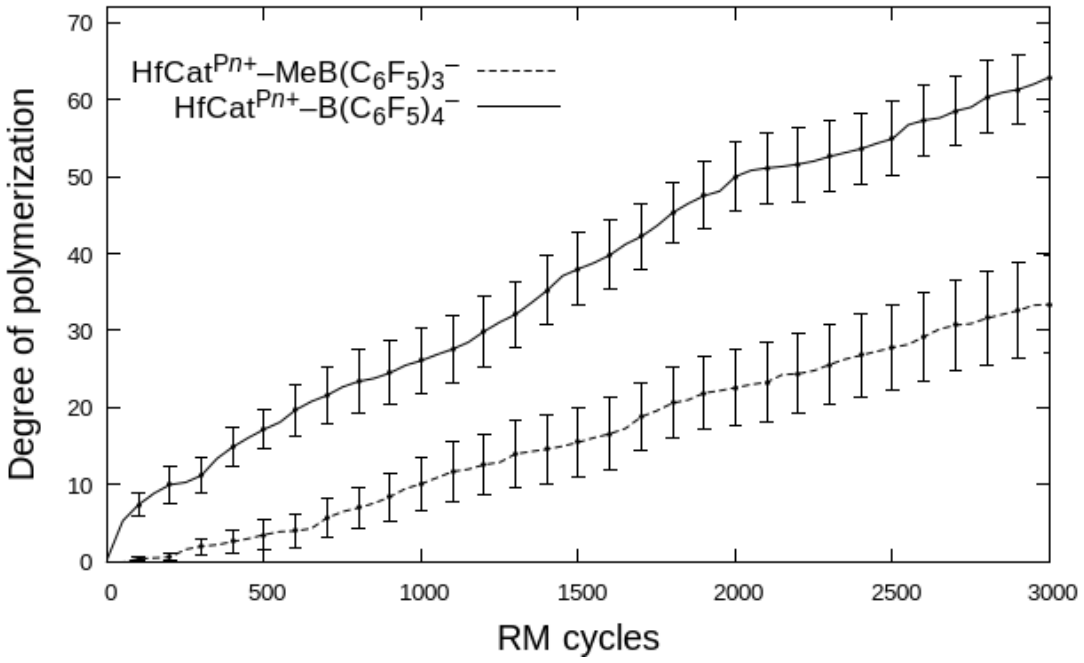

Figure 3. Averaged degree of polymerization vs. RM cycle for each $HfCat^{Pn+}$–$MeB(C_6F_5)_3^-$ and $HfCat^{Pn+}$–$B(C_6F_5)_4^-$ IP system until 3000 RM cycles. The average degree of polymerization was calculated by counting the average number of 1-octene molecules that are incorporated into $HfCat^{Pn+}$ out of the 10 RM samples at the end of each RM cycle in each IP system. The error bars correspond to the standard errors of the average degrees of polymerization of the 10 RM samples at each moment of every 100 RM cycles.

Table 1. Experimental 1-octene polymerization reaction rate constants k_2^{exp} in $HfCat^{Pn+}$–$MeB(C_6F_5)_3^-$ and $HfCat^{Pn+}$–$B(C_6F_5)_4^-$ IP systems.

IP system	k_2^{exp} ($L \cdot mol^{-1} \cdot s^{-1}$)
$HfCat^{Pn+}$–$MeB(C_6F_5)_3^-$	3.5×10^2
$HfCat^{Pn+}$–$B(C_6F_5)_4^-$	5.6×10^2

3.5.1.2. Monomer Distribution Influenced by the Growing Polymer Chains: Difficulty of the First Monomer Insertion with $MeB(C_6F_5)_3^-$

Since the polymerization reaction rate in RM simulation is controlled by the frequency of monomer coordination to the catalyst, monomer distributions around the active site would help us understand the difference of the 1-octene consumption rates in **Figure 3**. **Figure 4** shows the radial distribution functions $g(r)$ between the sp^2 carbon atoms of 1-octene monomer and Hf atom of either $HfCat^{Pn+}$–$MeB(C_6F_5)_3^-$ or $HfCat^{Pn+}$–$B(C_6F_5)_4^-$ having an *n*-mer chain on Hf, where *n* is set to 0, 1, 6, 12, 24, or 36 (see Appendix D). **Table 2** shows the equilibrium constant K_d(in) for the pre-equilibrium state of monomer insertion reaction (see Section V in **Supporting Information**) estimated from the MD trajectory in each IP system, which is an index of the frequency of monomer coordination to $HFCat^{Pn+}$. In **Figure 4**, the two remarkable peaks of $g(r)$ around 3–4 Å correspond to the two carbon atoms coordinating to the Hf center. It is remarkable that, in the initial $HfCat^{P0+}$–$MeB(C_6F_5)_3^-$

IP system, i.e., the system with 0-mer, 1-octene monomers cannot coordinate to HfCat^{P0+}, for there are no peaks observed around 3–4 Å (**Figure 4(a)**). However, in the HfCat^{P1+}–MeB$(C_6F_5)_3^-$ IP system with 1-mer, the 1-octene coordination to HfCat^{P1+} around r = 3–4 Å can be observed (**Figure 4(a)**). Accordingly, the K_d(in) value increases drastically from n = 0 to n = 1 in the HfCat^{P0+}–MeB$(C_6F_5)_3^-$ IP system (**Table 2**). It is suggested, therefore, that the MeB$(C_6F_5)_3^-$ coordinates to HfCat$^+$ so strongly that first monomer insertion, i.e., the initiation reaction ((R2) in **Scheme 1**), hardly occurs. Then, after the first insertion, the HfCat^{Pn+}–MeB$(C_6F_5)_3^-$ interaction would become weakened by the steric hindrance of the inserted 1-octene monomers on the Hf atom, so that a successive monomer insertion can take place more easily.

Table 2. Equilibrium constant K_d(in) (L·mol^{-1}) for the pre-equilibrium of monomer insertion reaction in the HfCat^{Pn+}–MeB$(C_6F_5)_3^-$ and HfCat^{Pn+}–B$(C_6F_5)_4^-$ IP systems, where n is set to 0, 1, 6, 12, 24, or 36.

IP system	n = 0	n = 1	n = 6	n = 12	n = 24	n = 36
HfCat^{Pn+}–MeB$(C_6F_5)_3^-$	9.4×10^{-4}	1.9×10^{-1}	3.6×10^{-3}	1.1×10^{-3}	2.4×10^{-3}	4.0×10^{-3}
HfCat^{Pn+}–B$(C_6F_5)_4^-$	1.7×10^{0}	1.4×10^{-1}	7.5×10^{-3}	5.2×10^{-3}	2.9×10^{-3}	5.7×10^{-3}

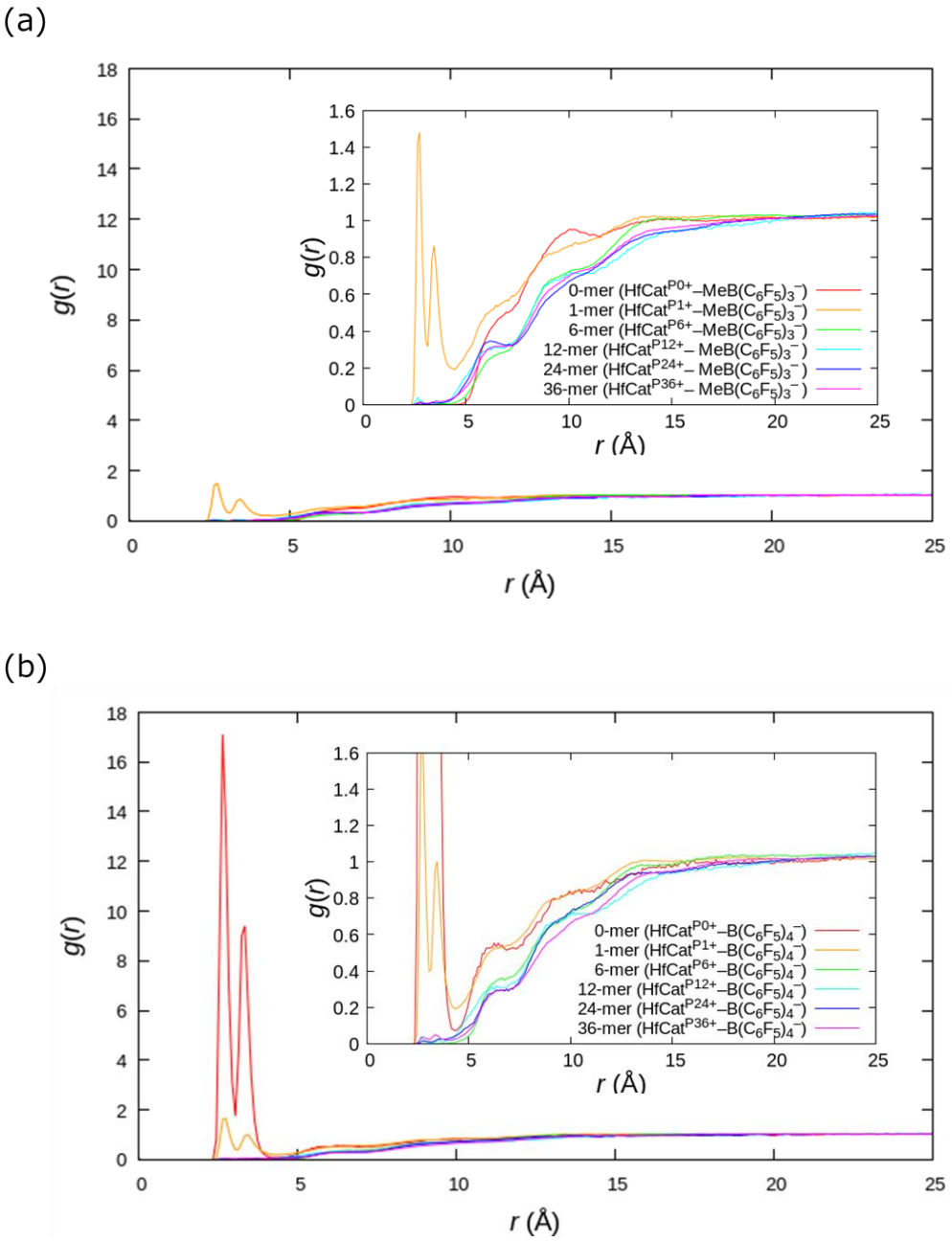

Figure 4. Radial distribution functions between the sp^2 carbon atoms of 1-octene monomers and the Hf atom of $HfCat^{Pn+}$ (a) in the $HfCat^{Pn+}$–$MeB(C_6F_5)_3^-$ IP system and (b) in the $HfCat^{Pn+}$–$B(C_6F_5)_4^-$ IP system, obtained from 200-ns-long NVT-MD simulations. Here, "*n*-mer" represents *n*-meric 1-octene polymers produced through RM simulations. The initial structures were selected from RM simulation at random**.**

Contrary to the HfCat^{Pn+}–MeB$(C_6F_5)_3^-$ IP system, in the HfCat^{Pn+}–B$(C_6F_5)_4^-$ one, the monomer coordination peaks of $g(r)$ around r = 3–4 Å, is higher with 0-mer than with 1-mer. This suggests that B$(C_6F_5)_4^-$ does not hinder monomer coordination to the Hf center, unlike MeB$(C_6F_5)_3^-$, since B$(C_6F_5)_4^-$ has weaker coordination ability than MeB$(C_6F_5)_3^-$, which can be also confirmed from the larger K_d(in) value when n = 0, in comparison to that when n = 1 in **Table 2**. Therefore, the initiation reaction ((R2) in **Scheme 1**) proceeds very rapidly in the HfCat^{Pn+}–B$(C_6F_5)_4^-$ IP system. It is confirmed that the $g(r)$ around r = 3–4 Å decreases as the polymer chain grows from 0-mer to 6-mer in both IP systems. It is interesting, however, that there is no significant difference in $g(r)$ after the polymer chain becomes larger than 6-mer (n > 6) in both HfCat^{Pn+}–MeB$(C_6F_5)_3^-$ and HfCat^{Pn+}–B$(C_6F_5)_4^-$ IP systems. Although the K_d(in) values fluctuate from n = 6 to n = 36 due to the limited time length of the MD simulation, they are within the same range of values, i.e., from 10^{-3} to 10^{-2} (**Table 2**). This implies that, as polymerization proceeds, the bulkiness of the growing polymeryl chain does not make a significant difference in the monomer distribution around the HfCat^{Pn+} active site. Therefore, in the HfCat^{Pn+}–B$(C_6F_5)_4^-$ IP system, the 1-octene consumption rate becomes slower but roughly constant after several monomer insertion reactions take place.

3.5.2. Different IP Structures with $MeB(C_6F_5)_3^-$ vs. $B(C_6F_5)_4^-$ Largely Influence the Monomer Coordination to the Active Site

3.5.2.1. Five Characteristic Regions on Free Energy Surfaces to Distinguish between ISIPs and OSIPs

I have demonstrated in Subsection 3.5.1 that 1-octene monomer distribution around the active site of $HfCat^{Pn+}$ changes as the polymerization proceeds due to the steric hindrance of the growing polymer. Further, during the successive polymerization process, it can be reasonably expected that the dynamics of CA should also be influenced by the polymeryl chain growing on $HfCat^{Pn+}$. It is assumed that the IP structure critically affects the frequency of monomer coordination to the active site, which thus significantly differentiates the polymerization reaction rates. Thus, I analyzed the IP structures of the $HfCat^{Pn+}$–$MeB(C_6F_5)_3^-$ and $HfCat^{Pn+}$–$B(C_6F_5)_4^-$ complexes during the RM simulations.

For drawing the characteristic free energy surfaces (FESs) using the obtained trajectories, in the present study, the interatomic distance r between Hf and B atoms and the angle ϕ formed between the straight lines connecting Hf to B and N in pyridine ring (**Figure 5**) were taken as the two coordinates to map the FESs (see Appendix E). To distinguish the anion location relative to the $HfCat^{Pn+}$ on the 2-dimensional free energy (FE) maps, it is convenient to divide the FE maps into the five characteristic regions; i) Region A' satisfying 4 Å < r < 5 Å and 100° < ϕ < 160°, ii) Region A satisfying 4 Å < r < 5 Å and 40° < ϕ < 100°, iii) Region B satisfying 5 Å < r < 7 Å and

30° < ϕ < 100°, iv) Region C satisfying 7 Å < r < 11 Å and 0° < ϕ < 40°, and v) Region D satisfying 7 Å < r < 11 Å and 40° < ϕ < 100°. Each of these five regions roughly corresponds to each characteristic IP structure; regions A and A' correspond to "inner-sphere" ion pair (ISIP) structures with Me group coordinating to the Hf center, region B corresponds to ISIP structures with F atom coordinating to Hf center, and regions C and D correspond to "outer-sphere" ion pair (OSIP) structures where CAs are located at the same side and the opposite of the active site across the pyridine ring of the $HfCat^{Pn+}$, respectively.

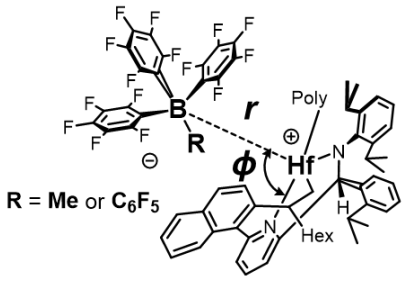

Figure 5. Definition of the distance r and the angle ϕ.

3.5.2.2. ISIPs Mainly Observed Initially While OSIPs Increased as Polymerization Proceeds in the $HfCat^{Pn+}$–$MeB(C_6F_5)_3^-$ IP System

Figure 6 shows the FE maps of the $HfCat^{Pn+}$–$MeB(C_6F_5)_3^-$ IP system during the RM simulation from 1 to 500 RM cycle (**Figure 6(a)**) and from 501 to 3000 RM cycle

(**Figure 6(b)**). Besides, the typical five catalyst structures **a'**$_{3PFB}$, **a**$_{3PFB}$, **b**$_{3PFB}$, **c**$_{3PFB}$, and **d**$_{3PFB}$ are shown in **Figure 7**, where the subscript 3PFB denotes $MeB(C_6F_5)_3^-$ (methyl**tris**(**p**er**f**luorophenyl)**b**orate), which are typically found in the five regions A', A, B, C, and D defined in **Figure 6(a)** and **6(b)**, respectively. From 1 to 500 RM cycle (**Figure 6(a)**), region A' is more stable than A, since the structure **a'**$_{3PFB}$ (**Figure 7**), mainly observed in region A', is the initial structure of the IP ((R2) in **Scheme 1**), while the structure **a**$_{3PFB}$ observed in region A corresponds to the catalyst structure of IP complex with a growing polymeryl group on the Hf atom (**Figure 7**). Due to the steric hindrance of the polymer, the angle ϕ in structure **a**$_{3PFB}$ is lower than that in **a'**$_{3PFB}$ to avoid the steric repulsion. Although I also observed the F atom coordinated ISIP structure **b**$_{3PFB}$ and OSIP structures **c**$_{3PFB}$ and **d**$_{3PFB}$ respectively in regions B, C, and D (**Figure 6(a)**), mainly observed is **a'**$_{3PFB}$, and the FE minimum is within region A'.

It can be seen from **Figure 6(a)** and **6(b)** that the relative FEs in the regions A, B, C, and D become lower as the polymerization reaction proceeds. From 501 to 3000 RM cycle, the FE minimum is still within region A', since the first insertion took place after 500 RM cycle in most of RM simulations (**Figure 6(b)**). It is reasonable that region A becomes more stable after the 500 RM cycle than before 500 RM cycle, due to the bulkiness of growing polymer chains. In the FE map from 501 to 3000 RM cycle (**Figure 6(b)**), two FE minima in regions C and D, which correspond to the OSIP structures **c**$_{3PFB}$ and **d**$_{3PFB}$, respectively, were both ~0.9 kcal/mol. Compared with the FE map from 1 to 500 RM cycle (**Figure 6(a)**), where two FE minima in regions C and D were both ~1.8 kcal/mol, we can see that the relative stability of the OSIP structure is enhanced by the steric effect of the polymeryl chain. Actually, 98% of the monomer insertion reaction candidates were observed in regions C and D throughout the RM

simulations. On the other hand, it is worth noting that even in the IP systems with a bulky 36-mer on the Hf active center, the IP state distributions were still observed in regions A and B, i.e., *r* ~4 Å and ~5 Å, which correspond to two ISIPs $\mathbf{a}_{\mathbf{3PFB}}$ and $\mathbf{b}_{\mathbf{3PFB}}$, respectively. Thus, it is confirmed that the $MeB(C_6F_5)_3^-$ anion can coordinate to $HfCat^{Pn+}$ with the Me group even after the polymeryl group on the Hf atom becomes comparatively bulky.

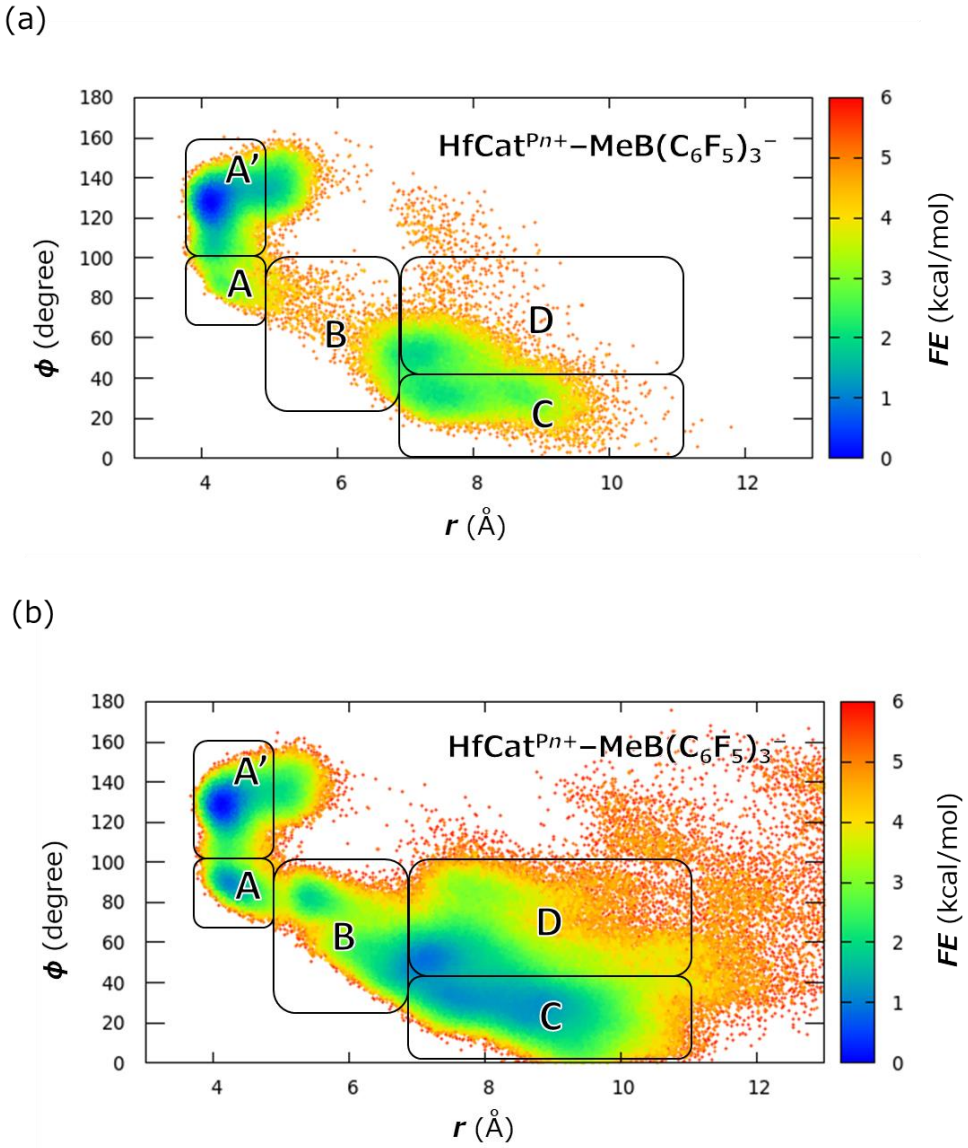

Figure 6. Free energy maps with respect to r and ϕ for the HfCat^{Pn+}–MeB$(C_6F_5)_3^-$ complex in RM cycles; (a) from 1 to 500 RM cycles and (b) from 501 to 3000 RM cycles. The free energy at the most stable point in region A' is set to the origin (0.00 kcal/mol). Calculations were performed by using bins with size of (0.05 Å, 2.0 deg.)

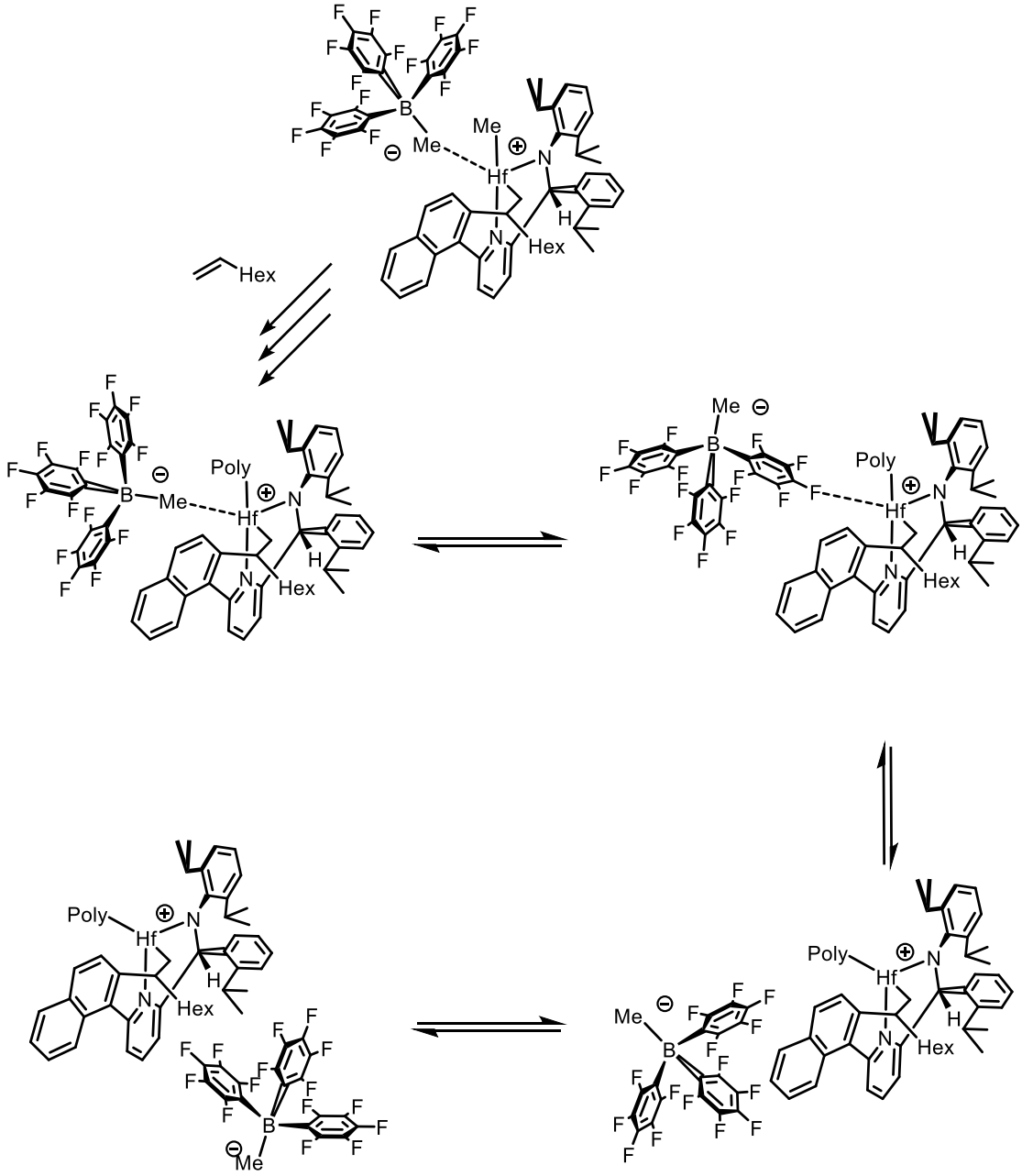

Figure 7. Schematic images of the structure transition of the $HfCat^{Pn+}$–$MeB(C_6F_5)_3^-$ IPs in the 1-octene polymerization process. The structures **a'$_{3PFB}$**, **a$_{3PFB}$**, **b$_{3PFB}$**, **c$_{3PFB}$** and **d$_{3PFB}$** are the representative structures of regions A', A, B, C and D in Figure 6(a) and 6(b), respectively.

3.5.2.3. OSIPs Mostly Observed in the HfCat^{Pn+}–B(C$_6$F$_5$)$_4^-$ IP System throughout the Polymerization Process

Figure 8 shows the FE maps of the HfCat^{Pn+}–B(C$_6$F$_5$)$_4^-$ IP during the RM simulation from 1 to 500 cycle (**Figure 8a**) and from 501 to 3000 cycle (**Figure 8b**). Besides this, the typical two catalyst structures **c**$_{4PFB}$ and **d**$_{4PFB}$ are shown in **Figure 9**, where the subscript 4PFB denotes B(C$_6$F$_5$)$_4^-$ (**tetrakis**(**p**er**f**luorophenyl)**b**orate), which are typically found in the two regions C and D defined in **Figures 8(a)** and **8(b)**, respectively. In both FE maps from 1 to 500 RM cycle and from 501 to 3000 RM cycle, the states of the HfCat^{Pn+}–B(C$_6$F$_5$)$_4^-$ IP are distributed mainly in regions C and D, where OSIP structures **c$_{4PFB}$** and **d$_{4PFB}$** are mainly observed, respectively (**Figure 9**). However, ISIP structures are scarcely observed throughout the polymerization process, because of the weak cation–anion interaction energy of the HfCat^{Pn+}–B(C$_6$F$_5$)$_4^-$ IP system, which can be easily separated by the stronger interaction between HfCat^{Pn+} and monomers.

Although there is no remarkable difference in FE maps between 1–500 and 501–3000 RM cycle (**Figure 8**), the IP state distributions in region D and around r ~ 9.5 Å in region C, where the B(C$_6$F$_5$)$_4^-$ anion is located far from the active site, become a little more stable in the FE map from 501 to 3000 RM cycle (**Figure 8b**) than before 500 RM cycle (**Figure 8a**), probably due to the steric hindrance between B(C$_6$F$_5$)$_4^-$ and the bulkier polymeryl groups of HfCat^{Pn+}.

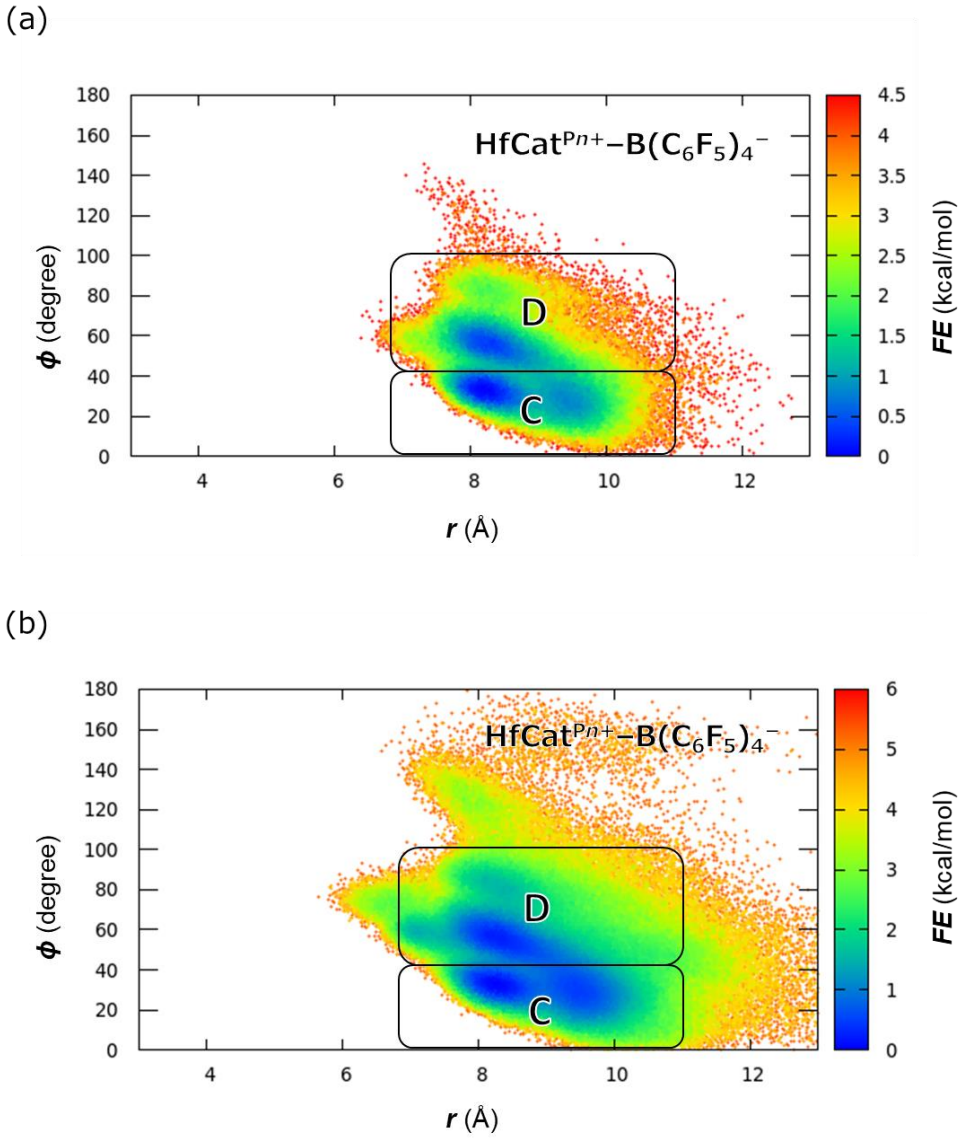

Figure 8. Free energy maps with respect to r and ϕ for the $HfCat^{Pn+}$–$B(C_6F_5)_4^-$ complex in RM cycles; (a) from 1 to 500 RM cycles and (b) from 501 to 3000 RM cycles. The free energy at the most stable point in region C is set to the origin (0.00 kcal/mol), respectively. Calculations were performed by using bins with size of (0.05 Å, 2.0 deg.).

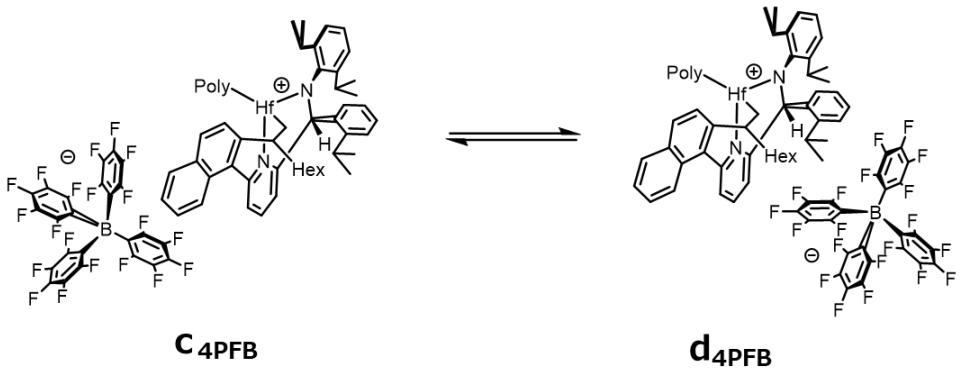

Figure 9. Schematic images of the structure transition of the $HfCat^{Pn+}$–$B(C_6F_5)_4^-$ IPs in the 1-octene polymerization process. The structures **c_{3PFB}** and **d_{4PFB}** are the representative structures of regions C and D in Figure 8, respectively

3.5.3. Chain Termination Reaction Possibly Influenced by IP Structures: Origin of Different Molecular Weight Distributions

3.5.3.1. Chain Termination Reaction from 2,1-Inserted Complex: *β*-Hydride Transfer More Reasonable than *β*-Hydride Elimination

I have demonstrated that the IP structures during the polymerization reaction are significantly different between in the $HfCat^{Pn+}$–$MeB(C_6F_5)_3^-$ IP and in $HfCat^{Pn+}$–$B(C_6F_5)_4^-$ IP. From those results, it is natural to suppose that the IP structure affects not only the polymerization reaction rate ((R2) and (R3) in **Scheme 1**) but also the chain termination reaction rate ((R4) in **Scheme 1**), which critically affects the molecular weight distribution of the olefin polymers. Hence, I propose a hypothesis that the MWD is broader for $HfCat^{Pn+}$–$B(C_6F_5)_4^-$ than $HfCat^{Pn+}$–$MeB(C_6F_5)_3^-$ IP system due to the difference in the chain termination reaction rates. To examine this hypothesis, I have analyzed the RM simulation results.

It was reported in an experimental study that chain termination reactions were detected only after 2,1-insertion, not after 1,2-insertion (**Figure 2(b)**) [42]. Thus, the different MWDs of the polymers produced by the $HfCat^+$–$MeB(C_6F_5)_3^-$ complex and the $HfCat^+$–$B(C_6F_5)_4^-$ one can be attributed to the probability of 2,1-insertion taking place, which would be eventually followed by a chain termination reaction. In this regard, however, QM studies on 1-octene insertion reaction showed that the activation

FE of 2,1-insertion was only 1.5 kcal/mol higher than that of 1,2-insertion in either $HfCat^{+}$–$MeB(C_6F_5)_3^{-}$ or $HfCat^{+}$–$B(C_6F_5)_4^{-}$ complex [49]. Therefore, under this circumstance, it is reasonable to assume that the competition between 1-octene monomer insertion and chain termination reactions after 2,1-insertion reaction should determine the living character of the catalytic system.

Figure 10 shows the schematic representation of two possible reaction schemes of the chain termination reaction ((R4) in **Scheme 1**) from a 2,1-inserted structure, (a) *β*-hydride elimination (**Figure 10(a)**) and (b) *β*-hydride transfer (**Figure 10(b)**) reactions, which have been generally thought of as the most likely causes of chain termination reaction in transition metal polymerization catalysts [58–61]. I performed QM calculations of these two possible chain termination reactions from a 2,1-inserted catalyst model structure without any CAs. I observed no transition state of (a) *β*-hydride elimination reaction and found that the dissociation of the hydride complex and the product olefin molecule takes more than 35 kcal/mol. In contrast, a transition state of (b) *β*-hydride transfer reaction was found with the activation FE of ~25 kcal/mol (see **Figure F1** in Appendix F). This is consistent with the commonly accepted fact that the *β*-hydride transfer reaction pathway is generally preferred over *β*-hydride elimination in noncrowded catalysts like nonmetallocene catalysts, where the space around the metal atom is not restricted [59,60]. Therefore, among the present two reaction schemes, the *β*-hydride transfer reaction should be more suitable as the reasonable scheme of chain termination reaction, which is comparable with 1-octene insertion as a competitive reaction.

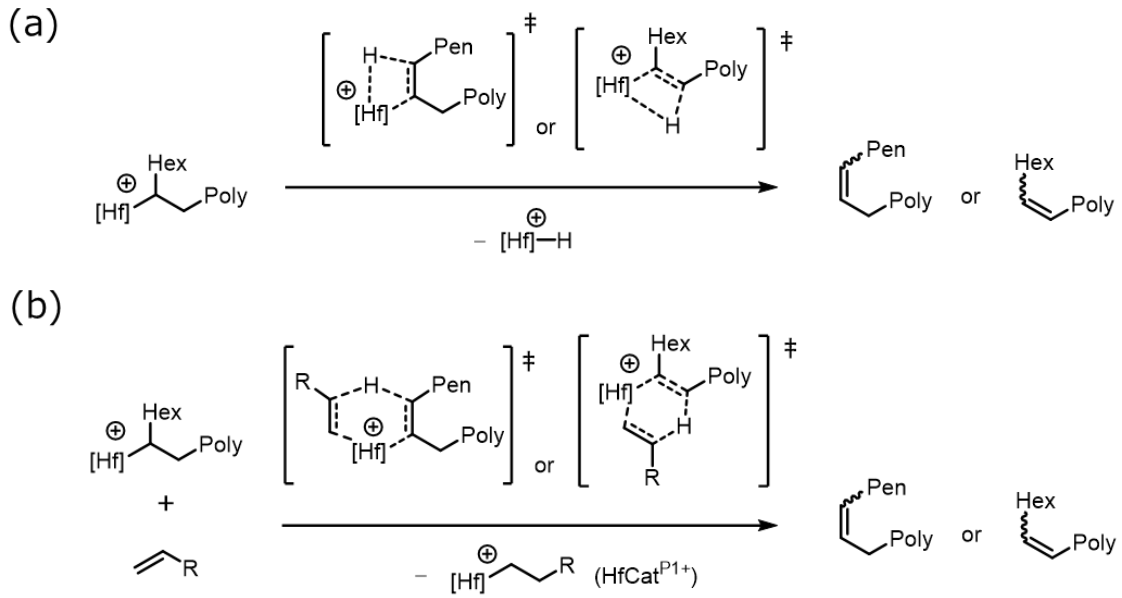

Figure 10. Schematic representation of possible chain termination reactions ((iii) in **Scheme 1**) from 2,1-inserted structure, (a) *β*-hydride elimination, where T in **Scheme 1** corresponds to none and Cat^*–T corresponds to the metal hydride complex $[Hf]^+$–H; and (b) *β*-hydride transfer, where T corresponds to a monomer and Cat^*–T corresponds to a monomer-inserted complex $HfCat^{P1+}$. "Poly" represents a 1-octene polymer chain, while "Hex" and "Pen" a hexyl and a pentyl group, respectively.

3.5.3.2. Relative Reaction Probability of *β*-Hydride Transfer to 1-Octene Insertion Higher with $B(C_6F_5)_4^-$ than with $MeB(C_6F_5)_3^-$

Figure 11 shows schematically the competition between *β*-hydride transfer and 1-octene insertion reactions from a 2,1-inserted complex. In the case of *β*-hydride transfer, both *β*-hydride atom and 1-octene monomer should come close to the active site of $HfCat^{Pn+}$, i.e., Hf atom. Hence, it can be reasonably considered that the IP structure also affects the *β*-hydride transfer reaction rate. To confirm this, I compare

the probabilities of β-hydride transfer reaction relative to 1-octene insertion reaction by estimating the numerical values of their reaction rates, k_2(tr) for β-hydride transfer reaction and k_2(in) for 1-octene insertion reaction from a 2,1-inserted complex. Under this assumption, k_2(tr)/k_2(in) determines the living character of the catalyst.

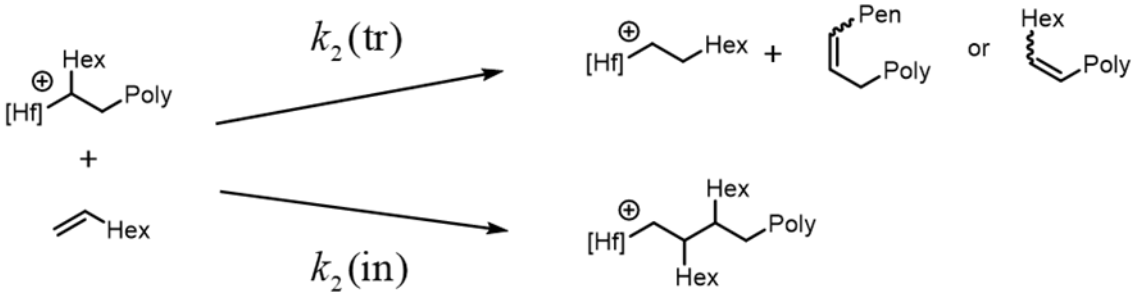

Figure 11. Schematic representation of competition between β-hydride transfer reaction and 1-octene insertion reaction from a 2,1-inserted HfCat^{Pn+} complex. k_2(tr) denotes the rate constant of β-hydride transfer reaction, while k_2(in) does that of 1-octene insertion reaction.

To evaluate k_2(tr) and k_2(in), it is necessary to consider the pre-equilibrium state for each reaction, as shown in **Figure 12**. The equilibrium constants K_d(tr) for β-hydride transfer reaction and K_d(in) for 1-octene insertion of 2,1-inserted complexes (**Figure 12**) can be estimated using the trajectories of equilibrium MD simulations. Thus, to estimate K_d(tr) and K_d(in), I analyzed all MD trajectories of the RM simulations (process 2(a) in Appendix A) where HfCat^{Pn+} is a 2,1-inserted complex (see Appendix G).

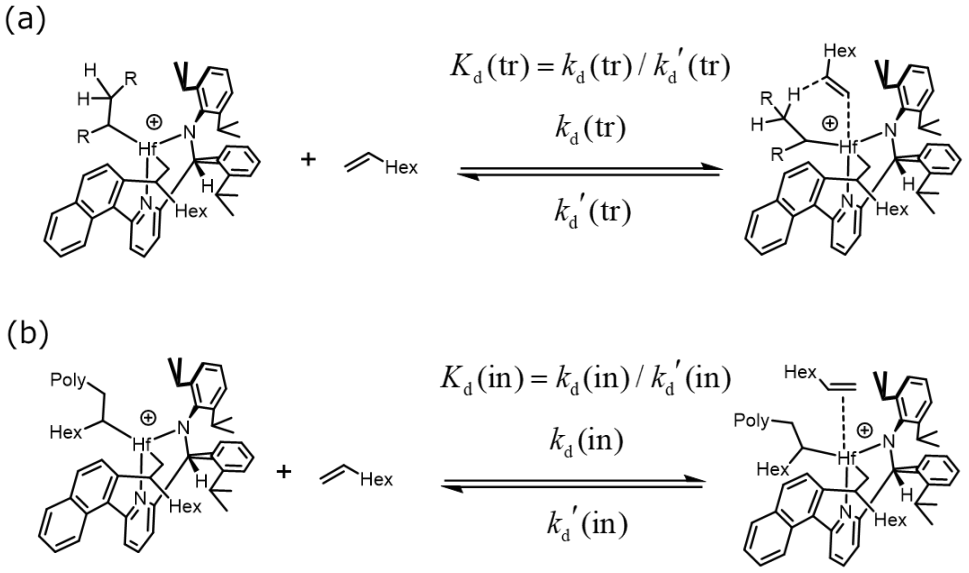

Figure 12. Schematic representation of the pre-equilibrium states of (a) *β*-hydride transfer reaction and (a) 1-octene insertion reaction from 2,1-inserted HfCat^{Pn+} complex. "R" represents alkyl groups. k_d and k_d' respectively represent association and dissociation constants, and K_d represents the equilibrium constant for each reaction.

Table 3 shows the calculated values of K_d(tr), K_d(in), k_2(tr), k_2(in), and the ratio k_2(tr)/k_2(in) of the HfCat^{Pn+}–MeB$(C_6F_5)_3^-$ and HfCat^{Pn+}–B$(C_6F_5)_4^-$ IP systems. It was revealed that both K_d(tr) and K_d(in) in the HfCat^{Pn+}–B$(C_6F_5)_4^-$ IP system are respectively larger than those in the HfCat^{Pn+}–MeB$(C_6F_5)_3^-$ one. This should be because, as I have demonstrated in Subsection 3.5.2, the B$(C_6F_5)_4^-$ anion is more likely to dissociate from HfCat^{Pn+} than the MeB$(C_6F_5)_3^-$ anion, so that 1-octene monomer coordination is less likely to compete with anion coordination. It is also noteworthy that the CAs also influence the *β*-hydride coordination to the Hf atom itself (see **Table H1** in Appendix H).

Table 3. Calculated pre-equilibrium constants K_d(in) and K_d(tr) and reaction constants k_2(in) and k_2(tr) for 1-octene insertion and β-hydride transfer reaction of HfCat^{Pn+}–MeB$(C_6F_5)_3^-$ and HfCat^{Pn+}–B$(C_6F_5)_4^-$ IP systems, and their ratio k_2(tr) / k_2(in).

IP system	K_d(tr) [a]	K_d(in) [a]	k_2(tr) [b]	k_2(in) [b]	k_2(tr) / k_2(in)
HfCat^{Pn+}–MeB$(C_6F_5)_3^-$	3.0×10^{-4}	1.6×10^{-3}	2.1×10^{-8}	7.1×10^{-3}	3.0×10^{-6}
HfCat^{Pn+}–B$(C_6F_5)_4^-$	9.3×10^{-4}	3.6×10^{-3}	6.6×10^{-8}	1.6×10^{-2}	4.1×10^{-6}

[a] Values are given in L·mol^{-1}. [b] Values are given in L·mol^{-1}·s^{-1}.

Accordingly, both k_2(tr) and k_2(in) are larger in the case of the HfCat^{Pn+}–B$(C_6F_5)_4^-$ IP system than the HfCat^{Pn+}–MeB$(C_6F_5)_3^-$ one. From the data in **Table 3** and the difference of 1.5 kcal/mol between the activation FE of 1,2-insertion and that of 2,1-insertion reaction [49], the frequency of β-hydride transfer reaction, i.e., chain termination reaction ((R4) in **Scheme 1**), can be estimated as about once in 10^6–10^7 insertion reactions ((R3) in **Scheme 1**) in both complexes. The estimated frequency of the termination reaction is relatively far from the experimentally reported value (one vinylidene formation per 4500 insertion reactions by the HfCat^{Pn+}–B$(C_6F_5)_4^-$ IP [42]), presumably due to the uncertainty of the activation FE values, which depends strongly on the adopted theoretical level of QM calculation. That is, the activation FEs might have been overestimated for β-hydride transfer reaction, or underestimated for 1-octene monomer insertion.

Furthermore, the ratio k_2(tr)/k_2(in) of the HfCat^{Pn+}–B$(C_6F_5)_4^-$ IP system was ~1.4 times higher than that of the HfCat^{Pn+}–MeB$(C_6F_5)_3^-$ one, which suggests the living character of the HfCat^{Pn+}–B$(C_6F_5)_4^-$ IP system is lower than that of the HfCat^{Pn+}–MeB$(C_6F_5)_3^-$ one. It should be noted that the difference in k_2(tr) or k_2(in) between the HfCat^{Pn+}–MeB$(C_6F_5)_3^-$ and HfCat^{Pn+}–B$(C_6F_5)_4^-$ IP systems directly reflects the

difference in K_d(tr) or K_d(in), since the same activation energy was assumed for both IP systems in each case of β-hydride transfer and 1-octene insertion reaction (see Appendix I). In other words, I did not consider the electronic effects of the CAs but considered only the dynamic effects. In this situation, the reason for the less living character of $HfCat^{Pn+}$–$B(C_6F_5)_4^-$ IP system lies in the ratio of K_d(tr)/K_d(in), which is about 1.4 times larger in the $HfCat^{Pn+}$–$B(C_6F_5)_4^-$ IP system than in the $HfCat^{Pn+}$–$MeB(C_6F_5)_3^-$ system due to the dynamic effect of the CAs (**Table 3**). This should be because the required condition for the candidate configuration of the β-hydride transfer reaction is more restrictive (or difficult to be realized) than that of the 1-octene insertion. In the case of β-hydride transfer reaction, the complex should necessarily take a more constrained six-membered ring structure, which needs more space around the active site, while a less constrained four-membered ring structure should be taken in the case of monomer insertion reaction. It is, therefore, reasonably suggested that the relative probability of β-hydride transfer reaction to that of 1-octene insertion after 2,1-insertion should be higher with the $HfCat^{Pn+}$–$B(C_6F_5)_4^-$ IP than with the $HfCat^{Pn+}$–$MeB(C_6F_5)_3^-$ IP system, since the former reaction should be more sensitive to the IP structures in the diffusion process, i.e., the dynamic effect of the CAs, than the latter. This should be a possible origin of the MWD being broader in the $HfCat^{Pn+}$–$B(C_6F_5)_4^-$ IP than the $HfCat^{Pn+}$–$MeB(C_6F_5)_3^-$ IP system.

3.6. Concluding Remarks

In this work, 1-octene polymerization reaction by the (pyridylamido)Hf catalyst with two counteranions (CAs), $MeB(C_6F_5)_3^-$ and $B(C_6F_5)_4^-$ was studied with the help of QM calculations and Red Moon (RM) simulations. I focused on the activities and the living characters of the catalytic systems, which are expected to be influenced by the IP structures.

First, I have certified that RM simulation reasonably reproduces the 1-octene polymerization reaction rate ((R2) and (R3) in **Scheme 1**) that is about twice larger in the $HfCat^{Pn+}$–$B(C_6F_5)_4^-$ IP system than in the $HfCat^{Pn+}$–$MeB(C_6F_5)_3^-$ one. This is because the 1-octene consumption rate with respect to the RM cycle is proportional to the frequency of the monomer coordination in the MD trajectories of the RM simulations, which is influenced by the dynamic effect of the CAs. Notably, in the $HfCat^{Pn+}$–$MeB(C_6F_5)_3^-$ IP system, I have observed the comparatively slow initiation ((R2) in **Scheme 1**) of the polymerization reaction as observed experimentally [42] and understood it emerges due to the strong coordinating ability of $MeB(C_6F_5)_3^-$. However, after the first insertion ((R3) in **Scheme 1**), the interaction between $HfCat^{Pn+}$ and $MeB(C_6F_5)_3^-$ is weakened by the steric hindrance of the inserted polymer chain and thus the insertion can proceed rapidly.

Then, the $HfCat^{Pn+}$–$MeB(C_6F_5)_3^-$ and $HfCat^{Pn+}$–$B(C_6F_5)_4^-$ IP structures during the polymerization reaction were investigated, which are expected as the origin of the difference in the polymerization reaction rates. I found that both IPs would be separated more or less by the growing polymeryl chain. However, $MeB(C_6F_5)_3^-$ can coordinate to $HfCat^{Pn+}$ even after the polymeryl chain becomes sufficiently bulky, while it is

interesting that $B(C_6F_5)_4^-$ is totally dissociated from the Hf center throughout the polymerization process.

Finally, I examined the possibility of the chain termination reaction ((R4) in **Scheme 1**) depending on the influence of the CAs. Although β-hydride elimination reaction and β-hydride transfer reaction can be generally considered as possible chain termination reaction mechanisms, I found that β-hydride transfer reaction is more reasonable from the QM calculations. According to this finding, since the chain termination reaction is experimentally observed only after 2,1-insertion, I analyzed the RM trajectories of 2,1-inserted $HfCat^{Pn+}$ to estimate and compare the reaction rate constants between 1-octene insertion and β-hydride transfer reactions. As a result, I found that the ratio of the chain termination reaction rate to that of insertion reaction is a little higher in the $HfCat^{Pn+}$–$B(C_6F_5)_4^-$ IP system than in the $HfCat^{Pn+}$–$MeB(C_6F_5)_3^-$ one, which is consistent with the experimental observation of the larger polydispersity index (PDI) value in the $HfCat^{Pn+}$–$B(C_6F_5)_4^-$ IP system than in the $HfCat^{Pn+}$–$MeB(C_6F_5)_3^-$ one [38]. It is reasonably understood that the β-hydride transfer reaction would be more sensitive to the IP structures in the MD trajectories, i.e., the dynamic effect of the CAs, because it involves a six-membered structure, whereas 1-octene insertion involves a less constrained four-membered one.

It might be true that there are some other possible causes as well for the broader molecular weight distribution (MWD) observed in the $HfCat^{Pn+}$–$B(C_6F_5)_4^-$ IP system, such as multiplicity of the active species or an increase of the active species during the polymerization reaction due to the relatively slow catalyst activation reaction compared to the monomer insertion reaction. However, it can be concluded that the

present theoretical study reasonably suggests that the dynamic effect of the CAs affects not only the polymerization reaction rate ((R2) and (R3) in **Scheme 1**) but also the chain termination reaction rate ((R4) in **Scheme 1**), which should be one of the possible reasons for the MWDs that are dependent on CAs.

It is notable that this work demonstrates the potential feasibility of RM simulation as a powerful tool to reveal the dynamic aspect of the overall CP reaction, which is difficult to model or compute with conventional QM or MD methods by themselves.

Finally, I have to note that there is room for testing my hypothesis regarding the MWDs. It would be more valuable to quantitatively examine how the estimated kinetic constants in this article affect the PDI values of the produced polymer, for example, by explicitly considering the termination reaction in RM simulation. Therefore, I expect this issue to be addressed in the near future through the establishment of a method to quantitatively evaluate the polymer's physical properties based on the RM simulations.

Appendix A:

Detailed Algorithm of Red Moon Simulation

For the application of the RM methodology, I first assume a reaction scheme which consists of a set of chemical reactions R_1, R_2, … . Then, I provide them their corresponding activation energies $\Delta E_{\mathrm{a}}^{\mathrm{R}_1}$, $\Delta E_{\mathrm{a}}^{\mathrm{R}_2}$, … . Each activation energy is obtained properly as the "free" energy of activation that is estimated in advance, within the continuum model, the free energy gradient method [62–64], or some experimental methods for each chemical reaction.

The present RM simulation consists of a combination of the following processes:

1. Equilibrate the whole system through the classical NVT-MD simulation and obtain configuration states.

2. Generate reaction steps with the NVT-MC procedure and classical NVT-MD simulation, consisting of the following steps:

   (a) Search for some reactant molecules in given configuration states, according to some criteria for the possible chemical reactions R_1, R_2, …. As a result, the number of candidates $N_{\mathrm{cand}}^{\mathrm{R}_i}$ for each possible chemical reaction is obtained in given configuration states.

   (b) In principle, randomly select a chemical reaction R_i among R_1, R_2, … according to their corresponding relative weights of selection w^{R_1}, w^{R_2}, … , where a relative weight w^{R_i} for R_i is expressed by the product of $N_{\mathrm{cand}}^{\mathrm{R}_i}$ and $\exp\left(-\beta \Delta E_{\mathrm{a}}^{\mathrm{R}_i}\right)$ as follows,

$$w^{\mathrm{R}_i} = N_{\mathrm{cand}}^{\mathrm{R}_i} \exp\left(-\beta \Delta E_{\mathrm{a}}^{\mathrm{R}_i}\right). \quad \text{(A1)}$$

If there is no candidate pair, return to the process 1 instead of the following step (c) and (d) to obtain new configuration states.

(c) Switch the atomic potential parameters and potential function forms of the reactant atoms in the selected reactant state "*r*" to the product ones, and virtually react them to generate a possible configuration states, relaxing the whole system to obtain the product state "*s*" through a short NVT-MD simulation.

(d) Compute the energy change of the system $\Delta U_{rs} (= U_s - U_r)$ and accept (or reject) the reaction step according to the transition probability $W_{r \to s}$ under the Metropolis scheme [65–67],

$$W_{r \to s} = \min\left\{1, \exp\left[-\beta \Delta U_{rs}\right]\right\}. \quad \text{(A2)}$$

In the present study, ΔU_{rs} is approximately estimated as follows,

$$\Delta U_{rs} = \Delta U_{rs}^{\mathrm{MM}} + \Delta U_0^{\mathrm{reac}}, \quad \text{(A3)}$$

where $\Delta U_{rs}^{\mathrm{MM}}$ is the naïve difference of total potential energies obtained in the MM force field, corresponding to a change of the atomic potential parameters and potential function forms, and $\Delta U_0^{\mathrm{reac}}$ represents a proper correction of the "zero" point of energy by the corresponding potential energy of the reaction.

3. If the molecular mixture composition might scarcely change, then stop. Otherwise, return to process 2.

Appendix B:

Average Number of All Reaction Candidates and All Accepted Reaction and Their Ratio Per One RM Simulation

The reaction rate in RM simulation can be determined by the two possible factors: the number of reaction candidates and the ratio of accepted reactions to all reaction candidates. I have investigated the number of all accepted reactions $\sum_j N_{\mathrm{Acc}}$ and all reaction candidates $\sum_j \sum_i N_{\mathrm{cand}}^{\mathrm{R}i,j}$ found in the process 2(a) in Appendix A, where *i* denoted the index of reaction and *j* denotes the index of RM cycles (*j* = 1–3000), for 10 RM simulations of each HfCat^{Pn+}–MeB(C_6F_5)$_3^-$ and HfCat^{Pn+}–B(C_6F_5)$_4^-$ IP systems. **Table B1** shows the average numbers of $\sum_j N_{\mathrm{Acc}}$, $\sum_j \sum_i N_{\mathrm{cand}}^{\mathrm{R}i,j}$, and $\sum_j N_{\mathrm{Acc}} / \sum_j \sum_i N_{\mathrm{cand}}^{\mathrm{R}i,j}$ per one RM simulation ($\overline{\sum_J N_{\mathrm{Acc}}}$, $\overline{\sum_J \sum_\iota N_{\mathrm{cand}}^{\mathrm{R}\iota,J}}$, and $\overline{\sum_J N_{\mathrm{Acc}} / \sum_J \sum_\iota N_{\mathrm{cand}}^{\mathrm{R}\iota,J}}$) for HfCat^{Pn+}–MeB($C_6F_5$)$_3^-$ and HfCat^{Pn+}–B(C_6F_5)$_4^-$ IP systems. It was clarified that the difference in the 1-octene consumption rate between HfCat^{Pn+}–MeB(C_6F_5)$_3^-$ and HfCat^{Pn+}–B(C_6F_5)$_4^-$ IP systems shown in **Figure 3** comes from the difference in the number of all reaction candidates $\sum_j \sum_i N_{\mathrm{cand}}^{\mathrm{R}i,j}$.

Table B1. Average number of all reaction candidate $\sum_j \sum_i N_{\mathrm{cand}}^{\mathrm{R}_{i,j}}$, all accepted reaction $\sum_j N_{\mathrm{Acc}}$, and their ratio $\sum_j N_{\mathrm{Acc}} / \sum_j \sum_i N_{\mathrm{cand}}^{\mathrm{R}_{i,j}}$ per one RM simulation for 3000 RM cycles in $\mathrm{HfCat}^{\mathrm{P}n+}$–$\mathrm{MeB(C_6F_5)_3^-}$ and $\mathrm{HfCat}^{\mathrm{P}n+}$–$\mathrm{B(C_6F_5)_4^-}$ IP systems. *j* represents the index of RM cycles.

IP system	$\overline{\sum_J N_{\mathrm{Acc}}}$	$\overline{\sum_J \sum_\iota N_{\mathrm{cand}}^{\mathrm{R}_{\iota,J}}}$	$\overline{\sum_J N_{\mathrm{Acc}} / \sum_J \sum_\iota N_{\mathrm{cand}}^{\mathrm{R}_{\iota,J}}}$
$\mathrm{HfCat}^{\mathrm{P}n+}$–$\mathrm{MeB(C_6F_5)_3^-}$	33.4 ± 5.0	499 ± 73	0.070 ± 0.011
$\mathrm{HfCat}^{\mathrm{P}n+}$–$\mathrm{B(C_6F_5)_4^-}$	62.9 ± 3.0	1023 ± 116	0.69 0.007

Appendix C:

Estimation of the Average Time Length of 1 RM Cycle

To estimate the time corresponding to 1 RM cycle, I assumed the second-order reaction

$$\mathrm{HfCat}^{\mathrm{P}n+} + \text{1-OCT} \xrightarrow{k_2} \mathrm{HfCat}^{\mathrm{P}(n+1)+} , \tag{C1}$$

where 1-OCT denotes 1-octene monomer, and the following equation can be obtained from the second-order reaction rate law;

$$k_2 = \frac{\ln[\text{1-OCT}]_0 - \ln[\text{1-OCT}]_\tau}{\int_0^\tau [\mathrm{HfCat}^{\mathrm{P}n+}]_t \, dt}, \tag{C2}$$

where k_2 is a polymerization rate constant and τ is an arbitrary time. Since $[\mathrm{HfCat}^{\mathrm{P}n+}]$ is constant in the RM simulation, τ can be obtained as follows, using the k_2 values that can be estimated from the experimental report [42] and [1-OCT]τ value in *n* RM cycle in the simulation,

$$\tau = \frac{\ln[\text{1-OCT}]_0 - \ln[\text{1-OCT}]_\tau}{k_2[\mathrm{HfCat}^{\mathrm{P}n+}]}, \tag{C3}$$

which corresponds to the time length of *n* RM cycles. In this way, the average time length of 1 RM cycle, *τ/n* (τ_{RM}), can be numerically obtained using Eq. (C3).

Table C1 shows the obtained average time length of 1 RM simulation for each of the $HfCat^{Pn+}$–$MeB(C_6F_5)_3^-$ and $HfCat^{Pn+}$–$B(C_6F_5)_4^-$ IP systems. From this result, we estimated that 1 RM cycle roughly corresponds on average to 25 μs in the experiment.

Table C1. Obtained average time length of 1RM cycle (τ_{RM}) in $HfCat^{Pn+}$–$MeB(C_6F_5)_3^-$ and $HfCat^{Pn+}$–$B(C_6F_5)_4^-$ IP systems.

IP system	τ_{RM}
$HfCat^{Pn+}$–$MeB(C_6F_5)_3^-$	22 μs
$HfCat^{Pn+}$–$B(C_6F_5)_4^-$	28 μs

Appendix D:

Details of MD Simulation to Obtain RDF of 1-Octene Monomers

For each model system, MD calculations were executed using the pmemd module in AMBER14 [53] under the periodic boundary condition in NVT ensemble at 323 K for 200 ns to obtain radial distribution function (RDF) between the sp^2 carbon atoms of 1-octene monomer and Hf atom in each model system. The weak-coupling algorithm with a time constant of 1 ps was applied to control the temperature. The integration time step was set to 1 fs, and the SHAKE algorithm was used to constrain the bond distances including hydrogen atoms. I employed the same force field parameters with those used in the RM simulations.

Appendix E:

Method to Obtain FE Map from MD Trajectories

To obtain the FE maps from the MD trajectory using the two axes, i.e., the interatomic distance r between Hf and B atoms and the angle ϕ formed between the straight lines connecting Hf to B and N in pyridine ring, the whole region in the FE map was divided into each region with a bin size of (0.05 Å, 2.0°). We calculated the following Z_i value in each region i,

$$Z_i = \frac{W_i}{\sum W_i}, \tag{E1}$$

where W_i corresponds to a number of states in each region. Then, the free energy of the region i can be described by

$$FE = -k_B T \ln(Z_i). \tag{E2}$$

By calculating FE for each region, we obtained the FE maps in **Figure 6** and **Figure 8**.

Appendix F:

FE Diagram of *β*-Hydride Transfer Reaction

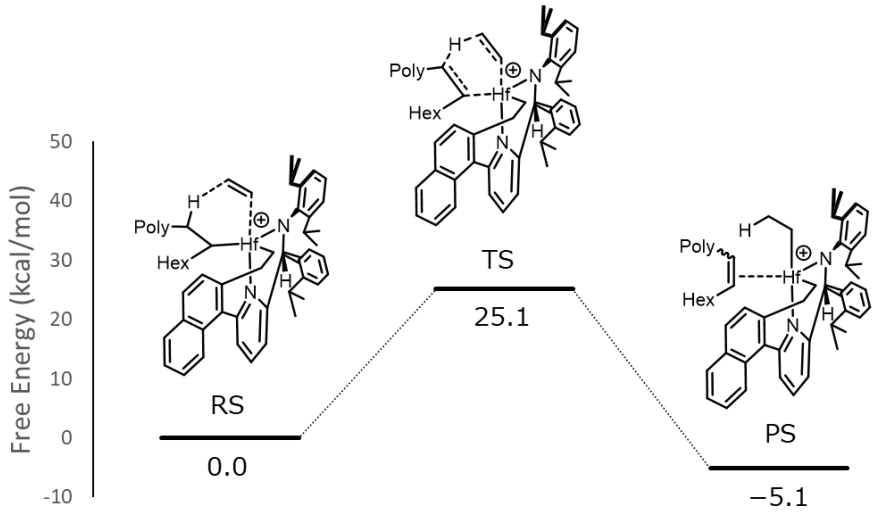

Figure F1. FE diagram of *β*-hydride transfer reaction with an ethylene monomer. The QM calculations were performed at the M06/def2-TZVPP level of theory.

Appendix G:

Estimation of K_d(tr) and K_d(in) Values

Numerically, K_d values can be estimated using Eq. (2.2). To evaluate the concentration of the isolated catalyst and monomer ([$HfCat^+$] and [1-OCT]), or the complex of the catalyst and monomer taking the favorable configuration

([$HfCat^{+}\cdots$1-OCT]) for each reaction in MD trajectories, it is necessary to set some criteria to distinguish between the former and the latter configurations.

For the pre-equilibrium constants K_d(tr) and K_d(in) in **Figure 12**, the following criteria were considered to determine the reaction candidate configurations, referring to the reactant structures obtained from the QM calculation (see Section IV); For β-hydride transfer (K_d(tr)), the dihedral angle between the Hf–C_α (polymeryl) and β-H–C_β (polymeryl) is within 35.0 degrees, and both two distances between Hf and one sp^2 carbon atom in 1-octene and between β-H and the other sp^2 carbon atom are within 4 Å and 5 Å, respectively. For 1-octene insertion (K_d(in)), both two distances between Hf and one sp^2 carbon atom in 1-octene and between C_α (polymeryl) and the other sp^2 carbon atom are within 5 Å.

Appendix H:

Pre-equilibrium State for β-Hydride Elimination and Its Constant K_d(el)

I investigated the equilibrium constant of β-hydride coordination to the Hf atom K_d(el), which corresponds to the pre-equilibrium state for β-hydride elimination reaction of 2,1-inserted complex as shown in **Figure H1**. The equilibrium constant K_d(el) can be estimated using Eq. (2.2). To examine the influence of the $MeB(C_6F_5)_3^-$ or $B(C_6F_5)_4^-$ counteranions on the K_d(el), I analyzed the MD trajectories of the RM simulations where $HfCat^{Pn+}$ corresponds to the 2,1-inserted complex.

To determine the configurations in the right side of the pre-equilibrium states (**Figure H1**), the following criteria were considered; the dihedral angle between the Hf–C_α (polymeryl) and β-H–C_β (polymeryl) is within 35.0 degrees, and the distances between Hf and β-H atom is within 3 Å.

Table H1 shows the obtained K_d(el) values for the HfCat^{Pn+}–MeB$(C_6F_5)_3^-$ and HfCat^{Pn+}–B$(C_6F_5)_4^-$ IP systems. I found that β-hydride coordination is also influenced by the counteranions. The K_d(el) is smaller in HfCat^{Pn+}–MeB$(C_6F_5)_3^-$ IP system than in the HfCat^{Pn+}–B$(C_6F_5)_4^-$ one. That should be because MeB$(C_6F_5)_3^-$ forms more ISIP than B$(C_6F_5)_4^-$, which thus makes less space for β-hydride to coordinate to the Hf atom.

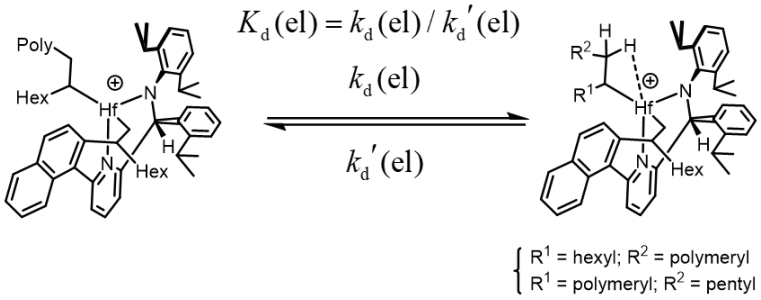

Figure H1. Schematic representation of the pre-equilibrium state of β-hydride elimination reaction from a 2,1-inserted HfCat^{Pn+} complex.

Table H1. Equilibrium constants K_d(el) in HfCat^{Pn+}–MeB$(C_6F_5)_3^-$ and HfCat^{Pn+}–B$(C_6F_5)_4^-$ IP systems.

IP system	K_d (el)
HfCat^{Pn+}–MeB$(C_6F_5)_3^-$	0.10
HfCat^{Pn+}–B$(C_6F_5)_4^-$	0.16

Appendix I:

Estimation of k_2 Values

To calculate the values of k_2 for 1-octene insertion reaction and β-hydride transfer reaction, the corresponding k_as and K_ds need to be calculated from QM and MD simulations. As for the 1-octene insertion, I have already calculated the activation free energies of 1-octene insertion reaction using ethylene-inserted active species of (pyridylamido)Hf catalyst, which are 17.6 and 17.9 kcal/mol, respectively with $MeB(C_6F_5)_3^-$ and $B(C_6F_5)_4^-$ anions. In this study, I must assume 1-octene insertion from a 2,1-inserted structure. However, due to the computational cost, I could not perform QM calculations of 1-octene insertion reaction from a 2,1-inserted structure. Thus, I decided to approximate the activation energies of 1-octene insertion reaction from 2,1-inserted structure to 18.0 kcal/mol for both $HfCat^{Pn+}$–$MeB(C_6F_5)_3^-$ and $HfCat^{Pn+}$–$B(C_6F_5)_4^-$ IP systems. As for the β-hydride transfer, I used the activation free energy obtained with the cationic model system described in Appendix F (25.1 kcal/mol) for both $HfCat^{Pn+}$–$MeB(C_6F_5)_3^-$ and $HfCat^{Pn+}$–$B(C_6F_5)_4^-$ IP systems. Therefore, the differences in k_2(in) or k_2(tr) between $HfCat^{Pn+}$–$MeB(C_6F_5)_3^-$ and $HfCat^{Pn+}$–$B(C_6F_5)_4^-$ IP systems directly reflect the differences in K_d(in) or K_d(tr), respectively.

References

[1] Stürzel, M.; Mihan, S.; Mülhaupt, R. *Chem. Rev.* **2016**, *116*, 1398.

[2] Carraher Jr, C. E. *Seymour/Carraher's polymer chemistry*; CRC press, 2003; Vol. 16.

[3] Chanda, M. *Introduction to polymer science and chemistry: a problemsolving approach*; CRC Press, 2013.

[4] Christianson, M. D.; Tan, E. H. P.; Landis, C. R. *J. Am. Chem. Soc.* **2010**, *132*, 11461, PMID: 20672801.

[5] Nelsen, D. L.; Anding, B. J.; Sawicki, J. L.; Christianson, M. D.; Arriola, D. J.; Landis, C. R. *ACS Catal.* **2016**, *6*, 7398.

[6] Chen, C.-H.; Shih, W.-C.; Hilty, C. *J. Am. Chem. Soc.* **2015**, *137*, 6965, PMID: 25961793.

[7] Jensen, F. *Introduction to computational chemistry*; John Wiley & Sons, 2017.

[8] Kawamura-Kuribayashi, H.; Koga, N.; Morokuma, K. *J. Am. Chem. Soc.* **1992**, *114*, 8687.

[9] Lanza, G.; Fragalà, I. L.; Marks, T. J. *J. Am. Chem. Soc.* **2000**, *122*, 12764.

[10] Lanza, G.; Fragalà, I. L.; Marks, T. J. *Organometallics* **2001**, *20*, 4006.

[11] Zurek, E.; Ziegler, T. *Faraday Discuss.* **2003**, *124*, 93.

[12] Xu, Z.; Vanka, K.; Ziegler, T. *Organometallics* **2004**, *23*, 104.

[13] Ziegler, T.; Vanka, K.; Xu, Z. *C. R. Chim.* **2005**, *8*, 1552.

[14] Busico, V.; Cipullo, R.; Pellecchia, R.; Ronca, S.; Roviello, G.; Talarico, G. *Proc. Natl. Acad. Sci.* **2006**, *103*, 15321.

[15] Tomasi, S.; Razavi, A.; Ziegler, T. *Organometallics* **2007**, *26*, 2024.

[16] Motta, A.; Fragalà, I. L.; Marks, T. J. *J. Am. Chem. Soc.* **2007**, *129*, 7327.

[17] Motta, A.; Fragalà, I. L.; Marks, T. J. *J. Am. Chem. Soc.* **2008**, *130*, 16533.

[18] De Rosa, C.; Di Girolamo, R.; Talarico, G. *ACS Catal.* **2016**, *6*, 3767.

[19] Matsumoto, K.; Takayanagi, M.; Sankaran, S. K.; Koga, N.; Nagaoka, M. *Organometallics* **2018**, *37*, 343.

[20] Frenkel, D.; Smit, B. *Understanding molecular simulation: from algorithms to applications*; Elsevier, 2001; Vol. 1.

[21] Correa, A.; Cavallo, L. *J. Am. Chem. Soc.* **2006**, *128*, 10952.

[22] Yang, S.; Ziegler, T. *Organometallics* **2006**, *25*, 887.

[23] Rowley, C. N.; Woo, T. K. *Organometallics* **2011**, *30*, 2071.

[24] Matsumoto, K.; Sandhya, K. S.; Takayanagi, M.; Koga, N.; Nagaoka, M. *Organometallics* **2016**, *35*, 4099.

[25] Nagaoka, M.; Suzuki, Y.; Okamoto, T.; Takenaka, N. *Chem. Phys. Lett.* **2013**, *583*, 80.

[26] Suzuki, Y.; Nagaoka, M. *J. Chem. Phys.* **2017**, *146*, 204102.

[27] Takenaka, N.; Suzuki, Y.; Sakai, H.; Nagaoka, M. *J. Phys. Chem. C* **2014**, *118*, 10874.

[28] Takenaka, N.; Sakai, H.; Suzuki, Y.; Uppula, P.; Nagaoka, M. *J. Phys. Chem. C* **2015**, *119*, 18046.

[29] Miyazaki, K.; Takenaka, N.; Fujie, T.; Watanabe, E.; Yamada, Y.; Yamada, A.; Nagaoka, M. *ACS Appl. Mater. Interfaces* **2019**, *11*, 15623.

[30] Suzuki, Y.; Koyano, Y.; Nagaoka, M. *J. Phys. Chem. B* **2015**, *119*, 6776, PMID: 25973839.

[31] Matsumoto, K.; Takayanagi, M.; Suzuki, Y.; Koga, N.; Nagaoka, M. *J. Comput. Chem.* **2019**, *40*, 421.

[32] Rao, Z.; Takayanagi, M.; Nagaoka, M. *J. Phys. Chem. C* **2020**, *124*, 16895.

[33] Boussie, T. R.; Diamond, G. M.; Goh, C.; Hall, K. A.; LaPointe, A. M.; Leclerc, M.; Lund, C.; Murphy, V.; Shoemaker, J. A. W.; Tracht, U.; Turner, H.; Zhang, J.; Uno, T.; Rosen, R. K.; Stevens, J. C. *J. Am. Chem. Soc.* **2003**, *125*, 4306.

[34] Boussie, T. R.; Diamond, G. M.; Goh, C.; Hall, K. A.; LaPointe, A. M.; Leclerc, M. K.; Murphy, V.; Shoemaker, J. A. W.; Turner, H.; Rosen, R. K.; Stevens, J. C.; Alfano, F.; Busico, V.; Cipullo, R.; Talarico, G. *Angew. Chem., Int. Ed.* **2006**, *45*, 3278.

[35] Chum, P. S.; Swogger, K. W. *Prog. Polym. Sci.* **2008**, *33*, 797.

[36] Arriola, D. J.; Carnahan, E. M.; Hustad, P. D.; Kuhlman, R. L.; Wenzel, T. T. *Science* **2006**, *312*, 714.

[37] Wenzel, T. T.; Arriola, D. J.; Carnahan, E. M.; Hustad, P. D.; Kuhlman, R. L. *Top. Organomet. Chem.* **2009**, *26*, 65.

[38] Domski, G. J.; Lobkovsky, E. B.; Coates, G. W. *Macromolecules* **2007**, *40*, 3510.

[39] Busico, V.; Cipullo, R.; Pellecchia, R.; Rongo, L.; Talarico, G.; Macchioni, A.; Zuccaccia, C.; Froese, R. D. J.; Hustad, P. D. *Macromolecules* **2009**, *42*, 4369.

[40] Niu, A.; Stellbrink, J.; Allgaier, J.; Richter, D.; Hartmann, R.; Domski, G. J.; Coates, G. W.; Fetters, L. J. *Macromolecules* **2009**, *42*, 1083.

[41] Frazier, K. A.; Froese, R. D.; He, Y.; Klosin, J.; Theriault, C. N.; Vosejpka, P. C.; Zhou, Z.; Abboud, K. A. *Organometallics* **2011**, *30*, 3318.

[42] Cueny, E. S.; Johnson, H. C.; Anding, B. J.; Landis, C. R. *J. Am. Chem. Soc.* **2017**, *139*, 11903.

[43] Domski, G. J.; Eagan, J. M.; De Rosa, C.; Di Girolamo, R.; LaPointe, A. M.; Lobkovsky, E. B.; Talarico, G.; Coates, G. W. *ACS Catalysis* **2017**, *7*, 6930.

[44] Cueny, E. S.; Landis, C. R. *ACS Catalysis* **2019**, *9*, 3338.

[45] Yang, F.; Wang, X.; Ma, Z.; Wang, B.; Pan, L.; Li, Y. *Polymers* **2020**, *12*, 89.

[46] Jia, L.; Yang, X.; Stern, C. L.; Marks, T. J. *Organometallics* **1997**, *16*, 842.

[47] Froese, R. D. J.; Hustad, P. D.; Kuhlman, R. L.; Wenzel, T. T. *J. Am. Chem. Soc.* **2007**, *129*, 7831.

[48] Zuccaccia, C.; Busico, V.; Cipullo, R.; Talarico, G.; Froese, R. D. J.; Vosejpka, P. C.; Hustad, P. D.; Macchioni, A. *Organometallics* **2009**, *28*, 5445.

[49] Misawa, N.; Suzuki, Y.; Saha, S.; Koga, N.; Nagaoka, M. *Organometallics* **2021**, *40*, 48.

[50] Wang, J.; Wolf, R. M.; Caldwell, J. W.; Kollman, P. A.; Case, D. A. *J. Comput. Chem.* **2004**, *25*, 1157.

[51] Besler, B. H.; Merz, K. M.; Kollman, P. A. *J. Comput. Chem.* **1990**, *11*, 431.

[52] Singh, U. C.; Kollman, P. A. *J. Comput. Chem.* **1984**, *5*, 129.

[53] Case, D.; Babin, V.; Berryman, J.; Betz, R.; Cai, Q.; Cerutti, D.; T.E. Cheatham, I.; Darden, T.; Duke, R.; Gohlke, H.; Goetz, A.; Gusarov, S.; Homeyer, N.; Janowski, P.; Kaus, J.; Kolossv´ary, I.; Kovalenko, A.; Lee, T.; LeGrand, S.; Luchko, T.; Luo, R.; Madej, B.; Merz, K.; Paesani, F.; Roe, D.; Roitberg, A.; Sagui, C.; Salomon-Ferrer, R.; Seabra, G.; Simmerling, C.; Smith, W.; Swails, J.; Walker, R.; Wang, J.; Wolf, R.; Wu, X.; Kollman, P. *AMBER 14*; University of California: San Francisco, 2014.

[54] Frisch, M. J.; Trucks, G. W.; Schlegel, H. B.; Scuseria, G. E.; Robb, M. A.; Cheeseman, J. R.; Scalmani, G.; Barone, V.; Petersson, G. A.; Nakatsuji, H.; Li, X.; Caricato, M.; Marenich, A. V.; Bloino, J.; Janesko, B. G.; Gomperts, R.; Mennucci, B.; Hratchian, H. P.; Ortiz, J. V.; Izmaylov, A. F.; Sonnenberg, J. L.; Williams-Young, D.; Ding, F.; Lipparini, F.; Egidi, F.; Goings, J.; Peng, B.; Petrone, A.; Henderson, T.; Ranasinghe, D.; Zakrzewski, V. G.; Gao, J.; Rega, N.; Zheng, G.; Liang, W.; Hada, M.; Ehara, M.; Toyota, K.; Fukuda, R.; Hasegawa, J.; Ishida, M.; Nakajima, T.; Honda, Y.; Kitao, O.; Nakai, H.; Vreven, T.; Throssell, K.; Montgomery, J. A., Jr.; Peralta, J. E.; Ogliaro, F.; Bearpark, M. J.; Heyd, J. J.; Brothers, E. N.; Kudin, K. N.; Staroverov, V. N.; Keith, T. A.; Kobayashi, R.; Normand, J.; Raghavachari, K.; Rendell, A. P.; Burant, J. C.; Iyengar, S. S.; Tomasi, J.; Cossi, M.; Millam, J. M.; Klene, M.; Adamo, C.;

Cammi, R.; Ochterski, J. W.; Martin, R. L.; Morokuma, K.; Farkas, O.; Foresman, J. B.; Fox, D. J. Gaussian16 Revision C.01. 2016; Gaussian Inc. Wallingford CT.

[55] Zhao, Y.; Truhlar, D. G. *Theor. Chem. Acc.* **2008**, *120*, 215.

[56] Zhao, Y.; Truhlar, D. G. *J. Chem. Phys.* **2006**, *125*, 194101.

[57] Marenich, A. V.; Cramer, C. J.; Truhlar, D. G. *J. Phys. Chem. B* **2009**, *113*, 6378.

[58] Lohrenz, J. C. W.; Woo, T. K.; Ziegler, T. *J. Am. Chem. Soc.* **1995**, *117*, 12793.

[59] Talarico, G.; Budzelaar, P. H. M. *Organometallics* **2008**, *27*, 4098.

[60] Rappé, A. K.; Skiff, W. M.; Casewit, C. J. *Chem. Rev.* **2000**, *100*, 1435.

[61] Talarico, G.; Busico, V.; Cavallo, L. *Organometallics* **2004**, *23*, 5989.

[62] Okuyama-Yoshida, N.; Nagaoka, M.; Yamabe, T. *Int. J. Quantum Chem.* **1998**, *70*, 95.

[63] Nagaoka, M.; Okuyama-Yoshida, N.; Yamabe, T. *J. Phys. Chem. A* **1998**, *102*, 8202.

[64] Kitamura, Y.; Takenaka, N.; Koyano, Y.; Nagaoka, M. In *Quantum Modeling of Complex Molecular Systems*; Rivail, J.-L., Ruiz-Lopez, M., Assfeld, X., Eds.; Springer International Publishing: Cham, 2015; pp 219–252.

[65] Allen, M.; Allen, M.; Tildesley, D.; ALLEN, T.; Tildesley, D. *Computer Simulation of Liquids*; Oxford Science Publ; Clarendon Press, 1989.

[66] Heermann, D. W. *Computer Simulation Methods in Theoretical Physics*; Springer, 1990; pp 8–12.

[67] Metropolis, N.; Rosenbluth, A. W.; Rosenbluth, M. N.; Teller, A. H.; Teller, E. *J. Chem. Phys.* **1953**, *21*, 1087.

Chapter 4

General Conclusion

In this thesis, I investigated the effect of counteranions (CAs) on olefin polymerization reaction by (pyridylamido)Hf(IV) catalyst with the commonly used boron-based CAs, $MeB(C_6F_5)_3^-$ and $B(C_6F_5)_4^-$. For a comprehensive understanding of the effect of the CAs from both dynamic and electronic points of view, I performed molecular dynamics (MD) and quantum mechanical (QM) studies to analyze the diffusion and activation processes of monomer insertion reaction, respectively. In addition, to better understand the catalytic polymerization (CP) reaction process in the presence of CAs, I also adopted Red Moon (RM) method, which can reasonably simulate the overall CP reaction process as a succession of monomer insertion reactions.

In Chapter 2, the 1-octene insertion reaction by the cationic active species of (pyridylamido)Hf(IV) catalyst ($HfCat^+$) was investigated, focusing on the effect of $MeB(C_6F_5)_3^-$ and $B(C_6F_5)_4^-$ on the catalyst activity. QM calculation showed a remarkable difference in TS structures that $HfCat^+$–$MeB(C_6F_5)_3^-$ complex forms an "inner-sphere" ion pair (ISIP), while $HfCat^+$–$B(C_6F_5)_4^-$ forms an "outer-sphere" ion pair (OSIP). However, the activation free energies of the 1-octene insertion reaction by both complexes are almost identical to each other due to the trade-off relationship between the stability of the cationic system and cation–anion interaction energy, i.e., the electronic effect of the CAs. Meanwhile, replica exchange molecular dynamics (REMD) simulation has revealed that the time duration of the $HfCat^+$ capturing 1-octene monomers throughout the REMD trajectories of $HfCat^+$–$B(C_6F_5)_4^-$ complex was ~2.5

times as large as that of $HfCat^{+}$–$MeB(C_6F_5)_3^{-}$ one due to the dynamic effect of the CAs. In other words, $B(C_6F_5)_4^{-}$ is more likely to dissociate from $HfCat^{+}$ to form OSIP than $MeB(C_6F_5)_3^{-}$, and thus allows monomers to approach $HfCat^{+}$ more easily. Using these microscopic data, I numerically evaluated the 1-octene polymerization reaction rate constants based on the chemical kinetic formulation and succeeded in reproducing qualitatively the experimentally observed tendency of the polymerization reaction with $B(C_6F_5)_4^{-}$ faster than with $MeB(C_6F_5)_3^{-}$. Finally, it was theoretically elucidated that the monomer capture step in the diffusion process, which is largely influenced by the dynamic effect of the CAs, determines the overall polymerization reaction rates in this catalytic system, rather than the following monomer insertion step in the activation process. I believe that this is the first example of numerically estimating the CP reaction rate constant by using MD and QM methods in combination.

In Chapter 3, atomistic simulation of the whole 1-octene polymerization reaction process, i.e., a succession of monomer insertion reaction, by (pyridylamido)Hf(IV) catalyst based on RM methodology was conducted in the presence of the CAs, $MeB(C_6F_5)_3^{-}$ and $B(C_6F_5)_4^{-}$ to investigate the effect of the CAs on the activities and the living characters of the catalytic systems, which affect the polymer's physical and mechanical properties. I demonstrated that RM simulation reasonably reproduces the faster reaction rate with $B(C_6F_5)_4^{-}$ than with $MeB(C_6F_5)_3^{-}$, since the 1-octene consumption rate with respect to RM cycle proportional to the total number of reaction candidates, which reflects the dynamic effect of the CAs. Notably, the initiation of polymerization reaction with $MeB(C_6F_5)_3^{-}$ is comparatively slow due to the strong coordinating ability of $MeB(C_6F_5)_3^{-}$; however, after the first insertion, $MeB(C_6F_5)_3^{-}$ would be separated from the active site by the steric hindrance of the inserted polymer

and thus monomer insertions can proceed drastically. Then I investigated the ion pair (IP) structure consisting of each CA and the cationic (pyridylamido)Hf(IV) catalyst with a growing polymer chain ($HfCat^{Pn+}$) in the RM simulations, which determines the polymerization reaction rates. I found that a $HfCat^{Pn+}$–$MeB(C_6F_5)_3^-$ can form ISIP even after the polymer chain becomes sufficiently bulky, while $HfCat^{Pn+}$–$B(C_6F_5)_4^-$ forms mostly OSIP. Finally, I further sought to elucidate the origin of the experimentally reported molecular weight distribution (MWD) of the polymer being broader with $B(C_6F_5)_4^-$ than with $MeB(C_6F_5)_3^-$, which means that the catalytic system with $B(C_6F_5)_4^-$ has less living character than that with $MeB(C_6F_5)_3^-$. I hypothesized that the IP structure influences not only the chain propagation rate but also the chain termination reaction rate, which eventually determines the MWD of the polymer. Trajectory analyses of RM simulation showed that the chain termination reaction would be more sensitive to the dynamic effect of the CAs than the monomer insertion reaction. This is presumably because the former involves a more constrained structure than the latter and thus needs more space around the active site, which should be one of the possible origins of the MWDs being broader with $B(C_6F_5)_4^-$ than with $MeB(C_6F_5)_3^-$.

In summary, I conducted a comprehensive study on the dynamic and electronic effects of the CAs in the 1-octene polymerization reaction by (pyridylamido)Hf catalyst and numerically evaluated the polymerization and termination reaction rate constants, which provided some new insights into the reaction mechanism. Notably, it was found that the monomer coordination frequency in the diffusion process is crucial to the polymerization reaction rate. Besides, I proposed that the characteristic IP structures during the polymerization reaction should affect not only the polymerization reaction rate but also the termination reaction rate, which eventually determines the

polymer's MWDs. Therefore, in this thesis, I succeeded in demonstrating the importance of the dynamic effect of CAs in the diffusion process, which determines the catalytic activities and the physical properties of the polymers.

I expect that these findings will contribute to a further understanding of the CP reaction mechanisms with coexisting CAs. For example, the effect of other kinds of CAs, such as methyl aluminoxane (MAO), which has long been considered a "black box" in polymer chemistry, should be addressed by taking advantage of QM and MD methods in combination, and further, RM method as well. As I have demonstrated in the case of boron-based CAs in this thesis, the dynamic effect of MAO in the diffusion process should also play a crucial role in determining the catalytic activities. I believe that this thesis would be a practical example of the comprehensive mechanistic study of CP reaction focusing on the effect of CAs.

Although this thesis demonstrates the applicability of RM method to CP reaction systems, I would like to note that there is a problem to be solved: difficulty in reproducing reaction selectivity. In the RM simulation of 1-octene polymerization in Chapter 3, I found that the ratio of the four possible 1-octene insertion patterns, i.e., *cis*-1,2; *cis*-2,1; *trans*-1,2; and *trans*-2,1, of all the insertion reactions taking place in the RM simulations was not close to the ideal one, which can be estimated from the QM calculation of 1-octene insertion reaction in Chapter 2. This might be because of the limited time length of MD simulation to search for the reaction candidates. To improve this problem, I think it is necessary to improve the efficiency of the search for reaction candidates, for example, by adopting REMD instead of the conventional MD in the RM simulation procedure.

Nevertheless, one of the advantages of the atomistic simulation of CP reaction based on RM method is that the product polymer materials with observable physical properties that are comparable with experimental ones can be virtually synthesized through the simulation if appropriate reaction schemes are employed. Therefore, I expect that RM simulations would reveal the detailed mechanism of the chain shuttling polymerization (CSP) reaction to some extent, whose complex mechanistic nature makes the polymer's chemical structure quite complicated. In particular, the chain transfer reaction rate between the catalyst and chain shuttling agent such as alkyl zinc is expected to be significantly dependent on the bulkiness of the polymer chains. Therefore, RM simulation would help us establish a fundamental insight into how catalyst architectures affect the polymer's molecular structures or mechanical properties in the CSP reaction system.

I hope that my work in this thesis will provide some hints for the design principles of efficient CP reaction systems and eventually help someone in the future to pave the way for the development of new and innovative CP systems.

Acknowledgements

This thesis is the summary of my research in the Graduate School of Informatics, Nagoya University.

I would like to thank all people who supported me in completing this thesis for their invaluable assistance and discussions. First, I would like to express my deepest gratitude to Prof. Masataka Nagaoka for his kind and careful guidance and invaluable advice. I am grateful to Prof. Nobuaki Koga for his instruction on the theory of electronic states and also thank Prof. Hedong Zhang for the kind advice for this thesis. I would like to acknowledge Dr. K. Matsumoto for some helpful suggestions and his pioneering work. Further, I thank all of the collaborators in Nagaoka's laboratory for their important advice and discussions, especially Dr. Yuichi Suzuki for continuous support and daily discussions and Dr. Soumen Saha for helpful advice, and Ms. Yuko Furukawa for supporting my research activities by handling various administrative procedures on my behalf.

I would also like to express my heartfelt gratitude to Prof. Kyoko Nozaki for motivating me and showing me what a scientist should be, Prof. Koichi Yamashita for his invaluable and kind advice on how to pursue my research in computational chemistry, and Prof. Ryo Shintani for his patient and warm guidance during my bachelor's and master's courses. I would also thank Dr. Mikiya Fujii for teaching me the basics of computational chemistry.

I am grateful to my parents and fiancé so much for their support and continuous encouragement during my doctor's course.

This thesis was supported by the Japan Society for the Promotion of Science (JSPS) as a JSPS Research Fellowship for Young Scientists and also by the Core Research for Evolutional Science and Technology (CREST) "High Performance Computing for Multi-scale and Multi-physics Phenomena" and "Establishment of Molecular Technology towards the Creation of New Functions" from the Japan Science and Technology Agency (JST).

Publication List

1. Nana Misawa, Yuichi Suzuki, Soumen Saha, Nobuaki Koga, and Masataka Nagaoka, “Theoretical Elucidation of the Effect of Counteranions on the Olefin Polymerization Activity of (Pyridylamido)Hf(IV) Catalyst by QM and REMD Studies: $MeB(C_6F_5)_3^-$ versus $B(C_6F_5)_4^-$”, *Organometallics* **2021**, *40*, 48–62.
   DOI: 10.1021/acs.organomet.0c00698

   (Chapter 2)

2. Nana Misawa, Yuichi Suzuki, Soumen Saha, Nobuaki Koga, and Masataka Nagaoka, “Atomistic Simulation of the Polymerization Reaction by a (Pyridylamido)hafnium(IV) Catalyst: Counteranion Influence on the Reaction Rate and the Living Character of the Catalytic System”, *The Journal of Physical Chemistry B*, accepted.

   (Chapter 3)

3. Soumen Saha, Masayoshi Takayanagi, Hirokazu Moriya, Nana Misawa, Nobuaki Koga, and Masataka Nagaoka, “Importance of Ion-Pair on Reactivity of Zirconium Bis(phenoxy-imine) Catalyst: Quantum Mechanical Investigation”, *Chemistry A European Journal*, in preparation.